CHAPTER 14

INS/GNSS Integration

Inertial navigation (Chapter 5) has a number of advantages. It operates continuously, bar hardware faults, provides high-bandwidth output at at least 50 Hz, and exhibits low short-term noise. It provides effective attitude, angular rate, and acceleration measurements as well as position and velocity. It is also invulnerable to jamming and interference, and is nonradiating (which is important for military stealth). However, an inertial navigation solution requires initialization and its accuracy then degrades with time as the inertial instrument errors are integrated through the navigation equations. Furthermore, INS capable of providing effective sole-means navigation for more than a few minutes after initial alignment are expensive at around $100,000 (€80,000).

GNSS (Chapters 8 to 10) provides a high long-term position accuracy with errors limited to a few meters (stand-alone), while user equipment is available for less than $100 (€80). However, compared to INS, the output rate is low, typically around 10 Hz, the short-term noise of a code-based position solution is high, and standard GNSS user equipment does not measure attitude. GNSS signals are also subject to obstruction and interference, so GNSS cannot be relied upon to provide a continuous navigation solution.

The benefits and drawbacks of INS and GNSS are complementary, so by integrating them, the advantages of both technologies are combined to give a continuous, high-bandwidth, complete navigation solution with high long- and short-term accuracy. In an integrated INS/GNSS, or GNSS/INS, navigation system, GNSS measurements prevent the inertial solution drifting, while the INS smooths the GNSS solution and bridges signal outages.

INS/GNSS integration, sometimes known as hybridization, is suited to established inertial navigation applications such as ships, airliners, military aircraft, and long-range missiles. Integration with GNSS also makes inertial navigation practical with lower cost tactical-grade inertial sensors (see Chapter 4), making INS/GNSS a suitable navigation solution for light aircraft, helicopters, UAVs, short- and medium-range guided weapons, smaller boats, and potentially trains. INS/GNSS is sometimes used for road vehicles and personal navigation. However, lower cost dead-reckoning techniques, such as odometers and PDR, are often integrated with GNSS instead as discussed in Section 16.2.

Figure 14.1 shows the basic configuration of a typical INS/GNSS navigation system. The integration algorithm compares the inertial navigation solution with the outputs of GNSS user equipment and estimates corrections to the inertial position, velocity, and attitude solution, usually alongside other parameters. It is usually based on a Kalman filter, described in Chapter 3. The corrected inertial navigation solution then forms the integrated navigation solution. This architecture ensures

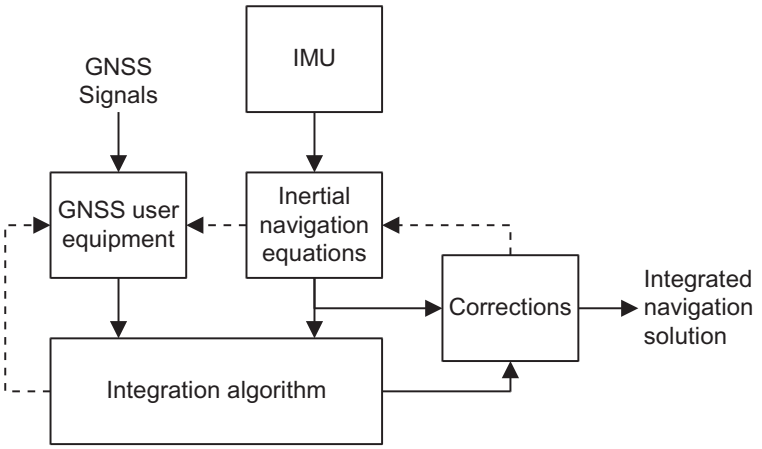

Figure 14.1 Generic INS/GNSS integration architecture.

that an integrated navigation solution is always produced, regardless of GNSS signal availability. The dotted lines in Figure 14.1 show data flows present in some systems but not others; these are discussed later.

The hardware configuration of INS/GNSS systems varies. The integration algorithm may be hosted in the INS, the GNSS user equipment, or separately. Alternatively, everything may be hosted in one unit, sometimes known as an embedded GNSS in INS (EGI) or integrated GNSS/INS (IGI). Where the inertial navigation equations and integration algorithm share the same processor, but the IMU is separate, the system is sometimes known as an integrated IMU/GNSS or GNSS/IMU. However, an IMU/GNSS is no different to an INS/GNSS.

Section 14.1 describes and compares the different INS/GNSS integration architectures. Section 14.2 discusses state selection for INS/GNSS integration Kalman filters and describes typical system models, while Section 14.3 describes measurement models. Finally, Section 14.4 discusses advanced INS/GNSS implementations, such as those using differential and carrier-phase GNSS and GNSS attitude, handling large heading errors, performing smoothing, or using advanced inertial sensor modeling. In addition, Appendix I on the CD describes several alternative formulations of INS/GNSS integration and time synchronization error estimation. MATLAB INS/GNSS integration software is also included on the CD, together with a number of demonstrations.

Figure 14.2 shows the typical stages of an INS/GNSS integration algorithm.

14.1 Integration Architectures

The architecture of an INS/GNSS integrated navigation system varies in three respects: how corrections are applied to the inertial navigation solution, what types of GNSS measurements are used, and how the GNSS user equipment is aided by the INS and integration algorithm. These are largely independent of each other. In the literature, terms such as loosely coupled, tightly coupled, ultratightly coupled, closely coupled, cascaded, deeply coupled, and deep are used to define integration architectures [1–5].

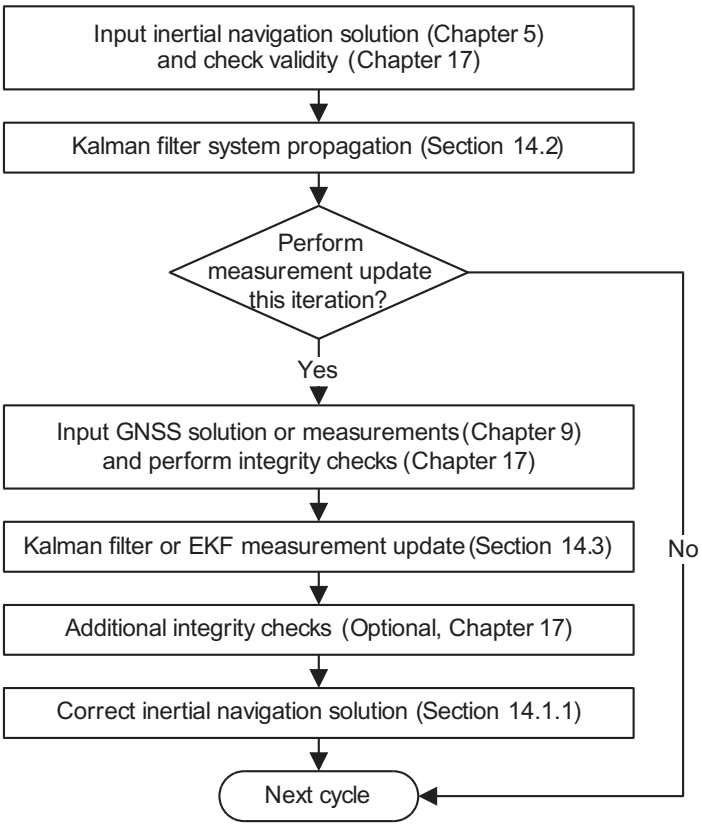

Figure 14.2 Typical stages of an INS/GNSS integration algorithm.

However, there is no commonly agreed definition of these terms. Here, the most widely used definitions are adopted.

A *loosely coupled* INS/GNSS system uses the GNSS position and velocity solution as the measurement inputs to the integration algorithm, irrespective of the type of INS correction or GNSS aiding used. It is a cascaded architecture where the GNSS user equipment incorporates a navigation filter. This is *position-domain* integration.

A *tightly coupled* INS/GNSS system uses the GNSS pseudo-range and pseudo-range-rate, delta-range, or ADR measurements as inputs to the integration algorithm, again irrespective of the type of INS correction or GNSS aiding used. This is *range-domain* integration.

A *deeply coupled* INS/GNSS system combines INS/GNSS integration and GNSS signal tracking into a single estimation algorithm. It uses the Is and Qs from the GNSS correlation channels as measurements, either directly or via discriminator functions, and generates the NCO commands used to control the reference code and carrier within the GNSS receiver (see Section 9.1.4). This is *tracking-domain* integration and is also known as deep integration.

The term *ultratightly coupled* (UTC) is used to describe both tracking-domain integration and range-domain integration with inertial aiding of the GNSS tracking loops, while the term *closely coupled* has been applied to both position-domain and range-domain integration architectures. Because of these ambiguities, both terms are avoided here.

The simplest way of combining INS and GNSS is an *uncoupled* system, whereby GNSS is simply used to reset the inertial navigation solution at intervals, often prompted by a manual command. This architecture has been applied in some aircraft where GPS was retrofitted when an INS was already installed. It is not true integration and is not discussed further.

The section begins with a description of the different methods of correcting the inertial navigation solution: open-loop correction, closed-loop correction, and total-state integration. The loosely coupled and tightly coupled architectures are then described and compared, followed by a discussion of GNSS aiding with these architectures. Finally, the deeply coupled integration architecture is described.

14.1.1 Correction of the Inertial Navigation Solution

The integrated navigation solution of an INS/GNSS integrated navigation system is the corrected inertial navigation solution. In a conventional integration architecture using an error-state Kalman filter and separate inertial navigation processing, correction may be either open-loop or closed-loop, regardless of what type of GNSS measurements are used and how the GNSS user equipment is aided.

The open-loop correction architecture, sometimes known as a feed-forward complementary filter, is shown in Figure 14.3. The estimated position, velocity, and attitude errors are used to correct the inertial navigation solution within the integration algorithm at each iteration but are not fed back to the INS. Consequently, only the integrated navigation solution contains the Kalman filter estimates and a raw INS solution is available for use in integrity monitoring (see Section 17.4.2). Either the raw INS or integrated navigation solution may be used for GNSS aiding.

The corrected inertial navigation solution, $\hat{\mathbf{C}}_b^{\gamma}$, $\hat{\mathbf{v}}_{\beta b}^{\gamma}$, and $\hat{\mathbf{r}}_{\beta b}^{\gamma}$ or $\hat{\mathbf{p}}_b$, which forms the integrated navigation solution, is obtained from the raw inertial navigation solution, $\tilde{\mathbf{C}}_b^{\gamma}$, $\tilde{\mathbf{v}}_{\beta b}^{\gamma}$, and $\tilde{\mathbf{r}}_{\beta b}^{\gamma}$ or $\tilde{\mathbf{p}}_b$, using

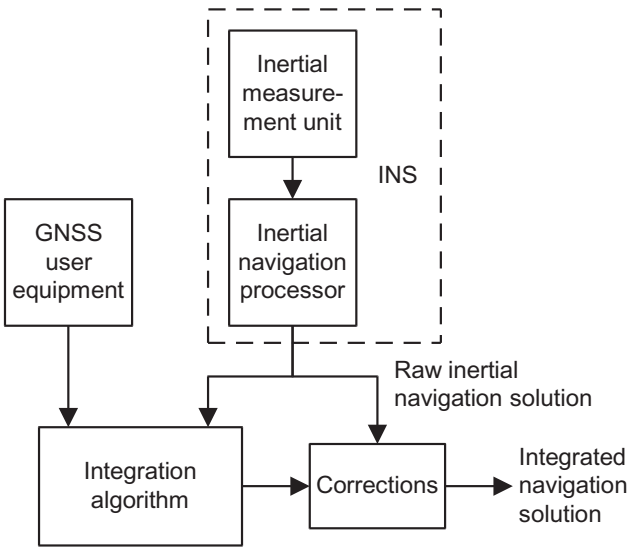

Figure 14.3 Open-loop INS correction architecture.

$$\hat{\mathbf{C}}_b^{\gamma} = \delta\hat{\mathbf{C}}_b^{\gamma\mathrm{T}}\tilde{\mathbf{C}}_b^{\gamma}, \tag{14.1}$$

$$\hat{\mathbf{v}}_{\beta b}^{\gamma} = \tilde{\mathbf{v}}_{\beta b}^{\gamma} - \delta\hat{\mathbf{v}}_{\beta b}^{\gamma} \tag{14.2}$$

and

$$\hat{\mathbf{r}}_{\beta b}^{\gamma} = \tilde{\mathbf{r}}_{\beta b}^{\gamma} - \delta\hat{\mathbf{r}}_{\beta b}^{\gamma} \tag{14.3}$$

or

$$\begin{aligned} \hat{L}_b &= \tilde{L}_b - \delta\hat{L}_b \\ \hat{\lambda}_b &= \tilde{\lambda}_b - \delta\hat{\lambda}_b \\ \hat{h}_b &= \tilde{h}_b - \delta\hat{h}_b \end{aligned}, \tag{14.4}$$

where the attitude, velocity, and position errors, $\delta\hat{\mathbf{C}}_b^{\gamma}$, $\delta\hat{\mathbf{v}}_{\beta b}^{\gamma}$, $\delta\hat{\mathbf{r}}_{\beta b}^{\gamma}$, $\delta\hat{L}_b$, $\delta\hat{\lambda}_b$, and $\delta\hat{h}_b$, are as defined by (5.107) to (5.109), with ^ denoting a Kalman filter estimate. Note that $\delta\hat{\mathbf{C}}_b^{\gamma}$ is resolved about the γ-frame axes. The reference frame, β, and resolving axes, γ, are given by

$$\{\beta,\gamma\} \in \{i,i\},\{e,e\},\{e,n\}, \tag{14.5}$$

and depend on which coordinate frames are used for the inertial navigation equations (see Chapter 5).

When the small angle approximation is applicable to the attitude errors, which is often not the case with open-loop integration, (14.1) becomes

$$\hat{\mathbf{C}}_b^{\gamma} \approx \left(\mathbf{I}_3 - \left[\delta\hat{\boldsymbol{\psi}}_{\gamma b}^{\gamma}\wedge\right]\right)\tilde{\mathbf{C}}_b^{\gamma}, \tag{14.6}$$

where $\delta\hat{\boldsymbol{\psi}}_{\gamma b}^{\gamma}$ is the Kalman filter estimate of the attitude error of the INS body frame, b, with respect to frame γ, resolved about the frame γ axes. The corresponding quaternion correction is included in Section E.6.3 of Appendix E on the CD.

In the closed-loop correction architecture, sometimes known as a feedback complementary filter, GNSS is used to aid the INS via the integration algorithm. This is shown in Figure 14.4. The estimated position, velocity, and attitude errors are fed back to the inertial navigation processor, where they are used to correct the inertial navigation solution itself. The feedback may occur either on each Kalman filter iteration or at longer intervals. The Kalman filter's position, velocity, and attitude error estimates are zeroed after each set of corrections is fed back. Consequently, there is no independent uncorrected inertial navigation solution. As discussed in Section 3.2.6, a closed-loop Kalman filter minimizes the size of the states, minimizing the linearization errors in the system model.

In closed-loop integration, there is only the corrected inertial navigation solution. New corrections are applied using

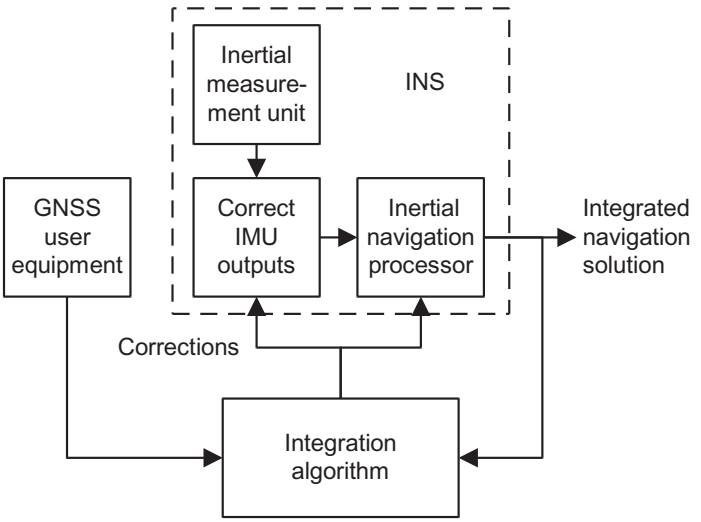

Figure 14.4 Closed-loop INS correction architecture.

$$\hat{\mathbf{C}}_b^{\gamma}(+) = \delta\hat{\mathbf{C}}_b^{\gamma\mathrm{T}}\hat{\mathbf{C}}_b^{\gamma}(-) \approx \left(\mathbf{I}_3 - \left[\delta\hat{\boldsymbol{\psi}}_{\gamma b}^{\gamma}\times\right]\right)\hat{\mathbf{C}}_b^{\gamma}(-), \tag{14.7}$$

$$\hat{\mathbf{v}}_{\beta b}^{\gamma}(+) = \hat{\mathbf{v}}_{\beta b}^{\gamma}(-) - \delta\hat{\mathbf{v}}_{\beta b}^{\gamma} \tag{14.8}$$

and

$$\hat{\mathbf{r}}_{\beta b}^{\gamma}(+) = \hat{\mathbf{r}}_{\beta b}^{\gamma}(-) - \delta\hat{\mathbf{r}}_{\beta b}^{\gamma} \tag{14.9}$$

or

$$\begin{aligned}\hat{L}_b(+) &= \hat{L}_b(-) - \delta\hat{L}_b\\ \hat{\lambda}_b(+) &= \hat{\lambda}_b(-) - \delta\hat{\lambda}_b\\ \hat{h}_b(+) &= \hat{h}_b(-) - \delta\hat{h}_b\end{aligned}, \tag{14.10}$$

where the suffixes (–) and (+) denote before and after the correction, respectively, and the small angle approximation is usually applicable to the attitude error.

In the closed-loop integration architecture, any accelerometer and gyro errors estimated by the Kalman filter are fed back to correct the IMU measurements, using (4.19) and (4.20), as they are input to the inertial navigation equations. These corrections are in addition to any that may be applied by the IMU's processor. Unlike the position, velocity, and attitude corrections, the accelerometer and gyro corrections must be applied on every iteration of the navigation equations, with feedback from the Kalman filter periodically updating the accelerometer and gyro errors. It may either feed back replacement estimates to the inertial navigation processor, or estimate residual errors and feed back perturbations to the error estimates stored by the navigation processor. In the latter case, the Kalman filter estimates are zeroed on feedback.

The choice of open- or closed-loop INS/GNSS integration is a function of both the INS quality and the integration algorithm quality. When low-grade inertial sensors are used, only the closed-loop configuration is suitable, regardless of the integration algorithm quality. This is because the raw inertial navigation solution will be of little use, while an open-loop configuration is likely to lead to large linearization errors in the Kalman filter. Conversely, when a high-quality INS is used with a low-quality integration algorithm, an open-loop configuration should be used as integrity monitoring is likely to be needed, whereas linearization errors will be small. Alternatively, a raw inertial navigation solution may be maintained in parallel to a closed-loop integrated solution. When both the INS and the integration algorithm are high quality, the open- and closed-loop configurations are both suitable.

Navigation systems where the IMU is supplied separately and the inertial navigation equations and integration algorithms share a common processor are ideally suited to closed-loop operation, as the feedback of corrections is fully under the control of the integrated navigation system designer. However, where the INS is supplied as a complete unit, closed-loop integration should be approached with caution, as it is then necessary to ensure that the corrections are sent in the form that the INS is expecting, which may not be clearly defined.

The alternative to an error-state Kalman filter in INS/GNSS integration is a total-state Kalman filter, which estimates absolute position, velocity, and attitude instead of the errors in the corresponding INS outputs. In a total-state Kalman filter, the inertial navigation equations are embedded in the system model. As these are nonlinear, the extended Kalman filter form of the system model (see Section 3.4.1) must be used. The system model is then a function of the IMU outputs [6]. Figure 14.5 shows the system architecture.

In total-state integration, the system model must be iterated at the same rate as the inertial navigation equations in an error-state implementation. However, the processor load can be limited by iterating the system propagation of the error covariance matrix, $\mathbf{P}$, at a lower rate than that of the state vector, $\mathbf{x}$. The equations processed in a total-state INS/GNSS implementation are the same as those in a closed-loop error-state implementation, so the performance will be the same. The difference lies in the software architecture.

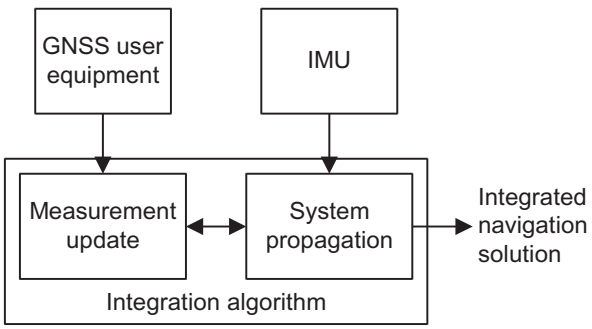

Figure 14.5 Total-state INS/GNSS integration architecture.

14.1.2 Loosely Coupled Integration

Figure 14.6 shows a loosely coupled INS/GNSS integration architecture. The GNSS position and velocity solutions (Section 9.4) are input as measurements to the integration Kalman filter, which uses them to estimate the INS errors. The integrated navigation solution is the INS navigation solution, corrected with the Kalman filter estimates of its errors. Thus, the integration is performed in the position domain, as opposed to the range domain.

Loosely coupled integration can operate with GNSS position measurements alone as the Kalman filter can infer the INS velocity error from the rate of change of position error in the same way as it infers the INS attitude and instrument errors from the changes in velocity error (see Sections 14.2.1 and 14.3.4). However, the velocity obtained by differentiating position is noisier, particularly where a code-based single-epoch GNSS position solution is used, as opposed to a carrier-smoothed-code-based or EKF-based solution. In principle, integration can also proceed using only the GNSS velocity measurements. However, this will not fully constrain the growth of the INS position error as the velocity measurement noise will be integrated up into the position state estimates. Therefore, most INS/GNSS integration algorithms use both velocity and position measurements.

The principal advantage of loosely coupled integration is simplicity. It can be used with any INS and any GNSS user equipment, making it particularly suited to retrofit applications. A further benefit is redundancy: there is usually a stand-alone

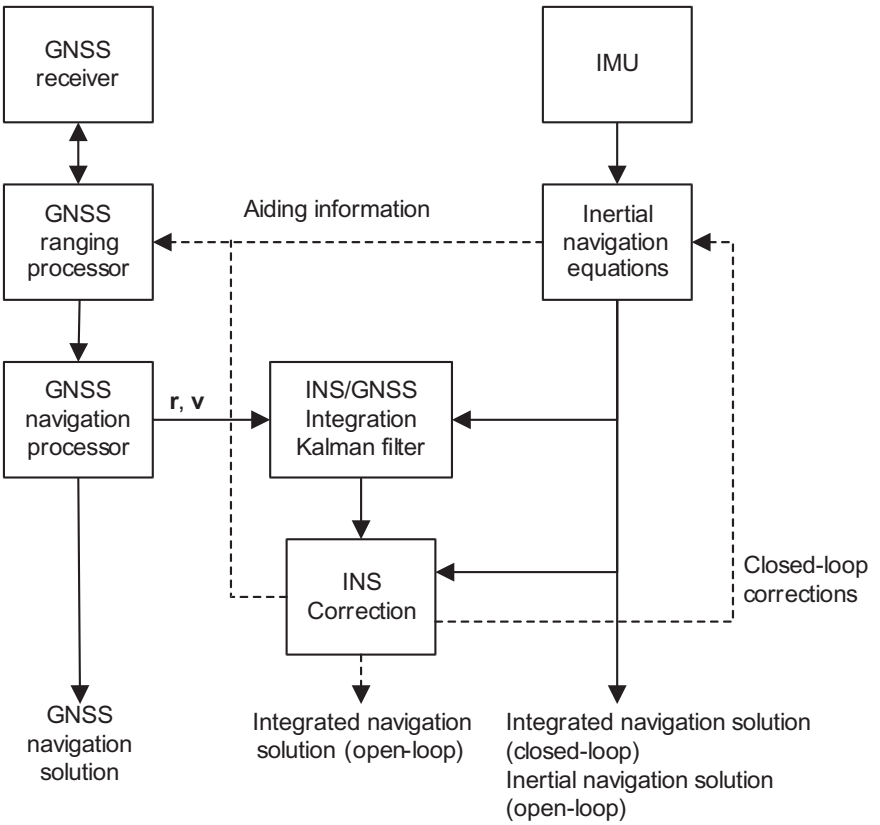

Figure 14.6 Loosely coupled INS/GNSS integration architecture.

GNSS navigation solution available in addition to the integrated solution. When open-loop INS correction is implemented, there is also an independent INS solution. This enables basic parallel solutions integrity monitoring (Section 17.4.2).

When the GNSS navigation processor is Kalman filter-based or uses carrier-smoothed pseudo-range measurements, it will output a position and velocity solution with time-correlated noise. However, an assumption of the Kalman filter used for INS/GNSS integration is that noise on the measurements it inputs is uncorrelated in time. This is a standard problem with cascaded filtered integration architectures (Section 16.1.3). As discussed in Section 3.4.3, input of measurements with time-correlated errors can disrupt Kalman filter state estimation unless the filter gain is reduced or the correlated errors are modeled as states. The correlation time of the GNSS navigation-solution errors varies and can be up to 100 seconds on the position and 20 seconds on the velocity. Selection of the integration Kalman filter gain and measurement iteration rate is therefore critical. If they are too high, the filter is liable to become unstable. However, if they are too low, the stochastic observability of the INS errors will be reduced (see Section 3.2.5). For stability, the system must be tuned so that the integration Kalman filter bandwidth is always less than that of the GNSS Kalman filter, noting that the bandwidths vary. Measurement-update intervals of 10 seconds are common in loosely coupled systems.

The cascading stability problem does not arise where the GNSS user equipment computes a single-epoch position solution without carrier smoothing of the pseudo-ranges (provided the update interval exceeds the tracking-loop time constants). However, this type of position solution is much noisier, so a low gain is still needed for the integration Kalman filter.

A further problem is that the integration filter needs to know the covariance of the GNSS navigation solution, both to ensure the correct gain is used and to estimate the accuracy of the integrated navigation solution. However, the GNSS solution covariance varies with satellite geometry and availability. With some geometries, there can be significant correlation between the position and velocity errors along different axes (see Sections 7.4.5 and 9.4.3). Furthermore, there may be significant correlation between the position error and the velocity error, depending on the GNSS navigation processor design. Few designs of GNSS user equipment output realistic error covariances; many just output DOP information, and some provide no information at all on the solution accuracy. Consequently, a conservative GNSS solution covariance must be assumed, limiting the Kalman filter gain further.

The final limitation of loosely coupled integration is that signals from at least four satellites are required to maintain a GNSS navigation solution, though an EKF-based solution can be maintained for short periods with fewer satellites. Consequently, when fewer satellites are tracked, the GNSS data cannot be used to aid the INS.

14.1.3 Tightly Coupled Integration

Figure 14.7 shows a tightly coupled INS/GNSS integration architecture. An extended Kalman filter inputs the pseudo-range and pseudo-range rate measurements from the GNSS ranging processor (Section 9.2) and uses them to estimate the INS errors, together with the GNSS receiver clock offset and bias. The integration is thus performed in the range domain. As with a loosely coupled architecture, the corrected

inertial navigation solution forms the integrated navigation solution. This is an example of centralized filtered integration (Section 16.1.4) as the GNSS navigation processor is bypassed, its function subsumed into the INS/GNSS integration filter.

The pseudo-range and pseudo-range rate measurements are complementary. Pseudo-ranges come from code tracking and can be used to determine absolute position, whereas pseudo-range rates are derived from the more precise, but less robust, carrier tracking and are used to determine changes in position. It is thus standard practice to use both. GNSS user equipment often outputs Doppler shift measurements instead of pseudo-range rates; however, the latter may be calculated from the former using (9.70). With suitable modifications to the EKF design, ADR or delta-range measurements may be used instead of pseudo-range rates.

A tightly coupled integration architecture has a number of advantages. By combining the GNSS navigation processor and INS/GNSS integration algorithm into one, the filter cascading problems of the loosely coupled architecture are eliminated. Also, the variation of the GNSS solution covariance with satellite geometry and availability is accounted for implicitly. These enable higher gains to be used, increasing the stochastic observability of the INS errors. Note, however, that the Kalman filter bandwidths must still be kept within the GNSS tracking-loop bandwidths to prevent time-correlated tracking noise from contaminating the state estimates. The final advantage of tightly coupled integration is that GNSS measurement data is

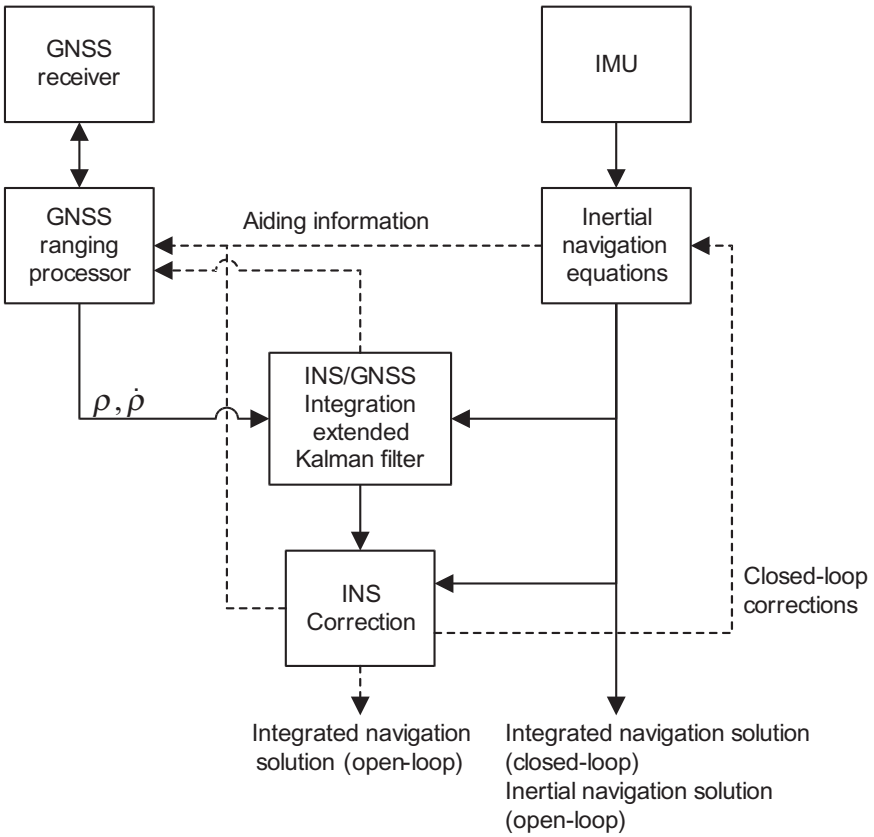

Figure 14.7 Tightly coupled INS/GNSS integration architecture.

still input and used to aid the INS when insufficient satellite signals are tracked to compute a stand-alone GNSS navigation solution.

The main limitation of tightly coupled integration is that not all designs of GNSS user equipment output the range-domain measurements required. Although there is no inherent stand-alone GNSS solution, a GNSS-only navigation solution may be maintained in parallel where required for integrity monitoring. Given the same inertial instruments and the same GNSS user equipment, a tightly coupled INS/GNSS should be both more accurate and more robust than its loosely coupled counterpart.

14.1.4 GNSS Aiding

In loosely and tightly coupled integration, the inertial navigation solution may be used to aid GNSS acquisition and tracking as discussed in Section 10.5.1 [7]. In deeply coupled integration, aiding of GNSS acquisition is the same, but tracking aiding is an inherent part of the integration architecture. When open-loop INS correction is used, either the raw or corrected inertial navigation solution may be used for GNSS acquisition and tracking aiding. The corrected solution is generally more accurate, but the raw solution is wholly independent of GNSS (after initialization), so is not subject to positive-feedback-induced errors. In tightly and deeply coupled integration, the receiver clock may also be corrected.

Acquisition aiding provides the GNSS ranging processor with the approximate position and velocity, limiting the number of cells that need to be searched to acquire the signal (see Section 9.2.1). For reacquisition, where the satellite positions and velocities are known and the receiver clock is calibrated, the number of cells to search can be very small, allowing very long dwell times in each cell. Simulations have shown that inertially aided reacquisition should be feasible at C/N_0 levels down to about 10 dB-Hz [8]. Using AGNSS (Section 10.5.2) to provide satellite information and receiver clock calibration enables a similar performance to be achieved with inertially aided initial acquisition [9].

GNSS tracking-loop bandwidths are a tradeoff between dynamics response and noise resistance (see Sections 9.2.2, 9.2.3, and 9.3.3). However, if the tracking loops are aided with the inertial navigation solution, they only have to track the receiver clock noise and the error in the INS solution, not the absolute dynamics of the user antenna. This enables narrower tracking-loop bandwidths to be used, improving noise resistance and allowing tracking to be maintained at a lower C/N_0 [10]. Integration architectures with GNSS tracking aiding are sometimes known as ultratightly coupled.

However, the downside of narrow tracking bandwidths is longer error correlation times on the GNSS measurements input to the integration algorithm. Figure 14.8 shows the code tracking time constant as a function of minimum C/N_0. This requires lower gains to be used in the Kalman filter to prevent instability (see Section 3.4.3). With an aviation-grade INS, this does not present a problem. However, with tactical-grade inertial sensors, a reduced-gain Kalman filter leads to poorer inertial calibration and larger navigation-solution errors. One solution is adaptive tightly coupled (ATC) integration [11, 12], in which the tracking-loop bandwidths are varied according to the measured c/n_0 and the measurement noise covariance in the integration algorithm adapted to the tracking bandwidths so that the Kalman

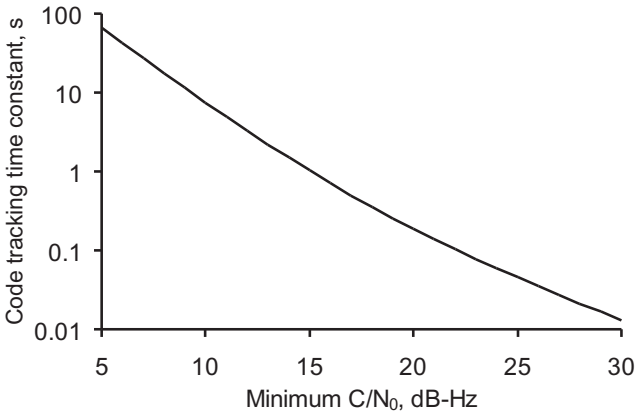

Figure 14.8 Code tracking time constant versus minimum C/N_0. [Calculated using (9.98) assuming $\sigma_x << 1/10$ chip, a DPP discriminator, and a time constant of $1/4B_{L\_CO}$.]

filter gains are matched to the tracking-error correlation times. ATC enables GNSS code to be tracked at a C/N_0 around 8 dB-Hz lower than a conventional tightly coupled system tuned for optimum INS calibration [11].

Inertial aiding of the code-tracking loop is normally implemented as a reversionary mode to carrier aiding. The pseudo-range rate for satellite s, estimated from the inertial navigation solution, is

$$\begin{aligned}\hat{\dot{\rho}}_R^s &= \hat{\mathbf{u}}_{as}^{i\,\mathrm{T}}\left(\hat{\mathbf{v}}_{is}^i(t_{st,a}^s) - \hat{\mathbf{v}}_{ia}^i(t_{sa,a}^s)\right) + \delta\hat{\dot{\rho}}_c^a - \delta\hat{\dot{\rho}}_c^s \\ &= \hat{\mathbf{u}}_{as}^{e\,\mathrm{T}}\left(\hat{\mathbf{v}}_{es}^e(t_{st,a}^s) - \hat{\mathbf{v}}_{ea}^e(t_{sa,a}^s)\right) + \delta\hat{\dot{\rho}}_{ie,a}^s + \delta\hat{\dot{\rho}}_c^a - \delta\hat{\dot{\rho}}_c^s\end{aligned}, \tag{14.11}$$

where the notation is as defined in Section 8.5.3. The receiver clock drift estimate, $\delta\hat{\dot{\rho}}_c^a$, is obtained from the integration Kalman filter in tightly coupled integration and the GNSS navigation solution in loosely coupled integration. The satellite velocity, $\hat{\mathbf{v}}_{is}^i$ or $\hat{\mathbf{v}}_{es}^e$, is obtained from the navigation data message (see Section 8.5.2). The line-of-sight vector, $\hat{\mathbf{u}}_{as}^i$ or $\hat{\mathbf{u}}_{as}^e$, is given by (8.40) or (8.41), the Sagnac correction, $\delta\hat{\dot{\rho}}_{ie,a}^s$, is given by (8.46), and the satellite clock drift correction, $\delta\hat{\dot{\rho}}_c^s$, obtained by differentiating (9.77). The GNSS antenna velocity is, from (2.165),

$$\hat{\mathbf{v}}_{\beta a}^{\gamma} = \hat{\mathbf{v}}_{\beta b}^{\gamma} + \hat{\mathbf{C}}_b^{\gamma}\left(\hat{\boldsymbol{\omega}}_{ib}^b \times \mathbf{l}_{ba}^b\right), \tag{14.12}$$

where $\mathbf{l}_{ba}^b$ is the lever arm from the IMU to the antenna, resolved about the IMU body frame and β and γ are defined by (14.5). When carrier tracking is lost, the inertial aiding information must also be used to control the carrier NCO to maintain signal coherence over the correlator accumulation interval in the receiver and GNSS ranging processor (see Section 9.1.4.4). For a 20-ms accumulation interval, the pseudo-range rate must be accurate to within about 4 m s^{-1}.

Inertial aiding can also be used to maintain synchronization of the reference code phase and carrier frequency through short signal blockages, enabling tracking to resume when the signal returns without having to undergo reacquisition first.

The key is to compensate for any loss of synchronization between loss of signal and detection of the loss of tracking lock. All-channel outages may be bridged for several tens of seconds and single-channel outages for several minutes [8].

Inertial and carrier aiding of the code tracking loop may also be implemented in parallel, in which case, a weighted average of the two pseudo-range rates should be constructed, based on the respective error standard deviations.

For inertial aiding of carrier-phase tracking, simulations have suggested that a 4 dB-Hz reduction in the minimum tolerable C/N_0 should be achievable using tactical-grade inertial sensors and a high-quality receiver oscillator [13]. However, carrier tracking aiding is challenging to implement, largely because it requires tight time synchronization for high-dynamics applications [14]. One solution is to store and retrieve the precorrelation GNSS signal samples so that inertial aiding derived from contemporaneous IMU measurements may be used; however, this requires a software receiver.

The integration algorithm's receiver-clock estimates may be fed back to correct the receiver clock itself in analogy with closed-loop INS correction. The Kalman filter states are zeroed when feedback takes place, which can occur at every iteration, at regular intervals or when the estimates exceed a predetermined threshold. Caution must be exercised in correcting for the effects of any lags in applying the clock corrections and disabling any clock feedback from the GNSS navigation processor. As no approximations are made in implementing the clock states in the Kalman filter, closed-loop receiver clock correction has no impact on performance.

The corrected inertial navigation solution can also be used to aid GNSS integrity monitoring (Chapter 17) and detection of GNSS cycle slips (see Section 10.5.1).

14.1.5 Deeply Coupled Integration

Deeply coupled, or deep, INS/GNSS integration is the INS/GNSS equivalent of combining GNSS navigation and tracking into a vector-tracking architecture, as discussed in Section 10.3.7. The terms ultratightly coupled and deeply integrated are also used to describe this architecture. Figure 14.9 shows the deeply coupled integration architecture with closed-loop INS correction. The code and carrier NCO commands are generated using the corrected inertial navigation solution, the satellite position and velocity from the navigation data message, and various GNSS error estimates. The accumulated correlator outputs from the GNSS receiver, the Is and Qs, are input via prefilters to the integration algorithm, usually Kalman filter-based, where a number of INS and GNSS errors are estimated. The corrected inertial navigation solution forms the integrated navigation solution as in the other architectures. The integration is thus performed in the tracking domain, as opposed to the range or position domain.

Compared with GNSS vector tracking, deep INS/GNSS integration has the advantage that only the errors in the INS solution need be tracked, as opposed to the absolute dynamics. This enables a lower tracking bandwidth to be used, increasing noise resistance. Deeply coupled integration can also operate with fewer than four GNSS satellites for limited periods.

Compared with tightly coupled integration, deeply coupled avoids the weighting down of the older I and Q measurement data when the pseudo-range or pseudo-range

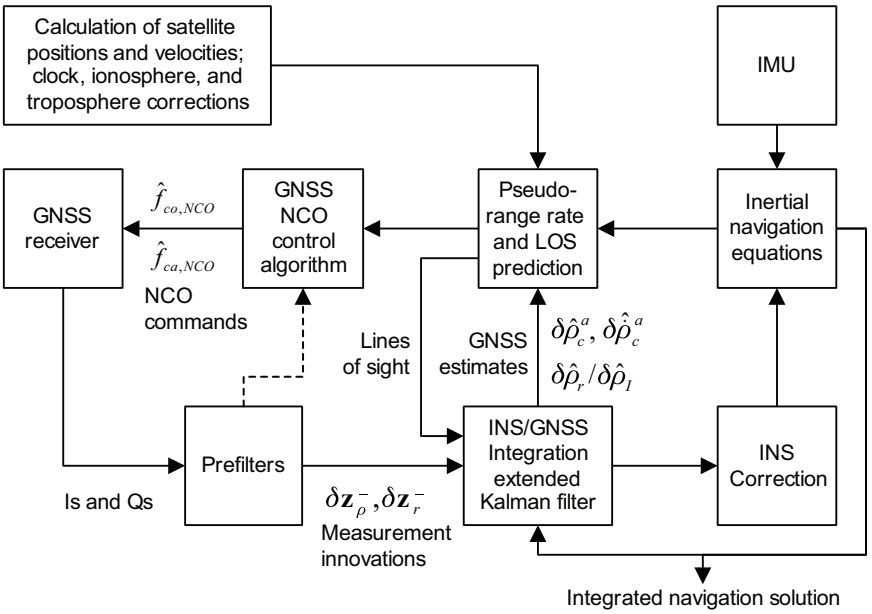

Figure 14.9 Deeply coupled INS/GNSS integration architecture (closed-loop INS correction).

rate output interval is greater than the corresponding tracking-loop time constant and avoids the need to reduce the Kalman filter gain when it is not. This enables deeply coupled integration to operate at lower C/N_0 levels. Like ATC, a deeply coupled integration algorithm can adapt to different C/N_0 levels by varying the measurement weighting. Bridging code and carrier-frequency tracking through brief signal outages is inherent in deep INS/GNSS integration. By removing the cascade between the tracking-loop filters and integration filter, deep coupling offers an optimal integration architecture [15].

For data-modulated signals, the Is and Qs must be output by the GNSS receiver at at least the navigation message symbol rate (50 Hz for the legacy GPS and GLONASS signals). A faster data rate reduces communication lags, but requires the integration algorithm to know where the navigation data-bit transitions are so that it can perform correct coherent summation of the Is and Qs. The NCO commands are usually input by the GNSS receiver at the same rate as the Is and Qs are output. The need to implement a new and much faster interface between the GNSS user equipment and integration algorithm is the main drawback of deeply coupled integration and makes it difficult to retrofit [16].

The prefilters input the Is and Qs from the receiver at its output rate, process them and then output pseudo-range and pseudo-range-rate or delta-range measurement innovations to the integration filter, usually an EKF, at a lower rate, typically 1–10 Hz. By reducing both the number of measurements input to the EKF and their rate, the processor load is reduced to a practical level. There is one prefilter per signal or satellite tracked. In some architectures, information from the prefilters is also used to correct the NCO commands; this is shown by the dotted line in Figure 14.9.

This combination of prefilters and integration filter is an example of a federated integration architecture as described in Section 16.1.5 [17]. As a key driver of deeply

coupled integration is to maximize the filtering gain by removing cascades between successive filters, the zero-reset version of the federated architecture is employed. This avoids cascading errors by removing information from the prefilters when it is passed to the integration filter.

There are two classes of deeply coupled integration; coherent and noncoherent [18]. These are distinguished by the prefilter design. In noncoherent integration, the prefilters process the Is and Qs using separate code and carrier discriminator functions. In coherent integration, the prefilters estimate the code-phase, carrier-phase, and carrier-frequency tracking errors between integration EKF updates, inputting the Is and Qs directly. If the prefilters are bypassed and the Is and Qs input directly to the integration filter, the integration is coherent. However, this is not currently practical due to the much higher processing load.

Coherent integration is more accurate as it avoids discriminator nonlinearities and reduces code-tracking noise to that obtained with a coherent discriminator (see Section 9.3.3). However, it can only operate where there is sufficient signal to noise to track carrier phase, so noncoherent deeply coupled integration is more robust. The benefits of both approaches may be realized by switching the prefilters between coherent and noncoherent operation according to the signal quality and dynamics. This is analogous to switching between carrier-phase and carrier-frequency tracking in a conventional GNSS receiver as discussed in Section 9.2.3.

Tests have shown that noncoherent deep INS/GPS integration can stably track code at C/N_0 levels of 8–12 dB-Hz using a tactical-grade IMU [19–22]. This represents a margin of at least 8–12 dB-Hz over conventional tightly coupled INS/GPS with wide tracking bandwidths. Carrier-phase tracking down to 15 dB-Hz C/N_0 has been demonstrated with coherent deeply coupled integration and navigation data-bit estimation [23, 24].

The tracking sensitivity is affected by a number of factors. The quality of the IMU is important as sensor noise limits the extent to which the receiver tracking bandwidth may be narrowed. In most studies reported in the literature, a tactical-grade IMU was used. Using an aviation-grade IMU enables tracking to be maintained at a C/N_0 6 dB-Hz lower than when a tactical-grade IMU is used [21]. However, with calibrated automotive- or consumer-grade inertial sensors, the tracking sensitivity is 4 dB-Hz poorer than with tactical-grade sensors [21, 22]. This may be no more sensitive than stand-alone GNSS using vector tracking [25]. The receiver oscillator must also be of an adequate standard, particularly for coherent implementations [26].

A further limiting factor is the C/N_0 measurement algorithm (Section 9.2.6). The C/N_0 measurements (or equivalent parameters such as signal amplitude) are used to determine the correct weighting of the GNSS measurements in the integration filter (see Section 14.3.3). However, at the lowest signal-to-noise levels, C/N_0 measurements are very noisy and the design of the C/N_0 measurement algorithm has been shown to have a significant impact on tracking robustness [18].

14.2 System Model and State Selection

The system model of a Kalman filter is described in Section 3.2.3. For INS/GNSS integration, it depends on which quantities are estimated as Kalman filter states

which, in turn, depends on the application, inertial sensors, integration architecture, and choice of coordinate frame. State selection is thus described first. A typical INS state-propagation model is then derived in an ECI frame, followed by descriptions of the ECEF-frame and local-navigation-frame equivalents. Modeling additional IMU errors, INS system noise modeling, and GNSS state propagation and system noise are then described. Discussion of state and error covariance initialization completes the section. In addition, wander-azimuth-frame and local-tangent-plane-frame state propagation models are described in Sections I.3 and I.4, respectively, of Appendix I on the CD.

There is no interaction between the INS and GNSS states in the system model; they only interact through the measurement model. Therefore, the system, transition, and system noise covariance matrices may be partitioned:

$$\mathbf{F} = \begin{pmatrix} \mathbf{F}_{INS} & \mathbf{0} \\ \mathbf{0} & \mathbf{F}_{GNSS} \end{pmatrix}, \quad \boldsymbol{\Phi} = \begin{pmatrix} \boldsymbol{\Phi}_{INS} & \mathbf{0} \\ \mathbf{0} & \boldsymbol{\Phi}_{GNSS} \end{pmatrix}, \quad \mathbf{Q} = \begin{pmatrix} \mathbf{Q}_{INS} & \mathbf{0} \\ \mathbf{0} & \mathbf{Q}_{GNSS} \end{pmatrix}, \tag{14.13}$$

where

$$\mathbf{x} = \begin{pmatrix} \mathbf{x}_{INS} \\ \mathbf{x}_{GNSS} \end{pmatrix}. \tag{14.14}$$

An error-state implementation is assumed here; for total-state INS/GNSS integration, the propagation of the position, velocity, and attitude errors should be replaced by the inertial navigation equations described in Chapter 5.

14.2.1 State Selection and Observability

All error-state INS/GNSS integration algorithms estimate the position and velocity errors. These may be expressed in an ECI frame as $\delta\mathbf{r}^i_{ib}$ and $\delta\mathbf{v}^i_{ib}$, in an ECEF frame as $\delta\mathbf{r}^e_{eb}$ and $\delta\mathbf{v}^e_{eb}$, or in a local navigation frame as δL_b, $\delta\lambda_b$, δh_b, and $\delta\mathbf{v}^n_{eb}$. An ECI-frame implementation leads to the sparsest system matrix, which can thus be multiplied most efficiently. However, it is also good practice to match the coordinate frame used for the integration algorithm to that used for the inertial navigation equations (Chapter 5).

For all but the highest grades of INS, there is significant benefit in estimating the attitude error, which here is expressed as a small angle, resolved about the coordinate frame used for navigation, $\delta\boldsymbol{\psi}^{\gamma}_{\gamma b}$. It may also be resolved about the INS body frame axes, giving $\delta\boldsymbol{\psi}^{b}_{\gamma b}$ (see Section I.5 of Appendix I on the CD), or expressed as a quaternion [27] or rotation vector [2]. The small angle approximation is only suited to attitude errors in which closed-loop INS correction is applied or the INS is of a high grade. For example, applying this approximation to a 2° attitude error perturbs the state estimate by about 5%. The handling of large attitude errors is discussed in Section 14.4.4.

The choice of inertial instrument errors to estimate depends on their effect on the position, velocity, and attitude solution. If an IMU error has a significant impact

on the navigation accuracy, it will be observable. Conversely, if its impact is much less than that of the random noise (Section 4.4.3), which cannot be calibrated, it will not be observable. Kalman filter state observability is discussed in general terms in Section 3.2.5. The deterministic observability of the inertial sensor errors, and also the attitude errors, depends on the user dynamics. The stochastic observability depends primarily on the IMU design; larger systematic errors are easier to observe, while high levels of random noise make systematic errors more difficult to observe. The Kalman filter measurement noise also impacts the stochastic observability of the states. Observability of INS error states is discussed more formally in [28]. Note that the observability is independent of the axes about which the states are resolved.

Except where they are very small, the accelerometer biases, $\mathbf{b}_a$, should always be estimated where the attitude errors are estimated. Conversely, the attitude errors should always be estimated where the accelerometer biases are estimated. Otherwise, the attitude error estimates are contaminated by the effects of the acceleration errors or vice versa. This is because, in INS/GNSS integration, the attitude and acceleration errors are observed through the growth in the velocity and position error they produce (see Section 14.3.4). As described in Section 5.7, both types of error lead to an initial linear growth in velocity error and quadratic growth in position error.

As (5.114) shows, the heading error only produces a velocity error when there is acceleration in the horizontal plane. Therefore, the navigation system's host must undergo significant maneuvering for the INS heading error to be observed and calibrated using GNSS measurements. When the navigation system is level and not accelerating, the vertical accelerometer bias is the only Kalman filter state that causes growth of the vertical velocity error. This makes it the most observable of the accelerometer biases and, as a consequence, an INS/GNSS navigation solution exhibits lower vertical drift than horizontal drift during GNSS outages of a few minutes.

The roll and pitch attitude errors and horizontal accelerometer biases are observed as linear combinations under conditions of constant acceleration and attitude. To fully separate the estimates of these states, the host-vehicle must turn, while a forward acceleration will separate the pitch error and forward accelerometer bias. The Kalman filter keeps a record of the correlations between its state estimates in the off-diagonal elements of its error covariance matrix, $\mathbf{P}$. This is used to separate the attitude and acceleration error estimates when their impact on the velocity error changes. Note that initialization of the roll and pitch solution using accelerometer leveling introduces correlations between the roll and pitch errors and all three accelerometer biases as described in Section 14.2.8.

The gyro biases, $\mathbf{b}_g$, are also estimated in most INS/GNSS integration algorithms. These are the only significant error sources that produce a quadratic growth in the velocity error with time. Consequently, the x- and y-axis gyro biases, which couple continuously into the velocity error (see Section 5.7.1), have better deterministic observability than the roll and pitch attitude errors and horizontal accelerometer biases as no maneuvers are required to separate them from other states. However, the stochastic observability is poorer as measurements must be made over time in order to distinguish the quadratic, linear, and random contributions to the velocity error growth. As with the attitude error, the z-axis (heading) gyro bias is more difficult to observe as a series of maneuvers that provide deterministic observability of the heading error must be performed.

Whether there is any benefit in estimating the accelerometer and gyro scale factor and cross-coupling errors (Section 4.4.2) or the gyro g-dependent biases (Section 4.4.4) depends on the accelerations and angular rates exhibited by the host vehicle as well as the magnitude of the errors. Maneuver-dependent INS error growth is discussed in Section 5.7.3. For most air, land, sea, and space applications, these errors are difficult to observe unless they are comparatively large. Exceptions are highly dynamic applications, such as motor sports, combat aircraft, and some guided weapons. Gyro scale factor and cross-coupling errors can also be significant for aircraft performing circling movements and roll-stabilized guided weapons.

A common mistake is to estimate scale factor errors, but not cross-coupling errors, as in most IMUs, they are of a similar magnitude. Estimating all of the scale factor and cross-coupling errors requires 15 states, while estimating all components of the gyro g-dependent biases requires a further nine states. Often, individual dynamics-dependent IMU errors are observable, but not the full set. Therefore, to make best use of the available processing capacity, simulations (or analytical sensitivity analysis) should be conducted in order to determine which errors should be estimated (see Section 3.3.5 and Appendix J on the CD).

Sometimes, where the observability of scale factor and cross-coupling errors is borderline, their inclusion in the Kalman filter state vector can improve the estimation of the accelerometer and gyro biases through the use of a more representative model of the IMU in the Kalman filter. Separating the biases into separate static and dynamic states (see Section 4.4.1) can have a similar effect [11]. Alternatively, these errors may be modeled as correlated system noise using a Schmidt-Kalman filter (Section D.2 of Appendix D on the CD).

The inertial navigation solution will also be subject to gravity-modeling errors. These produce acceleration biases aligned with the reference frame, as opposed to the vehicle body frame. The biases are of order 10^{-3} m s^{-2} per axis where a simple gravity model is used [1, 29] and of order 2×10^{-4} m s^{-2} per axis with a precision model [30]. However, estimation of the gravity-modeling errors as separate states is typically restricted to high-precision applications. Otherwise, their effects are absorbed by the z-axis accelerometer bias state and the components of the attitude error states resolved about the horizontal axes.

The choice of GNSS states to estimate depends on the integration architecture. In loosely coupled integration, no GNSS states are normally estimated. In tightly and deeply coupled integration, the receiver clock offset, $\delta\rho_c^a$, and drift, $\delta\dot{\rho}_c^a$, must normally be estimated as described in Section 9.4.2 for a stand-alone GNSS navigation filter. In an integrated INS/GNSS, the specific force on the receiver's reference oscillator is known, so the clock g-dependent errors may be estimated by the Kalman filter where they have an impact on system performance. Estimation of interconstellation timing biases may also be required in multiconstellation implementations.

In tightly coupled integration, GNSS measurements may be differenced across satellites. This cancels out the receiver clock errors enabling the clock states to be omitted, reducing the processor load. However, at least two satellites must then be tracked for GNSS measurements to be processable and any INS calibration to thus take place. Furthermore, the benefit of clock coasting to help limit position error growth during partial GNSS outages is lost.

In dual-frequency GNSS user equipment, the ionosphere propagation error is normally corrected by combining pseudo-range measurements made on different frequencies, as described in Section 9.3.2. Another way of performing the smoothing is to estimate the ionosphere propagation delays as Kalman filter states, inputting the pseudo-range measurements on different frequencies separately. In a tightly coupled architecture, this significantly increases the processor load without bringing performance benefits. In deeply coupled integration, it is the only way of performing dual-frequency ionosphere calibration. However, the ionosphere error states can be incorporated in the prefilters instead of the main integration filter. Either the total ionosphere propagation delays or the errors in ionosphere model predictions may be estimated.

As discussed in Section 9.4.2.1, the Kalman filter may also estimate the correlated range errors due to the ephemeris and the residual satellite clock, troposphere, and ionosphere errors. These range biases are partially observable where signals from more than four GNSS satellites are tracked. Their inclusion as states or correlated system noise leads to a more representative error covariance matrix, **P**. In deeply coupled integration, range bias estimation can be used to keep the reference codes aligned with their respective signal correlation peaks where the range biases are a significant proportion of the code chip length. When range biases are not estimated, the position and clock offset uncertainties should be modified as described in Section 9.4.2.5.

If a short correlation time is modeled, range bias states could also be used to absorb NLOS reception errors, and possibly multipath errors, lessening their impact on the navigation solution.

Finally, if it is not practical to accurately measure the lever arm from the IMU to the GNSS antenna, $\mathbf{l}_{ba}^{b}$, this may also be estimated as Kalman filter states.

14.2.2 INS State Propagation in an Inertial Frame

A state propagation model is developed here for a Kalman filter estimating attitude, velocity, and position errors referenced to and resolved in an ECI frame, together with the accelerometer and gyro biases. The INS partition of the state vector comprises the following 15 states

$$\mathbf{x}_{INS}^{i} = \begin{pmatrix} \delta\boldsymbol{\psi}_{ib}^{i} \\ \delta\mathbf{v}_{ib}^{i} \\ \delta\mathbf{r}_{ib}^{i} \\ \mathbf{b}_{a} \\ \mathbf{b}_{g} \end{pmatrix}, \tag{14.15}$$

where the superscript i is used to denote an ECI-frame implementation of the integration Kalman filter, consistent with the notation used in Section 9.4.2.

To obtain the INS system model, the time derivative of each Kalman filter state must be calculated. The attitude error propagation is derived first, followed by the

velocity and position error propagation. The complete continuous-time system model is then presented, followed by a discussion of its discrete-time implementation in the form of a transition matrix.

In a real navigation system, the true values of the attitude, velocity, and other kinematic parameters are unknown. The best estimates available are the corrected INS-indicated parameters. Thus, for a generic parameter, y, the approximation $y \approx \mathrm{E}(y) = \hat{y}$ must be made in deriving the system model. This also applies to the measurement model. Note that where closed-loop correction of INS errors is implemented, the raw and corrected INS outputs are the same, so for a generic parameter, y, $\tilde{y} = \hat{y}$.

14.2.2.1 Attitude Error Propagation

From (5.111), the time derivative of the small-angle attitude error, $\delta\boldsymbol{\psi}^i_{ib}$, may be obtained by differentiating its coordinate transformation matrix counterpart:

$$\left[\dot{\delta\boldsymbol{\psi}}^i_{ib} \times\right] \approx \dot{\delta\mathbf{C}}^i_b. \tag{14.16}$$

From (5.109),

$$\dot{\delta\mathbf{C}}^i_b = \dot{\tilde{\mathbf{C}}}^i_b\mathbf{C}^b_i + \tilde{\mathbf{C}}^i_b\dot{\mathbf{C}}^b_i, \tag{14.17}$$

while from (2.56)

$$\dot{\mathbf{C}}^i_b = \mathbf{C}^i_b\boldsymbol{\Omega}^b_{ib}, \tag{14.18}$$

noting that $\boldsymbol{\Omega}^b_{ib}$ is the skew-symmetric matrix of the angular rate, $\boldsymbol{\omega}^b_{ib}$. Substituting (14.18) and (14.17) into (14.16) gives

$$\left[\dot{\delta\boldsymbol{\psi}}^i_{ib} \times\right] \approx \dot{\tilde{\mathbf{C}}}^i_b\tilde{\boldsymbol{\Omega}}^b_{ib}\mathbf{C}^b_i + \tilde{\mathbf{C}}^i_b\mathbf{C}^b_i\boldsymbol{\Omega}^i_{bi}. \tag{14.19}$$

Applying (2.51) and rearranging,

$$\tilde{\mathbf{C}}^b_i\left[\dot{\delta\boldsymbol{\psi}}^i_{ib} \times\right]\mathbf{C}^i_b \approx \tilde{\boldsymbol{\Omega}}^b_{ib} - \boldsymbol{\Omega}^b_{ib}. \tag{14.20}$$

A fundamental assumption of the Kalman filter is that the system model is a linear function of the states; otherwise a nonlinear estimation algorithm must be used. For a linear system model to be valid in practice, the product of any two Kalman filter states must be negligible. Thus, applying the approximation $\delta\boldsymbol{\psi}^i_{ib}\dot{\delta\boldsymbol{\psi}}^i_{ib} \approx 0$,

$$\begin{aligned}\tilde{\mathbf{C}}^b_i\left[\dot{\delta\boldsymbol{\psi}}^i_{ib} \times\right]\mathbf{C}^i_b &\approx \hat{\mathbf{C}}^b_i\left[\dot{\delta\boldsymbol{\psi}}^i_{ib} \times\right]\hat{\mathbf{C}}^i_b \\ &= \left[\left(\hat{\mathbf{C}}^b_i\dot{\delta\boldsymbol{\psi}}^i_{ib}\right) \times\right]\end{aligned}. \tag{14.21}$$

Substituting this into (14.20), taking the components of the skew-symmetric matrices and rearranging gives

$$\begin{aligned}\delta\boldsymbol{\psi}^i_{ib} &\approx \hat{\mathbf{C}}^i_b\left(\tilde{\boldsymbol{\omega}}^b_{ib} - \boldsymbol{\omega}^b_{ib}\right)\\ &= \hat{\mathbf{C}}^i_b\delta\boldsymbol{\omega}^b_{ib}\end{aligned}. \tag{14.22}$$

The error in the gyro triad's angular-rate output, $\delta\boldsymbol{\omega}^b_{ib}$, is given by (4.17) and (4.18), When the biases are the only gyro errors modeled as Kalman filter states, the expectation of (14.22) is

$$\mathrm{E}\left(\delta\boldsymbol{\psi}^i_{ib}\right) \approx \hat{\mathbf{C}}^i_b\mathbf{b}_g. \tag{14.23}$$

14.2.2.2 Velocity Error Propagation

From (5.18) and (5.19), the time derivative of the ECI-frame velocity is

$$\dot{\mathbf{v}}^i_{ib} = \mathbf{f}^i_{ib} + \boldsymbol{\gamma}^i_{ib}. \tag{14.24}$$

Thus, the time derivative of the velocity error is

$$\delta\dot{\mathbf{v}}^i_{ib} = \tilde{\mathbf{f}}^i_{ib} - \mathbf{f}^i_{ib} + \tilde{\boldsymbol{\gamma}}^i_{ib} - \boldsymbol{\gamma}^i_{ib}. \tag{14.25}$$

The accelerometers measure specific force in body axes, so the error in $\tilde{\mathbf{f}}^i_{ib}$ is due to a mixture of accelerometer and attitude errors:

$$\tilde{\mathbf{f}}^i_{ib} - \mathbf{f}^i_{ib} = \tilde{\mathbf{C}}^i_b\tilde{\mathbf{f}}^b_{ib} - \mathbf{C}^i_b\mathbf{f}^b_{ib}. \tag{14.26}$$

Assuming the products of Kalman filter states may be neglected,

$$\begin{aligned}\tilde{\mathbf{f}}^i_{ib} - \mathbf{f}^i_{ib} &= \tfrac{1}{2}\left(\tilde{\mathbf{C}}^i_b + \mathbf{C}^i_b\right)\left(\tilde{\mathbf{f}}^b_{ib} - \mathbf{f}^b_{ib}\right) + \tfrac{1}{2}\left(\tilde{\mathbf{C}}^i_b - \mathbf{C}^i_b\right)\left(\tilde{\mathbf{f}}^b_{ib} + \mathbf{f}^b_{ib}\right)\\ &\approx \hat{\mathbf{C}}^i_b\left(\tilde{\mathbf{f}}^b_{ib} - \mathbf{f}^b_{ib}\right) + \left(\tilde{\mathbf{C}}^i_b - \mathbf{C}^i_b\right)\hat{\mathbf{f}}^b_{ib}\end{aligned}. \tag{14.27}$$

The error in the accelerometer triad's specific-force output, $\delta\mathbf{f}^b_{ib}$, is given by (4.16) and (4.18). When the biases are the only accelerometer errors modeled as Kalman filter states, the expectations of the accelerometer errors are

$$\mathrm{E}\left(\tilde{\mathbf{f}}^b_{ib} - \mathbf{f}^b_{ib}\right) = \mathrm{E}\left(\delta\mathbf{f}^b_{ib}\right) \approx \mathbf{b}_a. \tag{14.28}$$

Applying the small angle approximation to the attitude error, (5.109) and (5.111) give

$$\begin{aligned}\tilde{\mathbf{C}}_b^i - \mathbf{C}_b^i &= \left(\delta\mathbf{C}_b^i - \mathbf{I}_3\right)\mathbf{C}_b^i \\ &\approx \left[\delta\boldsymbol{\psi}_{ib}^i \wedge\right]\mathbf{C}_b^i\end{aligned}. \tag{14.29}$$

Turning to the gravitational term in (14.25), from Section 2.4.7, this scales with height roughly as [(2.138) repeated]:

$$\boldsymbol{\gamma}_{ib}^i \approx \frac{\left(r_{eS}^e(L_b)\right)^2}{\left(r_{eS}^e(L_b) + h_b\right)^2}\boldsymbol{\gamma}_0^i(L_b),$$

where the geocentric radius at the Earth's surface, r_{eS}^e, is given by (2.137).

As the variation of gravitation with latitude is small, the effect of the latitude error on the assumed gravitational acceleration may be neglected. Making the additional assumption that $h_b << r_{eS}^e$ gives

$$\tilde{\boldsymbol{\gamma}}_{ib}^i - \boldsymbol{\gamma}_{ib}^i \approx -2\frac{\left(\tilde{h}_b - h_b\right)}{r_{eS}^e(\hat{L}_b)}\hat{\boldsymbol{\gamma}}_{ib}^i, \tag{14.30}$$

where $\hat{\boldsymbol{\gamma}}_{ib}^i$ is the gravitational acceleration at the estimated position, $\hat{\mathbf{r}}_{ib}^i$. Assuming that the height error corresponds approximately to the position error component resolved along the Cartesian position vector from the center of the Earth gives

$$\tilde{\boldsymbol{\gamma}}_{ib}^i - \boldsymbol{\gamma}_{ib}^i \approx -\frac{2\hat{\boldsymbol{\gamma}}_{ib}^i}{r_{eS}^e(\hat{L}_b)}\frac{\hat{\mathbf{r}}_{ib}^{i\,\mathrm{T}}}{\left|\hat{\mathbf{r}}_{ib}^i\right|}\delta\mathbf{r}_{ib}^i. \tag{14.31}$$

Substituting (14.28) and (14.29) into (14.27), and (14.27) and (14.31) into (14.25) gives the expectation of the time derivative of the velocity error in terms of the Kalman filter states:

$$\mathrm{E}\left(\delta\dot{\mathbf{v}}_{ib}^i\right) \approx -\left(\hat{\mathbf{C}}_b^i\hat{\mathbf{f}}_{ib}^b\right) \wedge \delta\boldsymbol{\psi}_{ib}^i - \frac{2\hat{\boldsymbol{\gamma}}_{ib}^i}{r_{eS}^e(\hat{L}_b)}\frac{\hat{\mathbf{r}}_{ib}^{i\,\mathrm{T}}}{\left|\hat{\mathbf{r}}_{ib}^i\right|}\delta\mathbf{r}_{ib}^i + \hat{\mathbf{C}}_b^i\mathbf{b}_a. \tag{14.32}$$

14.2.2.3 Position Error Propagation

As the resolving axes and reference frame are the same, the time derivative of ECI-frame position is simply velocity, as shown by (5.22):

$$\dot{\mathbf{r}}_{ib}^i = \mathbf{v}_{ib}^i.$$

The time derivative of the position error is thus simply the velocity error:

$$\delta\dot{\mathbf{r}}_{ib}^i = \delta\mathbf{v}_{ib}^i. \tag{14.33}$$

14.2.2.4 System and Transition Matrices

The accelerometer and gyro biases, $\mathbf{b}_a$ and $\mathbf{b}_g$, are assumed not to have a known time variation. Thus, their expected time derivatives are zero:

$$\mathrm{E}\left(\dot{\mathbf{b}}_a\right) = 0, \qquad \mathrm{E}\left(\dot{\mathbf{b}}_g\right) = 0. \tag{14.34}$$

Substituting (14.23) and (14.32) to (14.34) into (3.26), the system matrix, expressed in terms of 3×3 submatrices corresponding to the components of the state vector in (14.15), is

$$\mathbf{F}_{INS}^{i} = \begin{pmatrix} \mathbf{0}_3 & \mathbf{0}_3 & \mathbf{0}_3 & \mathbf{0}_3 & \hat{\mathbf{C}}_b^i \\ \mathbf{F}_{21}^i & \mathbf{0}_3 & \mathbf{F}_{23}^i & \hat{\mathbf{C}}_b^i & \mathbf{0}_3 \\ \mathbf{0}_3 & \mathbf{I}_3 & \mathbf{0}_3 & \mathbf{0}_3 & \mathbf{0}_3 \\ \mathbf{0}_3 & \mathbf{0}_3 & \mathbf{0}_3 & \mathbf{0}_3 & \mathbf{0}_3 \\ \mathbf{0}_3 & \mathbf{0}_3 & \mathbf{0}_3 & \mathbf{0}_3 & \mathbf{0}_3 \end{pmatrix}, \tag{14.35}$$

where

$$\mathbf{F}_{21}^i = \left[-\left(\hat{\mathbf{C}}_b^i \hat{\mathbf{f}}_{ib}^b \right) \wedge \right], \qquad \mathbf{F}_{23}^i = -\frac{2\hat{\boldsymbol{\gamma}}_{ib}^i}{r_{eS}^e(\hat{L}_b)} \frac{\hat{\mathbf{r}}_{ib}^{i\mathrm{T}}}{\left| \hat{\mathbf{r}}_{ib}^i \right|}. \tag{14.36}$$

As shown in Section 3.2.3, the transition matrix, $\boldsymbol{\Phi}$, is a power-series expansion of $\mathbf{F}\tau_s$. In practice, the Kalman filter designer must determine which terms to include and which to neglect. This does not have to be a uniform truncation of the power-series (e.g., some second-order terms may be included and others neglected). Assuming that all zeroth- and first-order terms are retained, the maximum magnitude of each higher-order term should be estimated and a determination made as to whether its inclusion will have a significant effect on the integration algorithm performance. The shorter the state propagation interval, τ_s, the smaller the higher-order terms will be. To ensure that the power-series expansion converges, τ_s should be 1 second or less. When there is a long interval between measurement updates, such as in many loosely coupled implementations, it may be necessary to run the system propagation at shorter intervals or use a nonlinear filter, such as a UKF.

When the power series is limited to the first order in $\mathbf{F}\tau_s$, the transition matrix is

$$\boldsymbol{\Phi}_{INS}^i \approx \begin{bmatrix} \mathbf{I}_3 & \mathbf{0}_3 & \mathbf{0}_3 & \mathbf{0}_3 & \hat{\mathbf{C}}_b^i \tau_s \\ \mathbf{F}_{21}^i \tau_s & \mathbf{I}_3 & \mathbf{F}_{23}^i \tau_s & \hat{\mathbf{C}}_b^i \tau_s & \mathbf{0}_3 \\ \mathbf{0}_3 & \mathbf{I}_3 \tau_s & \mathbf{I}_3 & \mathbf{0}_3 & \mathbf{0}_3 \\ \mathbf{0}_3 & \mathbf{0}_3 & \mathbf{0}_3 & \mathbf{I}_3 & \mathbf{0}_3 \\ \mathbf{0}_3 & \mathbf{0}_3 & \mathbf{0}_3 & \mathbf{0}_3 & \mathbf{I}_3 \end{bmatrix}. \tag{14.37}$$

When terms of up to the third order in $\mathbf{F}\tau_s$ are included and $\left|F^i_{23,ij}\right|\tau_s^2 << 1$ for all i and j is assumed, it becomes

$$\boldsymbol{\Phi}^i_{INS} \approx \begin{bmatrix} \mathbf{I}_3 & \mathbf{0}_3 & \mathbf{0}_3 & \mathbf{0}_3 & \hat{\mathbf{C}}^i_b\tau_s \\ \mathbf{F}^i_{21}\tau_s & \mathbf{I}_3 & \mathbf{F}^i_{23}\tau_s & \hat{\mathbf{C}}^i_b\tau_s & \frac{1}{2}\mathbf{F}^i_{21}\hat{\mathbf{C}}^i_b\tau_s^2 \\ \frac{1}{2}\mathbf{F}^i_{21}\tau_s^2 & \mathbf{I}_3\tau_s & \mathbf{I}_3 & \frac{1}{2}\hat{\mathbf{C}}^i_b\tau_s^2 & \frac{1}{6}\mathbf{F}^i_{21}\hat{\mathbf{C}}^i_b\tau_s^3 \\ \mathbf{0}_3 & \mathbf{0}_3 & \mathbf{0}_3 & \mathbf{I}_3 & \mathbf{0}_3 \\ \mathbf{0}_3 & \mathbf{0}_3 & \mathbf{0}_3 & \mathbf{0}_3 & \mathbf{I}_3 \end{bmatrix}. \tag{14.38}$$

14.2.3 INS State Propagation in an Earth Frame

When the Kalman-filter-estimated attitude, velocity, and position errors are referenced to and resolved in an ECEF frame, the state vector becomes

$$\mathbf{x}^e_{INS} = \begin{pmatrix} \delta\boldsymbol{\psi}^e_{eb} \\ \delta\mathbf{v}^e_{eb} \\ \delta\mathbf{r}^e_{eb} \\ \mathbf{b}_a \\ \mathbf{b}_g \end{pmatrix}, \tag{14.39}$$

where the superscript e is used to denote an ECEF-frame implementation.

As shown in Section 5.3.1, the attitude propagation depends on the Earth rate as well as the gyro measurements. Determination of the attitude error derivative follows its ECI-frame counterpart from (14.16) to (14.22), giving

$$\delta\dot{\boldsymbol{\psi}}^e_{eb} \approx \hat{\mathbf{C}}^e_b\left(\tilde{\boldsymbol{\omega}}^b_{eb} - \boldsymbol{\omega}^b_{eb}\right). \tag{14.40}$$

Splitting this up into gyro measurement and Earth-rate terms, and then applying (5.109) and (5.111),

$$\begin{aligned} \delta\dot{\boldsymbol{\psi}}^e_{eb} &\approx \hat{\mathbf{C}}^e_b\delta\boldsymbol{\omega}^b_{ib} - \hat{\mathbf{C}}^e_b\left(\tilde{\mathbf{C}}^b_e - \mathbf{C}^b_e\right)\boldsymbol{\omega}^e_{ie} \\ &= \hat{\mathbf{C}}^e_b\delta\boldsymbol{\omega}^b_{ib} - \boldsymbol{\Omega}^e_{ie}\delta\boldsymbol{\psi}^e_{eb} \end{aligned}. \tag{14.41}$$

In terms of the Kalman filter states, the expectation of the rate of change of the attitude error is thus

$$\mathrm{E}\left(\delta\dot{\boldsymbol{\psi}}^e_{eb}\right) \approx -\boldsymbol{\Omega}^e_{ie}\delta\boldsymbol{\psi}^e_{eb} + \hat{\mathbf{C}}^e_b\mathbf{b}_g. \tag{14.42}$$

The rate of change of the Earth-referenced velocity is [repeating (5.35)]:

$$\dot{\mathbf{v}}_{eb}^{e} = \mathbf{f}_{ib}^{e} + \mathbf{g}_{b}^{e}\left(\mathbf{r}_{eb}^{e}\right) - 2\boldsymbol{\Omega}_{ie}^{e}\mathbf{v}_{eb}^{e}.$$

Thus, the time derivative of the velocity error is

$$\delta\dot{\mathbf{v}}_{eb}^{e} = \tilde{\mathbf{f}}_{eb}^{e} - \mathbf{f}_{eb}^{e} + \mathbf{g}_{b}^{e}\left(\tilde{\mathbf{r}}_{eb}^{e}\right) - \mathbf{g}_{b}^{e}\left(\mathbf{r}_{eb}^{e}\right) - 2\boldsymbol{\Omega}_{ie}^{e}\left(\tilde{\mathbf{v}}_{eb}^{e} - \mathbf{v}_{eb}^{e}\right). \tag{14.43}$$

Compared to an ECI-frame implementation, this replaces the gravitational term with a gravity term and adds a Coriolis term. By analogy with Section 14.2.2.2, the expectation of the specific force term is

$$\mathrm{E}\left(\tilde{\mathbf{f}}_{ib}^{e} - \mathbf{f}_{ib}^{e}\right) \approx -\left(\hat{\mathbf{C}}_{b}^{e}\hat{\mathbf{f}}_{ib}^{b}\right) \wedge \boldsymbol{\psi}_{eb}^{e} + \hat{\mathbf{C}}_{b}^{e}\mathbf{b}_{a}. \tag{14.44}$$

The gravity error may be expressed as

$$\begin{aligned}\mathbf{g}_{b}^{e}\left(\tilde{\mathbf{r}}_{eb}^{e}\right) - \mathbf{g}_{b}^{e}\left(\mathbf{r}_{eb}^{e}\right) &= \tilde{\boldsymbol{\gamma}}_{ib}^{e} - \boldsymbol{\gamma}_{ib}^{e} - \boldsymbol{\Omega}_{ie}^{e}\boldsymbol{\Omega}_{ie}^{e}\delta\mathbf{r}_{eb}^{e} \\ &\approx -\frac{2\hat{\boldsymbol{\gamma}}_{ib}^{e}}{r_{eS}^{e}(\hat{L}_{b})}\frac{\hat{\mathbf{r}}_{eb}^{e\,\mathrm{T}}}{\left|\hat{\mathbf{r}}_{eb}^{e}\right|}\delta\mathbf{r}_{eb}^{e}\end{aligned}, \tag{14.45}$$

where $\hat{\boldsymbol{\gamma}}_{ib}^{e}$ is given by (2.142), the assumption that $h_b << r_{eS}^{e}$ has been made, and the centrifugal term neglected as it is three orders of magnitude smaller near the Earth's surface.

Substituting (5.107), (14.44), and (14.45) into (14.43) gives the expectation of the time derivative of the velocity error in terms of the Kalman filter states

$$\mathrm{E}\left(\delta\dot{\mathbf{v}}_{eb}^{e}\right) \approx -\left(\hat{\mathbf{C}}_{b}^{e}\hat{\mathbf{f}}_{ib}^{b}\right) \wedge \boldsymbol{\psi}_{eb}^{e} - 2\boldsymbol{\Omega}_{ie}^{e}\delta\mathbf{v}_{eb}^{e} - \frac{2\hat{\boldsymbol{\gamma}}_{ib}^{e}}{r_{eS}^{e}(\hat{L}_{b})}\frac{\hat{\mathbf{r}}_{eb}^{e\,\mathrm{T}}}{\left|\hat{\mathbf{r}}_{eb}^{e}\right|}\delta\mathbf{r}_{eb}^{e} + \hat{\mathbf{C}}_{b}^{e}\mathbf{b}_{a}. \tag{14.46}$$

The time derivative of the position error is the same as for an ECI-frame implementation. Thus,

$$\delta\dot{\mathbf{r}}_{eb}^{e} = \delta\mathbf{v}_{eb}^{e}. \tag{14.47}$$

Substituting (14.42), (14.46), (14.47), and (14.34) into (3.26), the system matrix is

$$\mathbf{F}_{INS}^{e} = \begin{pmatrix} -\boldsymbol{\Omega}_{ie}^{e} & \mathbf{0}_{3} & \mathbf{0}_{3} & \mathbf{0}_{3} & \hat{\mathbf{C}}_{b}^{e} \\ \mathbf{F}_{21}^{e} & -2\boldsymbol{\Omega}_{ie}^{e} & \mathbf{F}_{23}^{e} & \hat{\mathbf{C}}_{b}^{e} & \mathbf{0}_{3} \\ \mathbf{0}_{3} & \mathbf{I}_{3} & \mathbf{0}_{3} & \mathbf{0}_{3} & \mathbf{0}_{3} \\ \mathbf{0}_{3} & \mathbf{0}_{3} & \mathbf{0}_{3} & \mathbf{0}_{3} & \mathbf{0}_{3} \\ \mathbf{0}_{3} & \mathbf{0}_{3} & \mathbf{0}_{3} & \mathbf{0}_{3} & \mathbf{0}_{3} \end{pmatrix}, \tag{14.48}$$

where

$$\mathbf{F}_{21}^{e} = \left[-\left(\hat{\mathbf{C}}_{b}^{e}\hat{\mathbf{f}}_{ib}^{b}\right)\times\right], \qquad \mathbf{F}_{23}^{e} = -\frac{2\hat{\boldsymbol{\gamma}}_{ib}^{e}}{r_{eS}^{e}(\hat{L}_{b})}\frac{\hat{\mathbf{r}}_{eb}^{e\,\mathrm{T}}}{\left|\hat{\mathbf{r}}_{eb}^{e}\right|}. \tag{14.49}$$

Moving from continuous to discrete time, the transition matrix, limited to the first order in $\mathbf{F}\tau_s$, is

$$\boldsymbol{\Phi}_{INS}^{e} \approx \begin{bmatrix} \mathbf{I}_3 - \boldsymbol{\Omega}_{ie}^{e}\tau_s & \mathbf{0}_3 & \mathbf{0}_3 & \mathbf{0}_3 & \hat{\mathbf{C}}_{b}^{e}\tau_s \\ \mathbf{F}_{21}^{e}\tau_s & \mathbf{I}_3 - 2\boldsymbol{\Omega}_{ie}^{e}\tau_s & \mathbf{F}_{23}^{e}\tau_s & \hat{\mathbf{C}}_{b}^{e}\tau_s & \mathbf{0}_3 \\ \mathbf{0}_3 & \mathbf{I}_3\tau_s & \mathbf{I}_3 & \mathbf{0}_3 & \mathbf{0}_3 \\ \mathbf{0}_3 & \mathbf{0}_3 & \mathbf{0}_3 & \mathbf{I}_3 & \mathbf{0}_3 \\ \mathbf{0}_3 & \mathbf{0}_3 & \mathbf{0}_3 & \mathbf{0}_3 & \mathbf{I}_3 \end{bmatrix}. \tag{14.50}$$

A version with terms of up to the third order in $\mathbf{F}\tau_s$ is presented in Section I.1 of Appendix I on the CD. The first-order version of this system model is included in the MATLAB functions, LC_KF_Epoch and TC_KF_Epoch, on the CD.

14.2.4 INS State Propagation Resolved in a Local Navigation Frame

When the Kalman filter-estimated attitude and velocity are Earth-referenced and resolved in a local navigation frame, while the position error is expressed in terms of the latitude, longitude, and height, the state vector becomes

$$\mathbf{x}_{INS}^{n} = \begin{pmatrix} \delta\boldsymbol{\psi}_{nb}^{n} \\ \delta\mathbf{v}_{eb}^{n} \\ \delta\mathbf{p}_{b} \\ \mathbf{b}_{a} \\ \mathbf{b}_{g} \end{pmatrix}, \qquad \delta\mathbf{p}_{b} = \begin{pmatrix} \delta L_{b} \\ \delta\lambda_{b} \\ \delta h_{b} \end{pmatrix}, \tag{14.51}$$

where the superscript n denotes a local-navigation-frame implementation.

As shown in Section 5.4.1, the attitude propagation equations incorporate a transport-rate term in addition to the Earth-rate and gyro-measurement terms. Following its ECI-frame counterpart from (14.16) to (14.22), the attitude error derivative in a local navigation frame is

$$\delta\dot{\boldsymbol{\psi}}_{nb}^{n} \approx \hat{\mathbf{C}}_{b}^{n}\left(\tilde{\boldsymbol{\omega}}_{nb}^{b} - \boldsymbol{\omega}_{nb}^{b}\right). \tag{14.52}$$

Expanding this into gyro-measurement, Earth-rate, and transport-rate terms,

$$\delta\dot{\boldsymbol{\psi}}_{nb}^{n} \approx \hat{\mathbf{C}}_{b}^{n}\delta\boldsymbol{\omega}_{ib}^{b} - \hat{\mathbf{C}}_{b}^{n}\left(\tilde{\boldsymbol{\omega}}_{ie}^{b} - \boldsymbol{\omega}_{ie}^{b}\right) - \hat{\mathbf{C}}_{b}^{n}\left(\tilde{\boldsymbol{\omega}}_{en}^{b} - \boldsymbol{\omega}_{en}^{b}\right). \tag{14.53}$$

Expanding the Earth-rate and transport-rate terms, neglecting products of error states,

$$\begin{aligned}\hat{\mathbf{C}}_b^n\left(\tilde{\boldsymbol{\omega}}_{ie}^b - \boldsymbol{\omega}_{ie}^b\right) + \hat{\mathbf{C}}_b^n\left(\tilde{\boldsymbol{\omega}}_{en}^b - \boldsymbol{\omega}_{en}^b\right) &\approx \hat{\mathbf{C}}_b^n\left(\tilde{\mathbf{C}}_n^b - \mathbf{C}_n^b\right)\left(\hat{\boldsymbol{\omega}}_{ie}^n + \hat{\boldsymbol{\omega}}_{en}^n\right) + \left(\tilde{\boldsymbol{\omega}}_{ie}^n - \boldsymbol{\omega}_{ie}^n\right) + \left(\tilde{\boldsymbol{\omega}}_{en}^n - \boldsymbol{\omega}_{en}^n\right)\\ &\approx \boldsymbol{\Omega}_{in}^n \delta\boldsymbol{\psi}_{nb}^n + \left(\tilde{\boldsymbol{\omega}}_{ie}^n - \boldsymbol{\omega}_{ie}^n\right) + \left(\tilde{\boldsymbol{\omega}}_{en}^n - \boldsymbol{\omega}_{en}^n\right)\end{aligned}. \tag{14.54}$$

From (2.123), the expectation of the Earth-rate error is

$$\mathrm{E}\left(\tilde{\boldsymbol{\omega}}_{ie}^n - \boldsymbol{\omega}_{ie}^n\right) = -\omega_{ie}\begin{pmatrix}\sin\hat{L}_b\\ 0\\ \cos\hat{L}_b\end{pmatrix}\delta L_b. \tag{14.55}$$

From (5.44), neglecting products of error states and the variation of the radii of curvature with latitude, the expectation of the transport-rate error is

$$\begin{aligned}\mathrm{E}\left(\tilde{\boldsymbol{\omega}}_{en}^n - \boldsymbol{\omega}_{en}^n\right) \approx &\begin{bmatrix}\delta v_{eb,E}^n \Big/ \left(R_E(\hat{L}_b) + \hat{h}_b\right)\\ -\delta v_{eb,N}^n \Big/ \left(R_N(\hat{L}_b) + \hat{h}_b\right)\\ -\delta v_{eb,E}^n \tan\hat{L}_b \Big/ \left(R_E(\hat{L}_b) + \hat{h}_b\right)\end{bmatrix} - \begin{pmatrix}0\\0\\1\end{pmatrix}\frac{\hat{v}_{eb,E}^n}{\left(R_E(\hat{L}_b) + \hat{h}_b\right)\cos^2\hat{L}_b}\delta L_b\\ &+\begin{bmatrix}-\hat{v}_{eb,E}^n \Big/ \left(R_E(\hat{L}_b) + \hat{h}_b\right)^2\\ \hat{v}_{eb,N}^n \Big/ \left(R_N(\hat{L}_b) + \hat{h}_b\right)^2\\ \hat{v}_{eb,E}^n \tan\hat{L}_b \Big/ \left(R_E(\hat{L}_b) + \hat{h}_b\right)^2\end{bmatrix}\delta h_b\end{aligned}. \tag{14.56}$$

The rate of change of the velocity, $\mathbf{v}_{eb}^n$, is [repeating (5.53)]:

$$\dot{\mathbf{v}}_{eb}^n = \mathbf{f}_{ib}^n + \mathbf{g}_b^n\left(L_b, h_b\right) - \left(\boldsymbol{\Omega}_{en}^n + 2\boldsymbol{\Omega}_{ie}^n\right)\mathbf{v}_{eb}^n,$$

adding a transport-rate term to the ECEF-frame equivalent. The time derivative of the velocity error is thus

$$\delta\dot{\mathbf{v}}_{eb}^n = \tilde{\mathbf{f}}_{ib}^n - \mathbf{f}_{ib}^n + \mathbf{g}_b^n\left(\tilde{L}_b, \tilde{h}_b\right) - \mathbf{g}_b^n\left(L_b, h_b\right) - \left(\tilde{\boldsymbol{\Omega}}_{en}^n + 2\tilde{\boldsymbol{\Omega}}_{ie}^n\right)\tilde{\mathbf{v}}_{eb}^n + \left(\boldsymbol{\Omega}_{en}^n + 2\boldsymbol{\Omega}_{ie}^n\right)\mathbf{v}_{eb}^n. \tag{14.57}$$

By analogy with Section 14.2.2.2, the expectation of the specific force term is

$$\mathrm{E}\left(\tilde{\mathbf{f}}_{ib}^{n} - \mathbf{f}_{ib}^{n}\right) \approx -\left(\hat{\mathbf{C}}_{b}^{n}\hat{\mathbf{f}}_{ib}^{b}\right) \wedge \boldsymbol{\delta\psi}_{nb}^{n} + \hat{\mathbf{C}}_{b}^{n}\mathbf{b}_{a}. \tag{14.58}$$

The gravity error may be approximated to

$$\mathbf{g}_{b}^{n}\left(\tilde{L}_{b}, \tilde{h}_{b}\right) - \mathbf{g}_{b}^{n}\left(L_{b}, h_{b}\right) \approx -2\frac{g_{0}(\hat{L}_{b})}{r_{eS}^{e}(\hat{L}_{b})}\delta h_{b}\hat{\mathbf{u}}_{D}^{n}, \tag{14.59}$$

where $\hat{\mathbf{u}}_{D}^{n}$ is the local navigation frame down unit vector, $h_b << r_{eS}^{e}$ is assumed, and the centrifugal term and latitude-error dependence have been neglected.

For a linear system model to be valid, the product of any two Kalman filter states must be negligible. Therefore, the Earth-rate and transport-rate terms may be approximated to

$$\begin{aligned}\left(\tilde{\boldsymbol{\Omega}}_{en}^{n} + 2\tilde{\boldsymbol{\Omega}}_{ie}^{n}\right)\tilde{\mathbf{v}}_{eb}^{n} - \left(\boldsymbol{\Omega}_{en}^{n} + 2\boldsymbol{\Omega}_{ie}^{n}\right)\mathbf{v}_{eb}^{n} &\approx \left(\tilde{\boldsymbol{\Omega}}_{en}^{n} - \boldsymbol{\Omega}_{en}^{n}\right)\hat{\mathbf{v}}_{eb}^{n} + 2\left(\tilde{\boldsymbol{\Omega}}_{ie}^{n} - \boldsymbol{\Omega}_{ie}^{n}\right)\hat{\mathbf{v}}_{eb}^{n} + \left(\hat{\boldsymbol{\Omega}}_{en}^{n} + 2\hat{\boldsymbol{\Omega}}_{ie}^{n}\right)\left(\tilde{\mathbf{v}}_{eb}^{n} - \mathbf{v}_{eb}^{n}\right) \\ &= \left(\hat{\boldsymbol{\Omega}}_{en}^{n} + 2\hat{\boldsymbol{\Omega}}_{ie}^{n}\right)\delta\mathbf{v}_{eb}^{n} - \hat{\mathbf{v}}_{eb}^{n} \wedge \left(\tilde{\boldsymbol{\omega}}_{en}^{n} - \boldsymbol{\omega}_{en}^{n}\right) - 2\hat{\mathbf{v}}_{eb}^{n} \wedge \left(\tilde{\boldsymbol{\omega}}_{ie}^{n} - \boldsymbol{\omega}_{ie}^{n}\right)\end{aligned}. \tag{14.60}$$

Substituting (5.107), (14.58), (14.59), and (14.60) into (14.57) gives the expectation of the time derivative of the velocity error in terms of the Kalman filter states:

$$\begin{aligned}\mathrm{E}\left(\delta\dot{\mathbf{v}}_{eb}^{n}\right) \approx\ & -\left(\hat{\mathbf{C}}_{b}^{n}\hat{\mathbf{f}}_{ib}^{b}\right) \wedge \boldsymbol{\delta\psi}_{nb}^{n} - \left(\hat{\boldsymbol{\Omega}}_{en}^{n} + 2\hat{\boldsymbol{\Omega}}_{ie}^{n}\right)\delta\mathbf{v}_{eb}^{n} + \hat{\mathbf{v}}_{eb}^{n} \wedge \mathrm{E}\left(\tilde{\boldsymbol{\omega}}_{en}^{n} - \boldsymbol{\omega}_{en}^{n}\right) \\ & + 2\hat{\mathbf{v}}_{eb}^{n} \wedge \mathrm{E}\left(\tilde{\boldsymbol{\omega}}_{ie}^{n} - \boldsymbol{\omega}_{ie}^{n}\right) - 2\frac{g_{0}(\hat{L}_{b})}{r_{eS}^{e}(\hat{L}_{b})}\hat{\mathbf{u}}_{D}^{n}\delta h_{b} + \hat{\mathbf{C}}_{b}^{n}\mathbf{b}_{a}\end{aligned}. \tag{14.61}$$

From (2.111), the expectation of the time derivative of the position error, neglecting products of error states and the variation of the radii of curvature with latitude, is

$$\begin{aligned}\mathrm{E}\left(\delta\dot{L}_{b}\right) &= \frac{\delta v_{eb,N}^{n}}{R_{N}(\hat{L}_{b}) + \hat{h}_{b}} - \frac{\hat{v}_{eb,N}^{n}\delta h_{b}}{\left(R_{N}(\hat{L}_{b}) + \hat{h}_{b}\right)^{2}} \\ \mathrm{E}\left(\delta\dot{\lambda}_{b}\right) &\approx \frac{\delta v_{eb,E}^{n}}{\left(R_{E}(\hat{L}_{b}) + \hat{h}_{b}\right)\cos\hat{L}_{b}} + \frac{\hat{v}_{eb,E}^{n}\sin\hat{L}_{b}\delta L_{b}}{\left(R_{E}(\hat{L}_{b}) + \hat{h}_{b}\right)\cos^{2}\hat{L}_{b}} - \frac{\hat{v}_{eb,E}^{n}\delta h_{b}}{\left(R_{E}(\hat{L}_{b}) + \hat{h}_{b}\right)^{2}\cos\hat{L}_{b}} \\ \delta\dot{h}_{b} &\approx -\delta v_{eb,D}^{n}\end{aligned}. \tag{14.62}$$

Substituting (14.53) to (14.56), (14.61), (14.62), and (14.34) into (3.26), the system matrix is

$$\mathbf{F}_{INS}^{n} = \begin{pmatrix} \mathbf{F}_{11}^{n} & \mathbf{F}_{12}^{n} & \mathbf{F}_{13}^{n} & \mathbf{0}_3 & \hat{\mathbf{C}}_b^n \\ \mathbf{F}_{21}^{n} & \mathbf{F}_{22}^{n} & \mathbf{F}_{23}^{n} & \hat{\mathbf{C}}_b^n & \mathbf{0}_3 \\ \mathbf{0}_3 & \mathbf{F}_{32}^{n} & \mathbf{F}_{33}^{n} & \mathbf{0}_3 & \mathbf{0}_3 \\ \mathbf{0}_3 & \mathbf{0}_3 & \mathbf{0}_3 & \mathbf{0}_3 & \mathbf{0}_3 \\ \mathbf{0}_3 & \mathbf{0}_3 & \mathbf{0}_3 & \mathbf{0}_3 & \mathbf{0}_3 \end{pmatrix}, \tag{14.63}$$

where

$$\mathbf{F}_{11}^{n} = -\left[\hat{\boldsymbol{\omega}}_{in}^{n} \wedge\right], \tag{14.64}$$

$$\mathbf{F}_{12}^{n} = \begin{bmatrix} 0 & \dfrac{-1}{R_E(\hat{L}_b) + \hat{h}_b} & 0 \\ \dfrac{1}{R_N(\hat{L}_b) + \hat{h}_b} & 0 & 0 \\ 0 & \dfrac{\tan \hat{L}_b}{R_E(\hat{L}_b) + \hat{h}_b} & 0 \end{bmatrix}, \tag{14.65}$$

$$\mathbf{F}_{13}^{n} = \begin{bmatrix} \omega_{ie} \sin \hat{L}_b & 0 & \dfrac{\hat{v}_{eb,E}^{n}}{\left(R_E(\hat{L}_b) + \hat{h}_b\right)^2} \\ 0 & 0 & \dfrac{-\hat{v}_{eb,N}^{n}}{\left(R_N(\hat{L}_b) + \hat{h}_b\right)^2} \\ \omega_{ie} \cos \hat{L}_b + \dfrac{\hat{v}_{eb,E}^{n}}{\left(R_E(\hat{L}_b) + \hat{h}_b\right) \cos^2 \hat{L}_b} & 0 & \dfrac{-\hat{v}_{eb,E}^{n} \tan \hat{L}_b}{\left(R_E(\hat{L}_b) + \hat{h}_b\right)^2} \end{bmatrix}, \tag{14.66}$$

$$\mathbf{F}_{21}^{n} = -\left[\left(\hat{\mathbf{C}}_b^n \hat{\mathbf{f}}_{ib}^{b}\right) \wedge\right], \tag{14.67}$$

$$\mathbf{F}_{22}^{n} = \begin{bmatrix} \dfrac{\hat{v}_{eb,D}^{n}}{R_N(\hat{L}_b) + \hat{h}_b} & -\dfrac{2\hat{v}_{eb,E}^{n} \tan \hat{L}_b}{R_E(\hat{L}_b) + \hat{h}_b} - 2\omega_{ie} \sin \hat{L}_b & \dfrac{\hat{v}_{eb,N}^{n}}{R_N(\hat{L}_b) + \hat{h}_b} \\ \dfrac{\hat{v}_{eb,E}^{n} \tan \hat{L}_b}{R_E(\hat{L}_b) + \hat{h}_b} + 2\omega_{ie} \sin \hat{L}_b & \dfrac{\hat{v}_{eb,N}^{n} \tan \hat{L}_b + \hat{v}_{eb,D}^{n}}{R_E(\hat{L}_b) + \hat{h}_b} & \dfrac{\hat{v}_{eb,E}^{n}}{R_E(\hat{L}_b) + \hat{h}_b} + 2\omega_{ie} \cos \hat{L}_b \\ -\dfrac{2\hat{v}_{eb,N}^{n}}{R_N(\hat{L}_b) + \hat{h}_b} & -\dfrac{2\hat{v}_{eb,E}^{n}}{R_E(\hat{L}_b) + \hat{h}_b} - 2\omega_{ie} \cos \hat{L}_b & 0 \end{bmatrix}, \tag{14.68}$$

$$\mathbf{F}_{23}^{n} = \begin{bmatrix} -\dfrac{(\hat{v}_{eb,E}^{n})^2 \sec^2 \hat{L}_b}{R_E(\hat{L}_b) + \hat{h}_b} - 2\hat{v}_{eb,E}^{n}\omega_{ie}\cos\hat{L}_b & 0 & \dfrac{(\hat{v}_{eb,E}^{n})^2 \tan\hat{L}_b}{\left(R_E(\hat{L}_b) + \hat{h}_b\right)^2} - \dfrac{\hat{v}_{eb,N}^{n}\hat{v}_{eb,D}^{n}}{\left(R_N(\hat{L}_b) + \hat{h}_b\right)^2} \\ \begin{pmatrix} \dfrac{\hat{v}_{eb,N}^{n}\hat{v}_{eb,E}^{n}\sec^2\hat{L}_b}{R_E(\hat{L}_b) + \hat{h}_b} + 2\hat{v}_{eb,N}^{n}\omega_{ie}\cos\hat{L}_b \\ -2\hat{v}_{eb,D}^{n}\omega_{ie}\sin\hat{L}_b \end{pmatrix} & 0 & -\dfrac{\hat{v}_{eb,N}^{n}\hat{v}_{eb,E}^{n}\tan\hat{L}_b + \hat{v}_{eb,E}^{n}\hat{v}_{eb,D}^{n}}{\left(R_E(\hat{L}_b) + \hat{h}_b\right)^2} \\ 2\hat{v}_{eb,E}^{n}\omega_{ie}\sin\hat{L}_b & 0 & \dfrac{(\hat{v}_{eb,E}^{n})^2}{\left(R_E(\hat{L}_b) + \hat{h}_b\right)^2} + \dfrac{(\hat{v}_{eb,N}^{n})^2}{\left(R_N(\hat{L}_b) + \hat{h}_b\right)^2} - \dfrac{2g_0(\hat{L}_b)}{r_{eS}^{e}(\hat{L}_b)} \end{bmatrix}, \tag{14.69}$$

$$\mathbf{F}_{32}^{n} = \begin{bmatrix} \dfrac{1}{R_N(\hat{L}_b) + \hat{h}_b} & 0 & 0 \\ 0 & \dfrac{1}{\left(R_E(\hat{L}_b) + \hat{h}_b\right)\cos\hat{L}_b} & 0 \\ 0 & 0 & -1 \end{bmatrix}, \tag{14.70}$$

$$\mathbf{F}_{33}^{n} = \begin{bmatrix} 0 & 0 & -\dfrac{\hat{v}_{eb,N}^{n}}{\left(R_N(\hat{L}_b) + \hat{h}_b\right)^2} \\ \dfrac{\hat{v}_{eb,E}^{n}\sin\hat{L}_b}{\left(R_E(\hat{L}_b) + \hat{h}_b\right)\cos^2\hat{L}_b} & 0 & -\dfrac{\hat{v}_{eb,E}^{n}}{\left(R_E(\hat{L}_b) + \hat{h}_b\right)^2\cos\hat{L}_b} \\ 0 & 0 & 0 \end{bmatrix}. \tag{14.71}$$

Moving from continuous to discrete time, the transition matrix, limited to first order in $\mathbf{F}\tau_s$, is

$$\boldsymbol{\Phi}_{INS}^{n} \approx \begin{bmatrix} \mathbf{I}_3 + \mathbf{F}_{11}^{n}\tau_s & \mathbf{F}_{12}^{n}\tau_s & \mathbf{F}_{13}^{n}\tau_s & \mathbf{0}_3 & \hat{\mathbf{C}}_b^{n}\tau_s \\ \mathbf{F}_{21}^{n}\tau_s & \mathbf{I}_3 + \mathbf{F}_{22}^{n}\tau_s & \mathbf{F}_{23}^{n}\tau_s & \hat{\mathbf{C}}_b^{n}\tau_s & \mathbf{0}_3 \\ \mathbf{0}_3 & \mathbf{F}_{32}^{n}\tau_s & \mathbf{I}_3 + \mathbf{F}_{33}^{n}\tau_s & \mathbf{0}_3 & \mathbf{0}_3 \\ \mathbf{0}_3 & \mathbf{0}_3 & \mathbf{0}_3 & \mathbf{I}_3 & \mathbf{0}_3 \\ \mathbf{0}_3 & \mathbf{0}_3 & \mathbf{0}_3 & \mathbf{0}_3 & \mathbf{I}_3 \end{bmatrix}. \tag{14.72}$$

A version with terms of up to third order in $\mathbf{F}\tau_s$ is presented in Section I.1 of Appendix I on the CD.

When consumer-grade inertial sensors are used, the gyro errors will greatly exceed the Earth rate and transport rate, enabling these terms to be neglected in

the system model [31]. The approximated system matrix is similar to its ECI-frame counterpart:

$$\mathbf{F}_{INS}^{\prime n} \approx \begin{pmatrix} \mathbf{0}_3 & \mathbf{0}_3 & \mathbf{0}_3 & \mathbf{0}_3 & \hat{\mathbf{C}}_b^n \\ \mathbf{F}_{21}^n & \mathbf{0}_3 & \mathbf{F}_{23}^{\prime n} & \hat{\mathbf{C}}_b^n & \mathbf{0}_3 \\ \mathbf{0}_3 & \mathbf{F}_{32}^n & \mathbf{0}_3 & \mathbf{0}_3 & \mathbf{0}_3 \\ \mathbf{0}_3 & \mathbf{0}_3 & \mathbf{0}_3 & \mathbf{0}_3 & \mathbf{0}_3 \\ \mathbf{0}_3 & \mathbf{0}_3 & \mathbf{0}_3 & \mathbf{0}_3 & \mathbf{0}_3 \end{pmatrix} \qquad \mathbf{F}_{23}^{\prime n} = -\frac{2g_0(\hat{L}_b)}{r_{eS}^e(\hat{L}_b)} \begin{pmatrix} 0 & 0 & 0 \\ 0 & 0 & 0 \\ 0 & 0 & 1 \end{pmatrix}, \tag{14.73}$$

Section I.2 of Appendix I on the CD presents an alternative formulation of local-navigation-frame INS/GNSS integration with Cartesian position error states, while Section I.3 presents a wander-azimuth-frame implementation.

14.2.5 Additional IMU Error States

Where estimated, the scale-factor, cross-coupling, and g-dependent errors are typically modeled with no deterministic time variation. Thus,

$$\mathrm{E}\left(\dot{\mathbf{M}}_a\right) = \mathbf{0}_3, \qquad \mathrm{E}\left(\dot{\mathbf{M}}_g\right) = \mathbf{0}_3, \qquad \mathrm{E}\left(\dot{\mathbf{G}}_g\right) = \mathbf{0}_3, \tag{14.74}$$

where $\mathbf{M}_a$ is the accelerometer scale-factor and cross-coupling error matrix, $\mathbf{M}_g$ is the gyro scale-factor and cross-coupling error matrix, and $\mathbf{G}_g$ is the gyro g-dependent error matrix, as defined in Section 4.4.

The additional IMU error states lead to additional terms in the attitude and velocity error models as follows:

$$\mathrm{E}\left(\delta\dot{\boldsymbol{\psi}}_{\gamma b}^{\gamma}\right) \rightarrow \mathrm{E}\left(\delta\dot{\boldsymbol{\psi}}_{\gamma b}^{\gamma}\right) + \hat{\mathbf{C}}_b^{\gamma}\mathbf{M}_g\hat{\boldsymbol{\omega}}_{ib}^b + \hat{\mathbf{C}}_b^{\gamma}\mathbf{G}_g\hat{\mathbf{f}}_{ib}^b, \tag{14.75}$$

$$\mathrm{E}\left(\delta\dot{\mathbf{v}}_{\beta b}^{\gamma}\right) \rightarrow \mathrm{E}\left(\delta\dot{\mathbf{v}}_{\beta b}^{\gamma}\right) + \hat{\mathbf{C}}_b^{\gamma}\mathbf{M}_a\hat{\mathbf{f}}_{ib}^b, \tag{14.76}$$

where γ and β are defined by (14.5).

When the accelerometer scale-factor and cross-coupling errors and gyro g-dependent errors are not estimated as Kalman filter states, the product of these errors with the reaction to gravity (i.e., the average specific force) will perturb the accelerometer and gyro bias estimates. This need not be a problem, particularly for low-dynamics applications, provided the initial uncertainties of the bias states are sufficient.

The accelerometer and gyro biases may be split into separate static and dynamic states using [repeating (4.13)]

$$\begin{aligned} \mathbf{b}_a &= \mathbf{b}_{as} + \mathbf{b}_{ad} \\ \mathbf{b}_g &= \mathbf{b}_{gs} + \mathbf{b}_{gd} \end{aligned}.$$

The static bias states, $\mathbf{b}_{as}$ and $\mathbf{b}_{gs}$, are modeled with zero known time variation:

$$\mathrm{E}\left(\dot{\mathbf{b}}_{as}\right) = 0, \qquad \mathrm{E}\left(\dot{\mathbf{b}}_{gs}\right) = 0, \tag{14.77}$$

whereas the dynamic bias states, $\mathbf{b}_{ad}$ and $\mathbf{b}_{gd}$, should be modeled as exponentially correlated fixed-variance first-order Markov processes (see Section B.4.3 of Appendix B on the CD). Their deterministic time variation is then

$$\mathrm{E}\left(\dot{\mathbf{b}}_{ad}\right) = -\frac{\mathbf{b}_{ad}}{\tau_{bad}}, \qquad \mathrm{E}\left(\dot{\mathbf{b}}_{gd}\right) = -\frac{\mathbf{b}_{gd}}{\tau_{bgd}}, \tag{14.78}$$

where τ_{bad} and τ_{bgd} are the correlation times of the dynamic accelerometer and gyro biases, respectively. Note that these states will absorb vibration rectification errors (see Section 4.4.5) as well as variation in the sensor biases themselves.

Modeling of selected higher order IMU errors is described in [3].

When gravity-modeling errors are estimated, they should also be modeled as exponentially correlated fixed-variance first-order Markov processes with velocity-dependent correlation times to account for the fact that these errors are spatially, as opposed to temporally, correlated. When a precision gravity model is used, the local variation in gravity not accounted for by the model has a standard deviation of about 2×10^{-4} m s^{-2} per axis and a correlation length of about 40 km [30].

14.2.6 INS System Noise

The main sources of system noise on the inertial navigation solution are random walk of the velocity error due to noise on the accelerometer specific-force measurements and random walk of the attitude error due to noise on the gyro angular-rate measurements. IMU random noise is discussed in Section 4.4.3. In addition, where separate accelerometer and gyro dynamic bias states are not estimated, the in-run variation of the accelerometer and gyro biases (Section 4.4.1) can be approximated as white noise.

From (3.43), the system noise covariance is obtained by integrating the power spectral densities of these noise sources over the state propagation interval, accounting for the deterministic system model. Thus, assuming 15 states are estimated as defined by (14.15), (14.39), or (14.51), the INS system noise covariance matrix, $\mathbf{Q}_{INS}$, is

$$\mathbf{Q}_{INS}^{\gamma} = \int_0^{\tau_s} \exp\left(\mathbf{F}_{INS}^{\gamma} t'\right) \begin{pmatrix} S_{rg}\mathbf{I}_3 & \mathbf{0}_3 & \mathbf{0}_3 & \mathbf{0}_3 & \mathbf{0}_3 \\ \mathbf{0}_3 & S_{ra}\mathbf{I}_3 & \mathbf{0}_3 & \mathbf{0}_3 & \mathbf{0}_3 \\ \mathbf{0}_3 & \mathbf{0}_3 & \mathbf{0}_3 & \mathbf{0}_3 & \mathbf{0}_3 \\ \mathbf{0}_3 & \mathbf{0}_3 & \mathbf{0}_3 & S_{bad}\mathbf{I}_3 & \mathbf{0}_3 \\ \mathbf{0}_3 & \mathbf{0}_3 & \mathbf{0}_3 & \mathbf{0}_3 & S_{bgd}\mathbf{I}_3 \end{pmatrix} \exp\left(\mathbf{F}_{INS}^{\gamma\,\mathrm{T}} t'\right) \mathrm{d}t' \qquad \gamma \in i,e,n, \tag{14.79}$$

where S_{rg}, S_{ra}, S_{bad}, and S_{bgd} are the power spectral densities of, respectively, the gyro random noise, accelerometer random noise, accelerometer bias variation, and gyro bias variation, and it is assumed that all gyros and all accelerometers have equal noise characteristics.

Assuming the PSDs are constant and substituting in (14.35), (14.48), and (14.63) give an exact system noise covariance of

$$\mathbf{Q}_{INS}^{\gamma} = \begin{pmatrix} \mathbf{Q}_{11} & \mathbf{Q}_{21}^{\gamma\,\mathrm{T}} & \mathbf{Q}_{31}^{\gamma\,\mathrm{T}} & \mathbf{0}_3 & \frac{1}{2}S_{bgd}\tau_s^2\hat{\mathbf{C}}_b^{\gamma} \\ \mathbf{Q}_{21}^{\gamma} & \mathbf{Q}_{22}^{\gamma} & \mathbf{Q}_{32}^{\gamma\,\mathrm{T}} & \frac{1}{2}S_{bad}\tau_s^2\hat{\mathbf{C}}_b^{\gamma} & \frac{1}{3}S_{bgd}\tau_s^3\mathbf{F}_{21}^{\gamma}\hat{\mathbf{C}}_b^{\gamma} \\ \mathbf{Q}_{31}^{\gamma} & \mathbf{Q}_{32}^{\gamma} & \mathbf{Q}_{33}^{\gamma} & \mathbf{Q}_{34}^{\gamma} & \mathbf{Q}_{35}^{\gamma} \\ \mathbf{0}_3 & \frac{1}{2}S_{bad}\tau_s^2\hat{\mathbf{C}}_{\gamma}^{b} & \mathbf{Q}_{34}^{\gamma\,\mathrm{T}} & S_{bad}\tau_s\mathbf{I}_3 & \mathbf{0}_3 \\ \frac{1}{2}S_{bgd}\tau_s^2\hat{\mathbf{C}}_{\gamma}^{b} & \frac{1}{3}S_{bgd}\tau_s^3\mathbf{F}_{21}^{\gamma\,\mathrm{T}}\hat{\mathbf{C}}_{\gamma}^{b} & \mathbf{Q}_{35}^{\gamma\,\mathrm{T}} & \mathbf{0}_3 & S_{bgd}\tau_s\mathbf{I}_3 \end{pmatrix}, \qquad \gamma \in i,e,n, \tag{14.80}$$

where

$$\begin{aligned}
\mathbf{Q}_{11} &= \left(S_{rg}\tau_s + \tfrac{1}{3}S_{bgd}\tau_s^3\right)\mathbf{I}_3 \\
\mathbf{Q}_{21}^{\gamma} &= \left(\tfrac{1}{2}S_{rg}\tau_s^2 + \tfrac{1}{4}S_{bgd}\tau_s^4\right)\mathbf{F}_{21}^{\gamma} \\
\mathbf{Q}_{22}^{\gamma} &= \left(S_{ra}\tau_s + \tfrac{1}{3}S_{bad}\tau_s^3\right)\mathbf{I}_3 + \left(\tfrac{1}{3}S_{rg}\tau_s^3 + \tfrac{1}{5}S_{bgd}\tau_s^5\right)\mathbf{F}_{21}^{\gamma}\mathbf{F}_{21}^{\gamma\,\mathrm{T}} \\
\mathbf{Q}_{31}^{i/e} &= \left(\tfrac{1}{3}S_{rg}\tau_s^3 + \tfrac{1}{5}S_{bgd}\tau_s^5\right)\mathbf{F}_{21}^{i/e} \\
\mathbf{Q}_{31}^{n} &= \left(\tfrac{1}{3}S_{rg}\tau_s^3 + \tfrac{1}{5}S_{bgd}\tau_s^5\right)\mathbf{T}_{r(n)}^{p}\mathbf{F}_{21}^{n} \\
\mathbf{Q}_{32}^{i/e} &= \left(\tfrac{1}{2}S_{ra}\tau_s^2 + \tfrac{1}{4}S_{bad}\tau_s^4\right)\mathbf{I}_3 + \left(\tfrac{1}{4}S_{rg}\tau_s^4 + \tfrac{1}{6}S_{bgd}\tau_s^6\right)\mathbf{F}_{21}^{i/e}\mathbf{F}_{21}^{i/e\,\mathrm{T}} \\
\mathbf{Q}_{32}^{n} &= \left(\tfrac{1}{2}S_{ra}\tau_s^2 + \tfrac{1}{4}S_{bad}\tau_s^4\right)\mathbf{T}_{r(n)}^{p} + \left(\tfrac{1}{4}S_{rg}\tau_s^4 + \tfrac{1}{6}S_{bgd}\tau_s^6\right)\mathbf{T}_{r(n)}^{p}\mathbf{F}_{21}^{n}\mathbf{F}_{21}^{n\,\mathrm{T}} \qquad \gamma \in i,e,n \\
\mathbf{Q}_{33}^{i/e} &= \left(\tfrac{1}{3}S_{ra}\tau_s^3 + \tfrac{1}{5}S_{bad}\tau_s^5\right)\mathbf{I}_3 + \left(\tfrac{1}{5}S_{rg}\tau_s^5 + \tfrac{1}{7}S_{bgd}\tau_s^7\right)\mathbf{F}_{21}^{i/e}\mathbf{F}_{21}^{i/e\;\mathrm{T}} \\
\mathbf{Q}_{33}^{n} &= \left(\tfrac{1}{3}S_{ra}\tau_s^3 + \tfrac{1}{5}S_{bad}\tau_s^5\right)\mathbf{T}_{r(n)}^{p}\mathbf{T}_{r(n)}^{p} + \left(\tfrac{1}{5}S_{rg}\tau_s^5 + \tfrac{1}{7}S_{bgd}\tau_s^7\right)\mathbf{T}_{r(n)}^{p}\mathbf{F}_{21}^{n}\mathbf{F}_{21}^{n\,\mathrm{T}}\mathbf{T}_{r(n)}^{p} \\
\mathbf{Q}_{34}^{i/e} &= \tfrac{1}{3}S_{bad}\tau_s^3\hat{\mathbf{C}}_b^{\gamma} \\
\mathbf{Q}_{34}^{n} &= \tfrac{1}{3}S_{bad}\tau_s^3\mathbf{T}_{r(n)}^{p}\hat{\mathbf{C}}_b^{n} \\
\mathbf{Q}_{35}^{i/e} &= \tfrac{1}{4}S_{bgd}\tau_s^4\mathbf{F}_{21}^{i/e}\hat{\mathbf{C}}_b^{\gamma} \\
\mathbf{Q}_{35}^{n} &= \tfrac{1}{4}S_{bgd}\tau_s^4\mathbf{T}_{r(n)}^{p}\mathbf{F}_{21}^{n}\hat{\mathbf{C}}_b^{n}
\end{aligned} \tag{14.81}$$

and $\mathbf{T}_{r(n)}^{p}$ is given by (2.119).

For small propagation intervals ($\tau_s \leq 0.2$ second), the system noise covariance matrix may be approximated to

$$\mathbf{Q}_{INS}^{\gamma} \approx \mathbf{Q}_{INS}^{\gamma} = \begin{pmatrix} S_{rg}\mathbf{I}_3 & \mathbf{0}_3 & \mathbf{0}_3 & \mathbf{0}_3 & \mathbf{0}_3 \\ \mathbf{0}_3 & S_{ra}\mathbf{I}_3 & \mathbf{0}_3 & \mathbf{0}_3 & \mathbf{0}_3 \\ \mathbf{0}_3 & \mathbf{0}_3 & \mathbf{0}_3 & \mathbf{0}_3 & \mathbf{0}_3 \\ \mathbf{0}_3 & \mathbf{0}_3 & \mathbf{0}_3 & S_{bad}\mathbf{I}_3 & \mathbf{0}_3 \\ \mathbf{0}_3 & \mathbf{0}_3 & \mathbf{0}_3 & \mathbf{0}_3 & S_{bgd}\mathbf{I}_3 \end{pmatrix} \tau_s, \quad \gamma \in i,e,n. \tag{14.82}$$

This approximation may also be used in conjunction with (3.46) for longer propagation intervals. This version of the system noise covariance model is included in the MATLAB functions, LC_KF_Epoch and TC_KF_Epoch, on the CD.

If σ_{ra} is the standard deviation of the noise on the accelerometer specific-force measurements and σ_{rg} is the standard deviation of the noise on the gyro angular-rate measurements, then the PSDs of the accelerometer and gyro noise are

$$S_{ra} = \sigma_{ra}^2 \tau_i, \qquad S_{rg} = \sigma_{rg}^2 \tau_i, \tag{14.83}$$

where τ_i is the interval between the input of successive accelerometer and gyro outputs to the inertial navigation equations. Note that vibration can significantly increase the effective sensor noise, particularly for MEMS sensors. The PSDs should either be sufficiently large to account for the maximum likely level of vibration or modeled as a function of the vibration level measured by the IMU.

Similarly, the bias variation PSDs are

$$S_{bad} = \frac{\sigma_{bad}^2}{\tau_{bad}}, \qquad S_{bgd} = \frac{\sigma_{bgd}^2}{\tau_{bgd}}, \tag{14.84}$$

where σ_{bad} and σ_{bgd} are the standard deviations of the accelerometer and gyro dynamic biases, respectively. These should account for the VREs (see Section 4.4.5) as well as variation in the sensor biases themselves. Vibration-dependent models are an option.

Sufficient system noise must be modeled on the horizontal attitude error and vertical accelerometer bias states to account for the spatial variation of the gravity-modeling errors where these are not estimated as states.

When errors such as the accelerometer and gyro scale factor, cross-coupling, and g-dependent errors are not modeled either as states or correlated system noise, their effects may be rather crudely approximated by increasing the modeled accelerometer and gyro random noise. A similar approach may be adopted for higher-order sensor errors. To account for these errors more effectively, sensor noise PSDs may be modeled as functions of acceleration and angular rate. Note that the product of these errors sources with the reaction to gravity is usually absorbed by the bias states. To maintain Kalman filter stability, these white noise approximations must overbound the true impact on the Kalman filter states. When the higher-order IMU errors are estimated as states, a certain level of system noise on the states should be modeled to account for any in-run variation.

The system noise variance for a state, x_{mi}, modeled as an exponentially correlated fixed-variance first-order Markov process is

$$Q_{mi} = \left[1 - \exp\left(-2\tau_s/\tau_{mi}\right)\right]\sigma_{mi}^2, \tag{14.85}$$

where σ_{mi} is the standard deviation of the state and τ_{mi} is the correlation time. This is applicable to estimation of the accelerometer and gyro dynamic biases.

The preceding discussion assumes that the PSDs are independent of frequency as a Kalman filter assumes that all noise sources are white. However, the true PSDs will vary with frequency. The assumed PSDs are therefore approximations.

An estimate of the system noise covariance can be obtained from the sensor manufacturer's specifications and knowledge of the dynamics and vibration likely to be encountered for the application in question. However, for best results, a semi-empirical approach should be adopted. This is particularly important where system noise is used to account for unmodeled systematic errors. Testing with data recorded under a range of representative conditions should be conducted to enable the overall integrated INS/GNSS performance to be compared with different system noise coefficients. Laboratory tests of the IMU under representative dynamics and vibration may also be conducted where suitable equipment is available.

Advanced system noise modeling is discussed in Section 14.4.5.

14.2.7 GNSS State Propagation and System Noise

When the receiver clock offset and drift are estimated, the state dynamics from (9.146) are

$$\frac{\partial}{\partial t}\delta\rho_c^a = \delta\dot{\rho}_c^a, \qquad \mathrm{E}\left(\frac{\partial}{\partial t}\delta\dot{\rho}_c^a\right) = 0, \tag{14.86}$$

giving

$$\mathbf{\Phi}_{GNSS} = \begin{pmatrix} 1 & 0 \\ \tau_s & 1 \end{pmatrix}. \tag{14.87}$$

As described in Section 9.4.2.2, the exact system noise covariance for these states is

$$\mathbf{Q}_{GNSS} = \begin{pmatrix} S_{c\phi}^a\tau_s + \frac{1}{3}S_{cf}^a\tau_s^3 & \frac{1}{2}S_{cf}^a\tau_s^2 \\ \frac{1}{2}S_{cf}^a\tau_s^2 & S_{cf}^a\tau_s \end{pmatrix}, \tag{14.88}$$

where S_{cf}^a is the receiver clock frequency drift PSD (in units of $m^2\ s^{-3}$) and $S_{c\phi}^a$ is the phase drift PSD (in units of $m^2\ s^{-1}$). For small propagation intervals and for use in conjunction with (3.46), this may be approximated to

$$\mathbf{Q}_{GNSS} \approx \mathbf{Q}'_{GNSS} = \begin{pmatrix} S^a_{c\phi}\tau_s & 0 \\ 0 & S^a_{cf}\tau_s \end{pmatrix}. \tag{14.89}$$

Typical values for a TCXO are $S^a_{cf} \approx 0.04$ m^2 s^{-3} and $S^a_{c\phi} \approx 0.01$ m^2 s^{-1} [32]. This GNSS system model is included in the MATLAB functions, LC_KF_Epoch and TC_KF_Epoch, on the CD.

When the clock g-dependent error coefficients, $\mathbf{s}^a_{cg}$, are also estimated, the expectation of the clock offset derivative is

$$\mathrm{E}\left(\frac{\partial}{\partial t}\delta\rho^a_c\right) = \delta\dot{\rho}^a_c + \hat{\mathbf{f}}^{b\mathrm{T}}_{ib}\mathbf{s}^a_{cg}, \tag{14.90}$$

where it is assumed that the axes of the receiver's reference oscillator are fixed with respect to the IMU. The g-dependent error coefficients may be assumed constant, so there is no physical requirement to model system noise on these states. However, a small amount of system noise is useful for maintaining numerical stability.

When they are included, ionosphere and range-bias states should be modeled as exponentially correlated fixed-variance first-order Markov processes as described by (3.3), with the system noise given by (14.85). The standard deviation of ionosphere states should be modeled as a function of satellite elevation angle and local time as discussed in Section 9.3.2. A correlation time of around 30 minutes is suitable. An elevation-dependent standard deviation is also suitable for the range-bias states, while the choice of correlation time depends on whether they are intended primarily to capture the ephemeris, satellite clock, ionosphere, and troposphere errors, demanding a long correlation time, or the multipath and NLOS errors, demanding a much smaller correlation time. When both types of errors are important, separate states can be used.

14.2.8 State Initialization

In an error-state implementation of INS/GNSS integration, the state estimates should generally be initialized at zero. An exception is the GNSS receiver clock offset and drift estimates in tightly- and deeply-coupled integration, which should be initialized using a GNSS navigation solution (either single-epoch or filtered, see Section 9.4). This is to avoid numerical problems arising from large disparities between the different state uncertainties.

The initial error covariance, $\mathbf{P}_0$, should reflect the state uncertainties and any covariance between state residuals as accurately as possible. When the position, velocity, and receiver clock solution are initialized from GNSS, the GNSS solution error covariance matrix, where available, should be used to initialize the relevant components of $\mathbf{P}_0$. Otherwise, when the satellite lines of sight are known, the error covariance may be estimated from the geometry matrix, $\mathbf{H}_G$, (see Section 9.4.3) using

$$\mathrm{E}\left[\begin{pmatrix} \delta\delta\mathbf{r}^\gamma_{\beta b} \\ \delta\delta\rho^a_c \end{pmatrix}\begin{pmatrix} \delta\delta\mathbf{r}^\gamma_{\beta b} \\ \delta\delta\rho^a_c \end{pmatrix}^{\mathrm{T}}\right] = \left(\mathbf{H}^{\gamma\mathrm{T}}_G\mathbf{H}^\gamma_G\right)\sigma^2_\rho, \qquad \mathrm{E}\left[\begin{pmatrix} \delta\delta\mathbf{v}^\gamma_{\beta b} \\ \delta\delta\dot{\rho}^a_c \end{pmatrix}\begin{pmatrix} \delta\delta\mathbf{v}^\gamma_{\beta b} \\ \delta\delta\dot{\rho}^a_c \end{pmatrix}^{\mathrm{T}}\right] = \left(\mathbf{H}^{\gamma\mathrm{T}}_G\mathbf{H}^\gamma_G\right)\sigma^2_r, \tag{14.91}$$

where σ_ρ and σ_r are, respectively, the estimated pseudo-range and pseudo-range rate error standard deviations, the leading δ denotes the state residual (see Section 3.2.1), and β and γ are given by (14.5). The choice of σ_ρ and σ_r depends on the GNSS user equipment design and operating environment. Suitably conservative values for most applications are $\sigma_\rho = 5$m and $\sigma_r = 0.05$ m s^{-1}.

Another common approach is to simply assume equal values for each component of the position and velocity uncertainty and zero off-diagonal covariance. Typical values are 10m for the clock offset uncertainty and each component of the position uncertainty and 0.1 m s^{-1} for the clock drift uncertainty and each component of the velocity uncertainty. For local-navigation-frame implementations, uncertainties a factor of two larger may be assumed for the vertical components.

From (2.118), the curvilinear position error covariance may be determined using

$$\mathrm{E}\left[\begin{pmatrix} \delta\delta\mathbf{p}_b \\ \delta\delta\rho_c^a \end{pmatrix}\begin{pmatrix} \delta\delta\mathbf{p}_b \\ \delta\delta\rho_c^a \end{pmatrix}^{\mathrm{T}}\right] = \begin{pmatrix} \mathbf{T}_{r(n)}^p & \mathbf{0}_{3\times1} \\ \mathbf{0}_{1\times3} & 1 \end{pmatrix}\mathrm{E}\left[\begin{pmatrix} \delta\delta\mathbf{r}_{eb}^n \\ \delta\delta\rho_c^a \end{pmatrix}\begin{pmatrix} \delta\delta\mathbf{r}_{eb}^n \\ \delta\delta\rho_c^a \end{pmatrix}^{\mathrm{T}}\right]\begin{pmatrix} \mathbf{T}_{r(n)}^p & \mathbf{0}_{3\times1} \\ \mathbf{0}_{1\times3} & 1 \end{pmatrix} \tag{14.92}$$

where $\mathbf{T}_{r(n)}^p$ is given by (2.119).

The position, velocity, and receiver clock states are easy to observe and converge quickly. Consequently, integration algorithm performance is not especially sensitive to the initial uncertainties of these states, provided they are not excessively large or small. The initial attitude and IMU error uncertainties have more impact.

Manufacturers' specifications may be used to guide the selection of the initial IMU error uncertainties. However, experimental tests should also be carried out as the sensor specifications are not always complete and the effective sensor performance can vary significantly with the vibration environment. Typical errors for different types of inertial sensor are discussed in Section 4.4.

Heading initialization techniques are described in Sections 5.6.2, 6.1, 15.1, and 15.2.1. Different techniques suit different applications and the accuracy varies with the environment and sensor quality. When the initial heading uncertainty exceeds about 2° or 35 mrad, large heading error Kalman filter implementations (Section 14.4.4) should be considered.

Roll and pitch attitude is typically initialized by accelerometer leveling (Section 5.6.2). Therefore, the initial roll and pitch uncertainties in radians are approximately the same as the accelerometer bias uncertainties in g units. However, the leveling process introduces correlation between the attitude errors and accelerometer biases. From (5.102), the initial roll and pitch errors, respectively, $\delta\phi_{nb}$ and $\delta\theta_{nb}$, may be expressed in terms of the accelerometer biases using

$$\begin{aligned} \delta\phi_{nb} &= \frac{f_{ib,z}^b b_{a,y} - f_{ib,y}^b b_{a,z}}{{f_{ib,y}^b}^2 + {f_{ib,z}^b}^2} \\ \delta\theta_{nb} &= \frac{\left({f_{ib,y}^b}^2 + {f_{ib,z}^b}^2\right)b_{a,x} - f_{ib,x}^b f_{ib,y}^b b_{a,y} - f_{ib,x}^b f_{ib,z}^b b_{a,z}}{\left({f_{ib,x}^b}^2 + {f_{ib,y}^b}^2 + {f_{ib,z}^b}^2\right)\sqrt{{f_{ib,y}^b}^2 + {f_{ib,z}^b}^2}} \end{aligned}. \tag{14.93}$$

From (2.59), the small-angle attitude errors may be expressed in terms of the roll, pitch, and heading errors using

$$\delta\boldsymbol{\psi}^{\gamma}_{\gamma b} = \mathbf{C}^{\gamma}_{b}\mathbf{T}^{\omega}_{\psi}\begin{pmatrix}\delta\phi_{nb}\\ \delta\theta_{nb}\\ \delta\psi_{nb}\end{pmatrix}, \qquad \mathbf{T}^{\omega}_{\psi} = \begin{pmatrix}1 & 0 & -\sin\theta_{nb}\\ 0 & \cos\phi_{nb} & \sin\phi_{nb}\cos\theta_{nb}\\ 0 & -\sin\phi_{nb} & \cos\phi_{nb}\cos\theta_{nb}\end{pmatrix}. \tag{14.94}$$

Therefore, the initial attitude error and accelerometer bias covariance, accounting for the error correlations, is

$$\mathrm{E}\left[\begin{pmatrix}\delta\boldsymbol{\psi}^{\gamma}_{\gamma b}\\ \delta\mathbf{b}_{a}\end{pmatrix}\begin{pmatrix}\delta\boldsymbol{\psi}^{\gamma}_{\gamma b}\\ \delta\mathbf{b}_{a}\end{pmatrix}^{\mathrm{T}}\right] = \begin{pmatrix}\mathbf{C}^{\gamma}_{b}\mathbf{T}^{\omega}_{\psi} & \mathbf{0}_{3}\\ \mathbf{0}_{3} & \mathbf{I}_{3}\end{pmatrix}\mathbf{A}\begin{pmatrix}\sigma^{2}_{ba}\mathbf{I}_{3} & \mathbf{0}_{3\times 1}\\ \mathbf{0}_{1\times 3} & \sigma^{2}_{\delta\psi}\end{pmatrix}\mathbf{A}^{\mathrm{T}}\begin{pmatrix}\mathbf{T}^{\omega\mathrm{T}}_{\psi}\mathbf{C}^{b}_{\gamma} & \mathbf{0}_{3}\\ \mathbf{0}_{3} & \mathbf{I}_{3}\end{pmatrix}$$

$$\mathbf{A} = \begin{pmatrix}0 & \dfrac{f^{b}_{ib,z}}{f^{b}_{ib,y}{}^{2}+f^{b}_{ib,z}{}^{2}} & \dfrac{-f^{b}_{ib,y}}{f^{b}_{ib,y}{}^{2}+f^{b}_{ib,z}{}^{2}} & 0\\ \dfrac{f_{yz}}{f^{2}_{xyz}} & \dfrac{-f^{b}_{ib,x}f^{b}_{ib,y}}{f^{2}_{xyz}f_{yz}} & \dfrac{-f^{b}_{ib,x}f^{b}_{ib,z}}{f^{2}_{xyz}f_{yz}} & 0\\ 0 & 0 & 0 & 1\\ 1 & 0 & 0 & 0\\ 0 & 1 & 0 & 0\\ 0 & 0 & 1 & 0\end{pmatrix}, \qquad \begin{aligned} f_{yz} &= \sqrt{f^{b}_{ib,y}{}^{2}+f^{b}_{ib,z}{}^{2}}\\ f^{2}_{xyz} &= f^{b}_{ib,x}{}^{2}+f^{b}_{ib,y}{}^{2}+f^{b}_{ib,z}{}^{2}\end{aligned} \tag{14.95}$$

where $\sigma_{\delta\psi}$ is the initial heading uncertainty and σ_{ba} is the standard deviation of each accelerometer bias.

When the INS is initialized using transfer alignment (Section 15.1) or quasi-stationary alignment (Section 15.2), the final error covariance matrix from the alignment algorithm should be used to initialize the relevant components of the INS/GNSS integration error covariance matrix. This should be increased to account for the error covariance of the alignment reference. When open-loop INS correction is implemented, the state estimates must also be transferred across.

14.3 Measurement Models

The measurement model of a Kalman filter is described in Section 3.2.4. In INS/GNSS integration, the differences between measurements output by the GNSS user equipment and predictions of those measurements from the inertial navigation solution are used to update the state vector. Which measurements are used depends on the integration architecture, so the loosely coupled measurement model is described first, followed by the tightly coupled model and models for deeply coupled integration.

The section concludes with a discussion of how the attitude and instrument errors are estimated. A number of alternative formulations of the loosely coupled and tightly coupled measurement models may be found in Appendix I on the CD. The MATLAB functions on the CD, Loosely_coupled_INS_GNSS and Tightly_coupled_INS_GNSS, simulate loosely coupled and tightly coupled integration, respectively.

Consider a measurement, $\tilde{m}_G$, output by the GNSS user equipment and a prediction of that measurement, $\tilde{m}_I$, obtained from the raw inertial navigation solution (and the GNSS navigation data message, where appropriate). Estimates of the errors in these measurements, $\delta\hat{m}_G$ and $\delta\hat{m}_I$, can then be obtained from the Kalman filter state vector. There are then two ways in which these can legitimately be assembled into a Kalman filter measurement, z_G, and estimate thereof, $\hat{z}_G^-$. These are

$$z_G = \tilde{m}_G - \tilde{m}_I, \qquad \hat{z}_G^- = \delta\hat{m}_G - \delta\hat{m}_I \tag{14.96}$$

and

$$z_G = \tilde{m}_G, \qquad \hat{z}_G^- = \tilde{m}_I - \delta\hat{m}_I + \delta\hat{m}_G. \tag{14.97}$$

When closed-loop correction of the INS is implemented, the predicted measurement is obtained from the corrected inertial navigation solution and becomes $\hat{m}_I$. It may also be convenient to do this in an open-loop architecture, noting that $\hat{m}_I = \tilde{m}_I - \delta\hat{m}_I$. The options for the measurement and its estimate are then

$$z_G = \tilde{m}_G - \hat{m}_I, \qquad \hat{z}_G^- = \delta\hat{m}_G. \tag{14.98}$$

and

$$z_G = \tilde{m}_G, \qquad \hat{z}_G^- = \hat{m}_I + \delta\hat{m}_G. \tag{14.99}$$

For tightly coupled integration, an extended Kalman filter (Section 3.4.1) is needed for (14.97) and (14.99), but not generally for (14.96) and (14.98). However, the measurement innovation, δz_G^-, is the same in all cases:

$$\begin{aligned} \delta z_G^- &= \tilde{m}_G - \delta\hat{m}_G - \tilde{m}_I + \delta\hat{m}_I \\ &= \tilde{m}_G - \delta\hat{m}_G - \hat{m}_I \end{aligned} \tag{14.100}$$

and may be computed directly. Therefore the distinction between a standard Kalman filter and an EKF is one of semantics rather than implementation. Here, the convention of expressing the measurement innovation directly is adopted. Note that the subscript G is used to distinguish GNSS measurement innovations from other types in multisensor integration (Chapter 16).

The INS-derived and GNSS-derived measurement data must have the same time of validity. Otherwise, contributions to the measurement innovations caused by time synchronization errors will corrupt the state estimates. This may be achieved by storing the inertial navigation solution and retrieving the version at the GNSS

time of validity as described in Section 3.3.4. However, this requires the IMU and GNSS measurements to be synchronized to the same time base. The INS–GNSS timing offset may be determined by comparing the INS and GNSS velocity and/or position solutions during host vehicle maneuvers. When the offset is fixed, a manual comparison of graphs can be very effective. Fixed offsets will typically occur where the INS or IMU timing is synchronized to the GNSS user equipment. For variable offsets, iterative least squares may be used to estimate position, velocity and time offsets from a short sequence of data prior to initialization of the integration algorithm. The time offset may also be estimated as a Kalman filter state as described in Section I.6 of Appendix I on the CD.

Before inputting GNSS measurements to the integration algorithm, they should be tested for faults as described in Chapter 17. For high-integrity applications, measurements may be delayed to enable testing over multiple epochs before acceptance. However, this is at the expense of accuracy as inertial error growth between the time of validity of the measurements and the time when they are processed is only partially corrected. The processing of delayed measurements in a Kalman filter is described in Section 3.3.4.

14.3.1 Loosely Coupled Integration

Loosely coupled INS/GNSS integration uses the GNSS user equipment's position and velocity solution. Therefore, the measurement innovation vector comprises the difference between the GNSS and corrected inertial position and velocity solutions, accounting for the lever arm from the INS to the GNSS antenna, $\mathbf{l}_{ba}^{b}$, which is assumed here to be well known. The coordinate frames for the measurement innovation should match those for the state vector. Thus,

$$\delta\mathbf{z}_{G,k}^{i-} = \begin{pmatrix} \hat{\mathbf{r}}_{iaG}^{i} - \hat{\mathbf{r}}_{ib}^{i} - \hat{\mathbf{C}}_{b}^{i}\mathbf{l}_{ba}^{b} \\ \hat{\mathbf{v}}_{iaG}^{i} - \hat{\mathbf{v}}_{ib}^{i} - \hat{\mathbf{C}}_{b}^{i}\left(\hat{\boldsymbol{\omega}}_{ib}^{b} \times \mathbf{l}_{ba}^{b}\right) \end{pmatrix}_{k}^{-}, \tag{14.101}$$

$$\delta\mathbf{z}_{G,k}^{e-} = \begin{pmatrix} \hat{\mathbf{r}}_{eaG}^{e} - \hat{\mathbf{r}}_{eb}^{e} - \hat{\mathbf{C}}_{b}^{e}\mathbf{l}_{ba}^{b} \\ \hat{\mathbf{v}}_{eaG}^{e} - \hat{\mathbf{v}}_{eb}^{e} - \hat{\mathbf{C}}_{b}^{e}\left(\hat{\boldsymbol{\omega}}_{ib}^{b} \times \mathbf{l}_{ba}^{b}\right) + \boldsymbol{\Omega}_{ie}^{e}\hat{\mathbf{C}}_{b}^{e}\mathbf{l}_{ba}^{b} \end{pmatrix}_{k}^{-} \tag{14.102}$$

and

$$\delta\mathbf{z}_{G,k}^{n-} = \begin{pmatrix} \hat{\mathbf{p}}_{aG} - \hat{\mathbf{p}}_{b} - \hat{\mathbf{T}}_{r(n)}^{p}\hat{\mathbf{C}}_{b}^{n}\mathbf{l}_{ba}^{b} \\ \hat{\mathbf{v}}_{eaG}^{n} - \hat{\mathbf{v}}_{eb}^{n} - \hat{\mathbf{C}}_{b}^{n}\left(\hat{\boldsymbol{\omega}}_{ib}^{b} \times \mathbf{l}_{ba}^{b}\right) + \hat{\boldsymbol{\Omega}}_{ie}^{n}\hat{\mathbf{C}}_{b}^{n}\mathbf{l}_{ba}^{b} \end{pmatrix}_{k}^{-}, \tag{14.103}$$

where the subscript k denotes the measurement update iteration, superscripts i, e, and n respectively denote ECI-frame, ECEF-frame, and local-navigation-frame implementations, the subscript G denotes GNSS indicated; $\boldsymbol{\Omega}_{ie}^{e}$ and $\boldsymbol{\Omega}_{ie}^{n}$ are given by

(5.25) and (5.41), respectively; and from (2.119), the Cartesian-to-curvilinear position change transformation matrix, $\hat{\mathbf{T}}^p_{r(n)}$, is

$$\hat{\mathbf{T}}^p_{r(n)} = \begin{pmatrix} \dfrac{1}{R_N(\hat{L}_b) + \hat{h}_b} & 0 & 0 \\ 0 & \dfrac{1}{\left(R_E(\hat{L}_b) + \hat{h}_b\right)\cos\hat{L}_b} & 0 \\ 0 & 0 & -1 \end{pmatrix}. \tag{14.104}$$

From (5.109) and (5.111),

$$\tilde{\mathbf{C}}^\gamma_b \approx \left(\mathbf{I}_3 + \left[\delta\boldsymbol{\psi}^\gamma_{\gamma b} \wedge\right]\right)\mathbf{C}^\gamma_b. \tag{14.105}$$

Substituting the attitude error states with their residual, $\delta\delta\boldsymbol{\psi}^\gamma_{\gamma b}$ [see (3.4)],

$$\hat{\mathbf{C}}^\gamma_b \approx \left(\mathbf{I}_3 + \left[\delta\delta\boldsymbol{\psi}^\gamma_{\gamma b} \wedge\right]\right)\mathbf{C}^\gamma_b. \tag{14.106}$$

Therefore,

$$\hat{\mathbf{C}}^\gamma_b\mathbf{l}^b_{ba} \approx \mathbf{C}^\gamma_b\mathbf{l}^b_{ba} - \left[\left(\mathbf{C}^\gamma_b\mathbf{l}^b_{ba}\right) \wedge\right]\delta\delta\boldsymbol{\psi}^\gamma_{\gamma b} \tag{14.107}$$

and

$$\begin{aligned} \hat{\mathbf{C}}^\gamma_b\left(\hat{\boldsymbol{\omega}}^b_{ib} \wedge \mathbf{l}^b_{ba}\right) &\approx \mathbf{C}^\gamma_b\left(\hat{\boldsymbol{\omega}}^b_{ib} \wedge \mathbf{l}^b_{ba}\right) - \left[\left\{\mathbf{C}^\gamma_b\left(\hat{\boldsymbol{\omega}}^b_{ib} \wedge \mathbf{l}^b_{ba}\right)\right\} \wedge\right]\delta\delta\boldsymbol{\psi}^\gamma_{\gamma b} \\ &\approx \mathbf{C}^\gamma_b\left(\boldsymbol{\omega}^b_{ib} \wedge \mathbf{l}^b_{ba}\right) - \left[\left\{\mathbf{C}^\gamma_b\left(\hat{\boldsymbol{\omega}}^b_{ib} \wedge \mathbf{l}^b_{ba}\right)\right\} \wedge\right]\delta\delta\boldsymbol{\psi}^\gamma_{\gamma b} - \mathbf{C}^\gamma_b\left(\mathbf{l}^b_{ba} \wedge \delta\mathbf{b}_g\right)^{\cdot} \end{aligned} \tag{14.108}$$

The measurement matrix is given by (3.90):

$$\mathbf{H}_k = \left.\frac{\partial\mathbf{h}(\mathbf{x}, t_k)}{\partial\mathbf{x}}\right|_{\mathbf{x}=\hat{\mathbf{x}}^-_k} = \left.\frac{\partial\mathbf{z}(\mathbf{x}, t_k)}{\partial\mathbf{x}}\right|_{\mathbf{x}=\hat{\mathbf{x}}^-_k}.$$

Taking the measurement vector (14.101) and the state vector (14.15), noting that no GNSS states are estimated in loosely coupled integration, and making use of (14.107) and (14.108), the measurement matrix for ECI-frame loosely coupled INS/GNSS integration is

$$\mathbf{H}^i_{G,k} = \begin{pmatrix} \mathbf{H}^i_{r1} & \mathbf{0}_3 & -\mathbf{I}_3 & \mathbf{0}_3 & \mathbf{0}_3 \\ \mathbf{H}^i_{v1} & -\mathbf{I}_3 & \mathbf{0}_3 & \mathbf{0}_3 & \mathbf{H}^i_{v5} \end{pmatrix}_k, \tag{14.109}$$

where

$$\begin{aligned}\mathbf{H}_{r1}^{i} &\approx \left[\left(\hat{\mathbf{C}}_{b}^{i}\mathbf{l}_{ba}^{b}\right)\wedge\right]\\ \mathbf{H}_{v1}^{i} &\approx \left[\left\{\hat{\mathbf{C}}_{b}^{i}\left(\hat{\boldsymbol{\omega}}_{ib}^{b}\wedge\mathbf{l}_{ba}^{b}\right)\right\}\wedge\right],\\ \mathbf{H}_{v5}^{i} &\approx \hat{\mathbf{C}}_{b}^{i}\left[\mathbf{l}_{ba}^{b}\wedge\right]\end{aligned} \tag{14.110}$$

noting that the corrected INS-indicated attitude, $\hat{\mathbf{C}}_{b}^{i}$, is the best available estimate of the true attitude, $\mathbf{C}_{b}^{i}$.

Similarly, from (14.102), (14.39), (14.107), and (14.108), the ECEF-frame loosely coupled measurement matrix is

$$\mathbf{H}_{G,k}^{e} = \begin{pmatrix} \mathbf{H}_{r1}^{e} & \mathbf{0}_{3} & -\mathbf{I}_{3} & \mathbf{0}_{3} & \mathbf{0}_{3} \\ \mathbf{H}_{v1}^{e} & -\mathbf{I}_{3} & \mathbf{0}_{3} & \mathbf{0}_{3} & \mathbf{H}_{v5}^{e} \end{pmatrix}_{k}, \tag{14.111}$$

where

$$\begin{aligned}\mathbf{H}_{r1}^{e} &\approx \left[\left(\hat{\mathbf{C}}_{b}^{e}\mathbf{l}_{ba}^{b}\right)\wedge\right]\\ \mathbf{H}_{v1}^{e} &\approx \left[\left\{\hat{\mathbf{C}}_{b}^{e}\left(\hat{\boldsymbol{\omega}}_{ib}^{b}\wedge\mathbf{l}_{ba}^{b}\right)-\boldsymbol{\Omega}_{ie}^{e}\hat{\mathbf{C}}_{b}^{e}\mathbf{l}_{ba}^{b}\right\}\wedge\right].\\ \mathbf{H}_{v5}^{e} &\approx \hat{\mathbf{C}}_{b}^{e}\left[\mathbf{l}_{ba}^{b}\wedge\right]\end{aligned} \tag{14.112}$$

From (14.103), (14.51), (14.107), and (14.108), the loosely coupled measurement matrix for an Earth-referenced local-navigation-frame implementation is

$$\mathbf{H}_{G,k}^{n} = \begin{pmatrix} \mathbf{H}_{r1}^{n} & \mathbf{0}_{3} & -\mathbf{I}_{3} & \mathbf{0}_{3} & \mathbf{0}_{3} \\ \mathbf{H}_{v1}^{n} & -\mathbf{I}_{3} & \mathbf{0}_{3} & \mathbf{0}_{3} & \mathbf{H}_{v5}^{n} \end{pmatrix}_{k}, \tag{14.113}$$

where

$$\begin{aligned}\mathbf{H}_{r1}^{n} &\approx \hat{\mathbf{T}}_{r(n)}^{p}\left[\left(\hat{\mathbf{C}}_{b}^{n}\mathbf{l}_{ba}^{b}\right)\wedge\right]\\ \mathbf{H}_{v1}^{n} &\approx \left[\left\{\hat{\mathbf{C}}_{b}^{n}\left(\hat{\boldsymbol{\omega}}_{ib}^{b}\wedge\mathbf{l}_{ba}^{b}\right)-\hat{\boldsymbol{\Omega}}_{ie}^{n}\hat{\mathbf{C}}_{b}^{n}\mathbf{l}_{ba}^{b}\right\}\wedge\right].\\ \mathbf{H}_{v5}^{n} &\approx \hat{\mathbf{C}}_{b}^{n}\left[\mathbf{l}_{ba}^{b}\wedge\right]\end{aligned} \tag{14.114}$$

Except where the lever arm is very large, the Earth-rotation terms in (14.102), (14.103), (14.112), and (14.114) may be neglected.

In practice, the coupling of the attitude errors and gyro biases into the measurements through the lever arm terms is also weak. These states are mainly estimated

through the change in the velocity error as described in Section 14.3.4. Therefore, the measurement matrices can often be approximated to

$$\mathbf{H}_{G,k}^{i/e/n} \approx \begin{pmatrix} \mathbf{0}_3 & \mathbf{0}_3 & -\mathbf{I}_3 & \mathbf{0}_3 & \mathbf{0}_3 \\ \mathbf{0}_3 & -\mathbf{I}_3 & \mathbf{0}_3 & \mathbf{0}_3 & \mathbf{0}_3 \end{pmatrix}_k, \tag{14.115}$$

noting that the remaining lever arm terms in the measurement innovations, (14.101) to (14.103), must not be neglected. This approximate version of the ECEF-frame measurement model is included in the MATLAB function, LC_KF_Epoch, on the CD.

Measurement noise arises due to a combination of factors such as RF and thermal noise, dynamics response lag, multipath interference, and NLOS signal reception. This may then be smoothed within the GNSS navigation processor by an EKF or carrier-smoothing algorithm, reducing the magnitude of the noise, but increasing its correlation time. Ideally, the measurement noise covariance matrix, $\mathbf{R}_G$, should be based on the error covariance of the GNSS navigation solution (e.g., $\mathbf{P}$ for an EKF), enabling the GNSS data to be weighted according to the GNSS user equipment's own level of confidence. However, this information is rarely output in practice. The measurement noise covariance is often assumed to be constant, but is better modeled as a function of the measured carrier power to noise density, $\tilde{c}/\tilde{n}_0$, satellite signal geometry, and acceleration. Acceleration is relevant because the effects of INS-GNSS time synchronization errors are larger under high dynamics. The measurement noise covariance must also account for any flexure in the lever arm between the INS and the GNSS antenna, which can also be excited by dynamics.

When the measurement-update interval is shorter than the correlation time of the noise on the GNSS position and velocity solution, the measurement noise covariance assumed in the integration Kalman filter should be increased to downweight the measurements. Note that reducing the measurement-update interval can better capture the host-vehicle dynamics, improving the observability of some of the attitude and instrument error states.

A suitable value for a component of the measurement noise covariance is thus the variance of the position or velocity error multiplied by the ratio of the error correlation time to the measurement update interval. Typical values for a 1-Hz update interval are $(2\text{–}20\text{m})^2$ for position and $(0.1\text{–}1\text{ m s}^{-1})^2$ for velocity, with the larger values used where GNSS reception is relatively poor, such as in urban areas.

In local-navigation-frame implementations of the loosely coupled measurement model, mixing latitude and longitude in radians with height in meters can cause numerical problems in the $\left(\mathbf{H}_k\mathbf{P}_k^-\mathbf{H}_k^{\mathrm{T}} + \mathbf{R}_k\right)$ matrix inversion step of the measurement update. One solution is to rescale the latitude and longitude components, in which case, the measurement innovation, $\delta\mathbf{z}_{G,k}^{n-}$, and measurement matrix, $\mathbf{H}_{G,k}^{n}$, become

$$\delta\mathbf{z}_{G,k}^{n-} = \begin{pmatrix} \mathbf{S}_p\left(\hat{\mathbf{p}}_{aG} - \hat{\mathbf{p}}_b - \hat{\mathbf{T}}_{r(n)}^{p}\hat{\mathbf{C}}_b^n\mathbf{l}_{ba}^b\right) \\ \hat{\mathbf{v}}_{eaG}^n - \hat{\mathbf{v}}_{eb}^n - \hat{\mathbf{C}}_b^n\left(\hat{\boldsymbol{\omega}}_{ib}^b \times \mathbf{l}_{ba}^b\right) + \hat{\boldsymbol{\Omega}}_{ie}^n\hat{\mathbf{C}}_b^n\mathbf{l}_{ba}^b \end{pmatrix}_k, \tag{14.116}$$

$$\begin{aligned}\mathbf{H}^n_{G,k} &= \begin{pmatrix} \mathbf{S}_p\mathbf{H}^n_{r1} & \mathbf{0}_3 & -\mathbf{S}_p & \mathbf{0}_3 & \mathbf{0}_3 \\ \mathbf{H}^n_{v1} & -\mathbf{I}_3 & \mathbf{0}_3 & \mathbf{0}_3 & \mathbf{H}^n_{v5} \end{pmatrix}_k, \\ &\approx \begin{pmatrix} \mathbf{0}_3 & \mathbf{0}_3 & -\mathbf{S}_p & \mathbf{0}_3 & \mathbf{0}_3 \\ \mathbf{0}_3 & -\mathbf{I}_3 & \mathbf{0}_3 & \mathbf{0}_3 & \mathbf{0}_3 \end{pmatrix}_k \end{aligned} \tag{14.117}$$

where $\mathbf{S}_p$ is the curvilinear position scaling matrix, given by

$$\mathbf{S}_p = \begin{pmatrix} s_{L\lambda} & 0 & 0 \\ 0 & s_{L\lambda} & 0 \\ 0 & 0 & 1 \end{pmatrix}, \tag{14.118}$$

where a suitable value for $s_{L\lambda}$ is 10^3, which converts the latitude and longitude components of the measurement innovation from radians to milliradians.

14.3.2 Tightly Coupled Integration

Tightly coupled INS/GNSS integration uses the GNSS ranging processor's pseudo-range and pseudo-range-rate measurements, obtained from code and carrier tracking, respectively. The measurement model is thus based on that of the GNSS navigation filter, described in Section 9.4.2.3. The measurement innovation vector comprises the differences between the GNSS measured pseudo-range and pseudo-range rates and values predicted from the corrected inertial navigation solution at the same time of validity, estimated receiver clock offset and drift, and navigation-data-indicated satellite positions and velocities. Thus,

$$\delta\mathbf{z}^-_{G,k} = \begin{pmatrix} \delta\mathbf{z}^-_{\rho,k} \\ \delta\mathbf{z}^-_{r,k} \end{pmatrix}, \qquad \begin{aligned} \delta\mathbf{z}^-_{\rho,k} &= \left(\tilde{\rho}^1_{a,C} - \hat{\rho}^{1-}_{a,C}, \tilde{\rho}^2_{a,C} - \hat{\rho}^{2-}_{a,C}, \cdots \tilde{\rho}^m_{a,C} - \hat{\rho}^{m-}_{a,C}\right)_k \\ \delta\mathbf{z}^-_{r,k} &= \left(\tilde{\tilde{\rho}}^1_{a,C} - \hat{\tilde{\rho}}^{1-}_{a,C}, \tilde{\tilde{\rho}}^2_{a,C} - \hat{\tilde{\rho}}^{2-}_{a,C}, \cdots \tilde{\tilde{\rho}}^m_{a,C} - \hat{\tilde{\rho}}^{m-}_{a,C}\right)_k \end{aligned}. \tag{14.119}$$

For the jth measurement, comprising signal l from satellite s, the corrected pseudo-range and pseudo-range-rate measurements, $\tilde{\rho}^j_{a,C} \equiv \tilde{\rho}^{s,l}_{a,C}$ and $\tilde{\tilde{\rho}}^j_{a,C} \equiv \tilde{\tilde{\rho}}^{s,l}_{a,C}$, are given by [repeating (8.49)]

$$\begin{aligned} \tilde{\rho}^{s,l}_{a,C} &= \tilde{\rho}^{s,l}_{a,R} - \delta\hat{\rho}^{s,l}_{I,a} - \delta\hat{\rho}^{s}_{T,a} + \delta\hat{\rho}^{s,l}_{c} \\ \tilde{\tilde{\rho}}^{s,l}_{a,C} &= \tilde{\tilde{\rho}}^{s,l}_{a,R} + \delta\hat{\rho}^{s}_{c} \end{aligned}.$$

Their estimated counterparts are given by [repeating (9.161)]

$$\begin{aligned} \hat{\rho}^{j-}_{a,C,k} &= \sqrt{\left[\hat{\mathbf{r}}^i_{ij}\left(\tilde{t}^j_{st,a,k}\right) - \hat{\mathbf{r}}^{i-}_{ia,k}\right]^{\mathrm{T}}\left[\hat{\mathbf{r}}^i_{ij}\left(\tilde{t}^j_{st,a,k}\right) - \hat{\mathbf{r}}^{i-}_{ia,k}\right]} + \delta\hat{\rho}^{a-}_{c,k} \\ \hat{\tilde{\rho}}^{j-}_{a,C,k} &= \hat{\mathbf{u}}^{i-\,\mathrm{T}}_{aj,k}\left[\hat{\mathbf{v}}^i_{ij}\left(\tilde{t}^j_{st,a,k}\right) - \hat{\mathbf{v}}^{i-}_{ia,k}\right] + \delta\hat{\tilde{\rho}}^{a-}_{c,k} \end{aligned}$$

for an ECI-frame calculation and [repeating (9.164)]

$$\hat{\rho}^{j-}_{a,C,k} = \sqrt{\left[\hat{\mathbf{r}}^{e}_{ej}\left(\tilde{t}^{j}_{st,a,k}\right) - \hat{\mathbf{r}}^{e-}_{ea,k}\right]^{\mathrm{T}}\left[\hat{\mathbf{r}}^{e}_{ej}\left(\tilde{t}^{j}_{st,a,k}\right) - \hat{\mathbf{r}}^{e-}_{ea,k}\right]} + \delta\hat{\rho}^{a-}_{c,k} + \delta\rho^{j}_{ie}$$
$$\hat{\rho}^{j-}_{a,C,k} = \hat{\mathbf{u}}^{e-}_{aj,k}{}^{\mathrm{T}}\left[\hat{\mathbf{v}}^{e}_{ej}\left(\tilde{t}^{j}_{st,a,k}\right) - \hat{\mathbf{v}}^{e-}_{ea,k}\right] + \delta\hat{\dot{\rho}}^{a-}_{c,k} + \delta\dot{\rho}^{j}_{ie}$$

or [repeating (9.165)]

$$\hat{\rho}^{j-}_{a,C,k} = \sqrt{\left[\mathbf{C}^{I}_{e}\left(\tilde{t}^{j}_{st,a,k}\right)\hat{\mathbf{r}}^{e}_{ej}\left(\tilde{t}^{j}_{st,a,k}\right) - \hat{\mathbf{r}}^{e-}_{ea,k}\right]^{\mathrm{T}}\left[\mathbf{C}^{I}_{e}\left(\tilde{t}^{j}_{st,a,k}\right)\hat{\mathbf{r}}^{e}_{ej}\left(\tilde{t}^{j}_{st,a,k}\right) - \hat{\mathbf{r}}^{e-}_{ea,k}\right]} + \delta\hat{\rho}^{a-}_{c,k}$$
$$\hat{\dot{\rho}}^{j-}_{a,C,k} = \hat{\mathbf{u}}^{e-}_{as,j}{}^{\mathrm{T}}\left[\mathbf{C}^{I}_{e}\left(\tilde{t}^{j}_{st,a,k}\right)\left(\hat{\mathbf{v}}^{e}_{ej}\left(\tilde{t}^{j}_{st,a,k}\right) + \boldsymbol{\Omega}^{e}_{ie}\hat{\mathbf{r}}^{e}_{ej}\left(\tilde{t}^{j}_{st,a,k}\right)\right) - \left(\hat{\mathbf{v}}^{e-}_{ea,k} + \boldsymbol{\Omega}^{e}_{ie}\hat{\mathbf{r}}^{e-}_{ea,k}\right)\right] + \delta\hat{\dot{\rho}}^{a-}_{c,k}$$

for an ECEF-frame calculation, where the transmission time used to calculate $\hat{\mathbf{r}}^{e}_{ej}$ is given by [repeating (9.125)]

$$\tilde{t}^{s,l}_{st,a} = \tilde{t}^{s,l}_{sa,a} - \left(\tilde{\rho}^{s,l}_{a,\mathrm{R}} + \delta\hat{\rho}^{s,l}_{c}\right)/c\,.$$

However, $\mathbf{C}^{I}_{e}$ is calculated using (8.36) as a function of the range between the user antenna and satellite, not the pseudo-range, because the *I* frame is synchronized with the ECEF frame at the true time of signal arrival, not the measured time.

The position and velocity of the user antenna are obtained from the inertial navigation solution using

$$\begin{aligned}\hat{\mathbf{r}}^{i}_{ia} &= \hat{\mathbf{r}}^{i}_{ib} + \hat{\mathbf{C}}^{i}_{b}\mathbf{l}^{b}_{ba}\\ \hat{\mathbf{v}}^{i}_{ia} &= \hat{\mathbf{v}}^{i}_{ib} + \hat{\mathbf{C}}^{i}_{b}\left(\hat{\boldsymbol{\omega}}^{b}_{ib} \wedge \mathbf{l}^{b}_{ba}\right)\end{aligned}\,, \tag{14.120}$$

$$\begin{aligned}\hat{\mathbf{r}}^{e}_{ea} &= \hat{\mathbf{r}}^{e}_{eb} + \hat{\mathbf{C}}^{e}_{b}\mathbf{l}^{b}_{ba}\\ \hat{\mathbf{v}}^{e}_{ea} &= \hat{\mathbf{v}}^{e}_{eb} + \hat{\mathbf{C}}^{e}_{b}\left(\hat{\boldsymbol{\omega}}^{b}_{ib} \wedge \mathbf{l}^{b}_{ba}\right) + \boldsymbol{\Omega}^{e}_{ie}\hat{\mathbf{C}}^{e}_{b}\mathbf{l}^{b}_{ba}\end{aligned} \tag{14.121}$$

or

$$\hat{\mathbf{r}}^{e}_{ea} = \begin{pmatrix}\left(R_E(\hat{L}_b) + \hat{h}_b\right)\cos\hat{L}_b\cos\hat{\lambda}_b\\ \left(R_E(\hat{L}_b) + \hat{h}_b\right)\cos\hat{L}_b\sin\hat{\lambda}_b\\ \left[\left(1 - e^2\right)R_E(\hat{L}_b) + \hat{h}_b\right]\sin\hat{L}_b\end{pmatrix} + \hat{\mathbf{C}}^{e}_{n}\hat{\mathbf{C}}^{n}_{b}\mathbf{l}^{b}_{ba}\,, \tag{14.122}$$
$$\hat{\mathbf{v}}^{e}_{ea} = \hat{\mathbf{C}}^{e}_{n}\hat{\mathbf{v}}^{n}_{eb} + \hat{\mathbf{C}}^{e}_{n}\hat{\mathbf{C}}^{n}_{b}\left(\hat{\boldsymbol{\omega}}^{b}_{ib} \wedge \mathbf{l}^{b}_{ba}\right) + \boldsymbol{\Omega}^{e}_{ie}\hat{\mathbf{C}}^{e}_{n}\hat{\mathbf{C}}^{n}_{b}\mathbf{l}^{b}_{ba}$$

where $\boldsymbol{\Omega}^{e}_{ie}$ and $\hat{\mathbf{C}}^{e}_{n}$ are given by (5.25) and (2.150), respectively, and the Earth-rotation terms may be neglected except where the lever arm is very large.

For tightly coupled integration, the state vector typically comprises the inertial states, receiver clock offset, and clock drift. Thus,

$$\mathbf{x}^{\gamma} = \begin{pmatrix} \mathbf{x}^{\gamma}_{INS} \\ \delta\rho^{a}_{c} \\ \delta\dot{\rho}^{a}_{c} \end{pmatrix}, \tag{14.123}$$

where the inertial state vectors given by (14.15), (14.39), and (14.51) are assumed.

The measurement matrix is given by (3.90) and can be expressed in terms of submatrices as

$$\mathbf{H}^{\gamma}_{G,k} = \begin{pmatrix} \frac{\partial \mathbf{z}_{\rho}}{\partial \boldsymbol{\delta\psi}^{\gamma}_{\gamma b}} & \mathbf{0}_{m,3} & \frac{\partial \mathbf{z}_{\rho}}{\partial \delta \mathbf{r}^{\gamma}_{\gamma b}} & \mathbf{0}_{m,3} & \mathbf{0}_{m,3} & \frac{\partial \mathbf{z}_{\rho}}{\partial \delta\rho^{a}_{c}} & \mathbf{0}_{m,1} \\ \frac{\partial \mathbf{z}_{r}}{\partial \boldsymbol{\delta\psi}^{\gamma}_{\gamma b}} & \frac{\partial \mathbf{z}_{r}}{\partial \delta \mathbf{v}^{\gamma}_{\gamma b}} & \frac{\partial \mathbf{z}_{r}}{\partial \delta \mathbf{r}^{\gamma}_{\gamma b}} & \mathbf{0}_{m,3} & \frac{\partial \mathbf{z}_{\rho}}{\partial \mathbf{b}_{g}} & \mathbf{0}_{m,1} & \frac{\partial \mathbf{z}_{r}}{\partial \delta\dot{\rho}^{a}_{c}} \end{pmatrix}_{\mathbf{x}=\hat{\mathbf{x}}^{-}_{k}} \quad \gamma \in i,e \tag{14.124}$$

or

$$\mathbf{H}^{n}_{G,k} = \begin{pmatrix} \frac{\partial \mathbf{z}_{\rho}}{\partial \boldsymbol{\delta\psi}^{n}_{nb}} & \mathbf{0}_{m,3} & \frac{\partial \mathbf{z}_{\rho}}{\partial \delta \mathbf{p}_{b}} & \mathbf{0}_{m,3} & \mathbf{0}_{m,3} & \frac{\partial \mathbf{z}_{\rho}}{\partial \delta\rho^{a}_{c}} & \mathbf{0}_{m,1} \\ \frac{\partial \mathbf{z}_{r}}{\partial \boldsymbol{\delta\psi}^{n}_{nb}} & \frac{\partial \mathbf{z}_{r}}{\partial \delta \mathbf{v}^{n}_{eb}} & \frac{\partial \mathbf{z}_{r}}{\partial \delta \mathbf{p}_{b}} & \mathbf{0}_{m,3} & \frac{\partial \mathbf{z}_{\rho}}{\partial \mathbf{b}_{g}} & \mathbf{0}_{m,1} & \frac{\partial \mathbf{z}_{r}}{\partial \delta\dot{\rho}^{a}_{c}} \end{pmatrix}_{\mathbf{x}=\hat{\mathbf{x}}^{-}_{k}}. \tag{14.125}$$

The differentials may be calculated analytically or numerically by perturbing the state estimates and calculating the change in estimate pseudo-range and pseudo-range rate. The dependence of the measurement innovations on the attitude error and of the pseudo-range-rate measurements on the position and gyro errors is weak, so a common approximation to the analytical solution is

$$\mathbf{H}^{\gamma}_{G,k} \approx \left(\begin{array}{ccccccc} \mathbf{0}_{1,3} & \mathbf{0}_{1,3} & \mathbf{u}^{\gamma\,\mathrm{T}}_{a1} & \mathbf{0}_{1,3} & \mathbf{0}_{1,3} & 1 & 0 \\ \mathbf{0}_{1,3} & \mathbf{0}_{1,3} & \mathbf{u}^{\gamma\,\mathrm{T}}_{a2} & \mathbf{0}_{1,3} & \mathbf{0}_{1,3} & 1 & 0 \\ \vdots & \vdots & \vdots & \vdots & \vdots & \vdots & \vdots \\ \mathbf{0}_{1,3} & \mathbf{0}_{1,3} & \mathbf{u}^{\gamma\,\mathrm{T}}_{am} & \mathbf{0}_{1,3} & \mathbf{0}_{1,3} & 1 & 0 \\ \hline \mathbf{0}_{1,3} & \mathbf{u}^{\gamma\,\mathrm{T}}_{a1} & \mathbf{0}_{1,3} & \mathbf{0}_{1,3} & \mathbf{0}_{1,3} & 0 & 1 \\ \mathbf{0}_{1,3} & \mathbf{u}^{\gamma\,\mathrm{T}}_{a2} & \mathbf{0}_{1,3} & \mathbf{0}_{1,3} & \mathbf{0}_{1,3} & 0 & 1 \\ \vdots & \vdots & \vdots & \vdots & \vdots & \vdots & \vdots \\ \mathbf{0}_{1,3} & \mathbf{u}^{\gamma\,\mathrm{T}}_{am} & \mathbf{0}_{1,3} & \mathbf{0}_{1,3} & \mathbf{0}_{1,3} & 0 & 1 \end{array}\right)_{\mathbf{x}=\hat{\mathbf{x}}^{-}_{k}} \quad \gamma \in i,e \tag{14.126}$$

or

$$\mathbf{H}_{G,k}^{n} \approx \left(\begin{array}{ccccccc} \mathbf{0}_{1,3} & \mathbf{0}_{1,3} & \mathbf{h}_{\rho p}^{1\,\mathrm{T}} & \mathbf{0}_{1,3} & \mathbf{0}_{1,3} & 1 & 0 \\ \mathbf{0}_{1,3} & \mathbf{0}_{1,3} & \mathbf{h}_{\rho p}^{2\,\mathrm{T}} & \mathbf{0}_{1,3} & \mathbf{0}_{1,3} & 1 & 0 \\ \vdots & \vdots & \vdots & \vdots & \vdots & \vdots & \vdots \\ \mathbf{0}_{1,3} & \mathbf{0}_{1,3} & \mathbf{h}_{\rho p}^{m\,\mathrm{T}} & \mathbf{0}_{1,3} & \mathbf{0}_{1,3} & 1 & 0 \\ \hline \mathbf{0}_{1,3} & \mathbf{u}_{a1}^{n\,\mathrm{T}} & \mathbf{0}_{1,3} & \mathbf{0}_{1,3} & \mathbf{0}_{1,3} & 0 & 1 \\ \mathbf{0}_{1,3} & \mathbf{u}_{a2}^{n\,\mathrm{T}} & \mathbf{0}_{1,3} & \mathbf{0}_{1,3} & \mathbf{0}_{1,3} & 0 & 1 \\ \vdots & \vdots & \vdots & \vdots & \vdots & \vdots & \vdots \\ \mathbf{0}_{1,3} & \mathbf{u}_{am}^{n\,\mathrm{T}} & \mathbf{0}_{1,3} & \mathbf{0}_{1,3} & \mathbf{0}_{1,3} & 0 & 1 \end{array} \right)_{\mathbf{x}=\hat{\mathbf{x}}_k^-}, \tag{14.127}$$

where

$$\mathbf{h}_{\rho p}^{j} = \begin{pmatrix} \left(R_N(\hat{L}_b) + \hat{h}_b\right) u_{aj,N}^{n} \\ \left(R_E(\hat{L}_b) + \hat{h}_b\right) \cos\hat{L}_b u_{aj,E}^{n} \\ -u_{aj,D}^{n} \end{pmatrix}, \tag{14.128}$$

where the line-of-sight unit vector, $\mathbf{u}_{aj}^{\gamma}$, is as defined in Section 8.5.3. Note that where the position error is large (e.g., when fewer than four GNSS satellites are tracked), the error in resolving the line-of-sight vectors along north, east, and down can be significant. The approximate version of the ECEF-frame measurement model is included in the MATLAB function, TC_KF_Epoch, on the CD.

The measurement noise covariance, $\mathbf{R}_G$, accounts for GNSS tracking errors, multipath variations, satellite clock noise, residual INS-GNSS synchronization errors, and flexure in the lever arm between the IMU and GNSS antenna. It should ideally be modeled as a function of $\tilde{c}/\tilde{n}_0$ and acceleration, though a constant value is often assumed. It may also be scaled to weight the measurements according to the expected range bias standard deviations and account for the effects of time-correlated noise. The matrix $\mathbf{R}_G$ is diagonal unless the pseudo-range measurements are carrier-smoothed. See Section 9.4.2.4 for more information.

An alternative to using pseudo-range rate measurements is to use carrier-smoothed pseudo-ranges (see Section 9.2.7) and estimate the time-correlated tracking errors as additional Kalman filter states. The pseudo-range rates are then inferred from the changes in the carrier-smoothed pseudo-ranges. In terms of processor load, this is typically more efficient when a vector measurement update is used and less efficient with a sequential measurement update. Otherwise, using carrier-smoothed pseudo-ranges does not significantly impact performance.

Another alternative is to use the delta ranges, which are the changes in ADR. The delta-range measurements are less noisy than the pseudo-range rates where the measurement-update interval is much longer than the carrier tracking-loop correlation

time. This applies with a 1-second update interval and carrier phase tracking. However, using delta range adds complexity to the Kalman filter, requiring either the use of delayed position error states or the incorporation of back-propagation through the system model into the measurement model as described in Section 3.3.4 and in Section G.8.3 of Appendix G on the CD [31, 33].

As discussed in Section 14.2.1, pseudo-range and pseudo-range-rate or delta-range measurements may also be differenced between satellites [31], in which case the receiver clock states are omitted. Using the superscript Δ to denote a differenced measurement, the differenced measurement innovation, measurement matrix, and measurement noise covariance matrix are related to their undifferenced counterparts by

$$\begin{aligned}
\delta\mathbf{z}^{\Delta-}_{G,k} &= \begin{pmatrix} \mathbf{D}_G & \mathbf{0} \\ \mathbf{0} & \mathbf{D}_G \end{pmatrix} \delta\mathbf{z}^{-}_{G,k} \\
\mathbf{H}^{\Delta\gamma}_{G,k} &= \begin{pmatrix} \mathbf{D}_G & \mathbf{0} \\ \mathbf{0} & \mathbf{D}_G \end{pmatrix} \mathbf{H}^{\gamma}_{G,k} \qquad \gamma \in i,e,n \ , \\
\mathbf{R}^{\Delta}_{G,k} &= \begin{pmatrix} \mathbf{D}_G & \mathbf{0} \\ \mathbf{0} & \mathbf{D}_G \end{pmatrix} \mathbf{R}_{G,k} \begin{pmatrix} \mathbf{D}_G & \mathbf{0} \\ \mathbf{0} & \mathbf{D}_G \end{pmatrix}^{\mathrm{T}}
\end{aligned} \tag{14.129}$$

where $\mathbf{D}_G$ is the differencing matrix, which is given by (10.18) in cases where a common reference satellite is used. Note that the measurement noise covariance matrix, $\mathbf{R}^{\Delta}_{G,k}$, is not diagonal.

Some GNSS receivers periodically implement 1-ms clock corrections, causing jumps of 3×10^5 m in their pseudo-range measurements. Tightly coupled integration algorithms using these receivers must detect these jumps and correct the clock offset estimate, $\delta\hat{\rho}^a_c$, using the algorithm shown in Figure 9.31.

14.3.3 Deeply Coupled Integration

The measurement model of a deep INS/GNSS integration and tracking algorithm comprises both the measurement model of the integration filter and the prefilters, implemented for each signal or satellite. The integration filter measurement model is described first, followed by descriptions of the noncoherent and coherent prefilters, a discussion on multisignal prefiltering, and finally, a description of receiver NCO control.

14.3.3.1 Integration Filter Measurement Model

The integration filter estimates the INS and receiver clock errors, and optionally, ionosphere or range-bias states. The measurement update rate is typically between 1 and 10 Hz. This must be set high enough to track the receiver clock noise and capture the host-vehicle dynamics.

Pseudo-range and pseudo-range rate measurement innovations are generated by the prefilters and input directly to the integration Kalman filter. Thus, the integration filter measurement model is essentially the same as for tightly coupled integration as described in Section 14.3.2.

Extra columns of the measurement matrix, $\mathbf{H}_{G,k}$, are required where range bias and/or ionosphere propagation delay states are estimated. For the pseudo-range rate measurements, these columns are all zero. For the pseudo-range measurements, the range bias elements are equal to 1 where measurement corresponds to the same satellite as the range bias state and to 0 otherwise. Similarly, the ionosphere elements are equal to $\left(f_{ca}^{L}/f_{ca}^{l}\right)^2$ where the pseudo-range measurement corresponds to the same satellite as the ionosphere state and to 0 otherwise; f_{ca}^{l} is the carrier frequency of the measurement and f_{ca}^{L} is a reference carrier frequency, typically the L1 frequency. Determination of the integration filter measurement noise covariance, $\mathbf{R}_G$, is discussed with the prefilters.

Measurements from a given signal should only be accepted where the tracking of that signal is in lock; otherwise, that signal must be reacquired. As deeply coupled integration can bridge short-term GNSS signal outages, lock detection cannot be c/n_0-based. Code tracking lock is determined by comparing the pseudo-range uncertainties, obtained by resolving the position-error and clock-offset state uncertainties along each user-satellite line of sight, with the code chip length. For determining carrier-frequency tracking lock, the pseudo-range rate uncertainties may be obtained from the velocity-error and clock-drift state uncertainties and compared against the tolerance given by (9.25); this is inversely proportional to the coherent integration, or accumulation, interval, τ_a. When there is insufficient c/n_0 for tracking to be maintained, $\mathbf{R}_G$ will be large, causing the state uncertainties to grow.

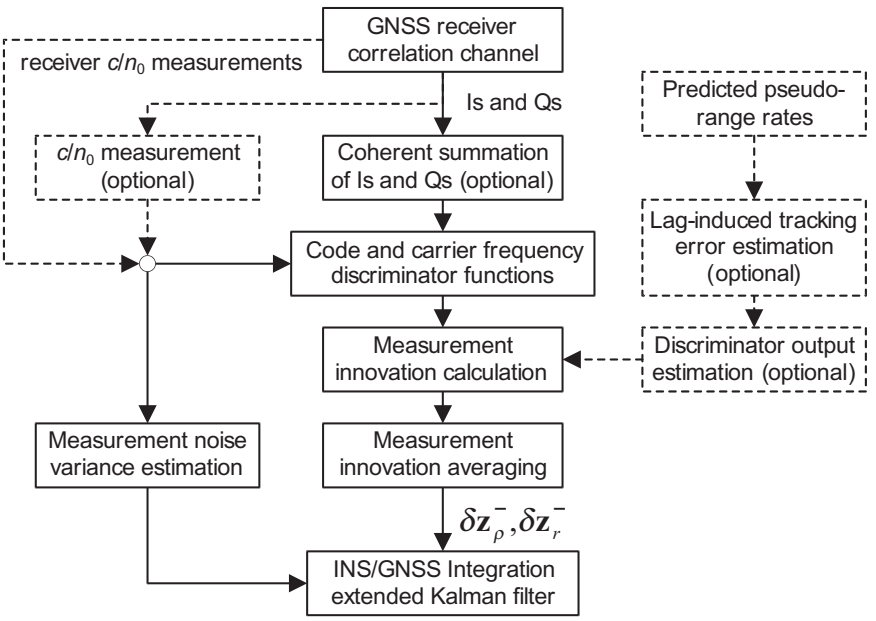

Figure 14.10 Noncoherent prefilter for deeply coupled integration.

14.3.3.2 Noncoherent Prefilters

Figure 14.10 shows the stages of the noncoherent prefilter. Coherent summation of the Is and Qs over the navigation data bit interval may be implemented where the receiver generates Is and Qs at a faster rate and the timing of the data bit transitions is known. Similarly, when navigation-data wipe-off (see Section 10.3.5) or a data-free signal is used, coherent I and Q summation may be performed over longer intervals. As discussed in Section 9.1.4.4, increasing the coherent summation interval improves signal-to-noise performance, but reduces the carrier-frequency tracking tolerance. One option is to vary the coherent summation interval as a function of the uncertainty in the predicted pseudo-range rate.

Following any coherent summation, the Is and Qs are used to form discriminator measurements as in a conventional GNSS ranging processor, described in Sections 9.2.2 and 9.2.3. Pseudo-range and pseudo-range-rate measurement innovations can then be obtained from the discriminator outputs using

$$\begin{aligned} \delta z^{j-}_{\rho,k} &= -\frac{c}{f_{co}}\left(\tilde{x}^j_k - \hat{x}^j_k\right) \\ \delta z^{j-}_{rk} &= -\frac{c}{f_{ca}}\left(\delta\tilde{f}^j_{ca,k} - \delta\hat{f}^j_{ca,k}\right) \end{aligned}, \tag{14.130}$$

where $\tilde{x}^j_k$ is the code discriminator output for channel j at iteration k, $\delta\tilde{f}^j_{ca,k}$ is the corresponding carrier-frequency discriminator output, and $\hat{x}^j_k$ and $\delta\hat{f}^j_{ca,k}$ are their estimated counterparts. It is assumed that the code discriminator outputs are normalized using $\tilde{c}/\tilde{n}_0$. Note that the estimated discriminator outputs are zero where there are no significant lags in applying the NCO commands (e.g., where a software receiver is used or NCO commands are applied at the IMU output rate). What constitutes a significant lag depends on the host-vehicle dynamics.

Unless a long coherent integration interval is used, the measurement innovations given by (14.130) are averaged (noncoherently) over successive iterations to reduce the integration filter processing load. Note that averaging should always be used in preference to undersampling, as it gives a better signal-to-noise level.

The noise variances of the pseudo-range and pseudo-range rate measurements are

$$\mathrm{E}\left(w^j_{m,\rho,k}{}^2\right) = \frac{c^2\sigma^2\left(N_D D\right)}{f^2_{co} n_D} + R^j_{\rho D,k}, \qquad \mathrm{E}\left(w^j_{m,r,k}{}^2\right) = \frac{c^2\sigma^2\left(N_F F\right)}{f^2_{ca} n_D} + R^j_{rD,k}. \tag{14.131}$$

where $\sigma^2(N_D D)$ and $\sigma^2(N_F F)$ are, respectively, the variances of the code and carrier-frequency discriminators, given in Section 9.3.3; n_D is the number of successive discriminator measurements averaged to form the measurement innovations; and $R^j_{\rho D,k}$ and $R^j_{rD,k}$ are empirically-determined terms to account for the effects of uncompensated NCO control lags (see Section 14.3.3.5), which may be proportional to the squares of the line-of-sight acceleration and/or jerk.

In theory, a noncoherent prefilter can also process carrier phase measurements, obtained from conventional carrier-phase discriminators. However, in practice, a coherent prefilter is used.

14.3.3.3 Coherent Prefilters

Figure 14.11 shows the main elements of a coherent prefilter for deep INS/GNSS integration. At its core, is a tracking filter that estimates the code-phase, carrier-phase, and carrier-frequency tracking errors for the relevant signal. This may be an EKF or a nonlinear estimation algorithm [34–36]. To maintain accurate carrier phase estimates, the tracking filter measurement update must be performed at at least 50 Hz. Therefore, coherent summation of the Is and Qs prior to the tracking filter is only performed where the receiver outputs them at a much higher rate. In coherent implementations of deeply coupled integration, pseudo-range and pseudo-range rate or delta-range measurements are typically output to the integration filter at 1 or 2 Hz.

All coherent prefilters estimate the code tracking error, x^j, the carrier phase tracking error, $\delta\phi_{ca}^j$ [given by (9.11)], and the carrier frequency tracking error, δf_{ca}^j. The derivative of the carrier frequency tracking error, $\delta\dot{f}_{ca}^j$, and the signal amplitude or carrier power to noise density may also be estimated [34, 35].

When the derivative of the carrier frequency tracking error is estimated, the deterministic system model for this state and the carrier frequency tracking error is

$$\frac{\partial}{\partial t}\delta f_{ca}^j = \delta\dot{f}_{ca}^j, \qquad \mathrm{E}\left(\frac{\partial}{\partial t}\delta\dot{f}_{ca}^j\right) = 0. \tag{14.132}$$

Otherwise, the deterministic system model is

$$\mathrm{E}\left(\frac{\partial}{\partial t}\delta f_{ca}^j\right) = 0. \tag{14.133}$$

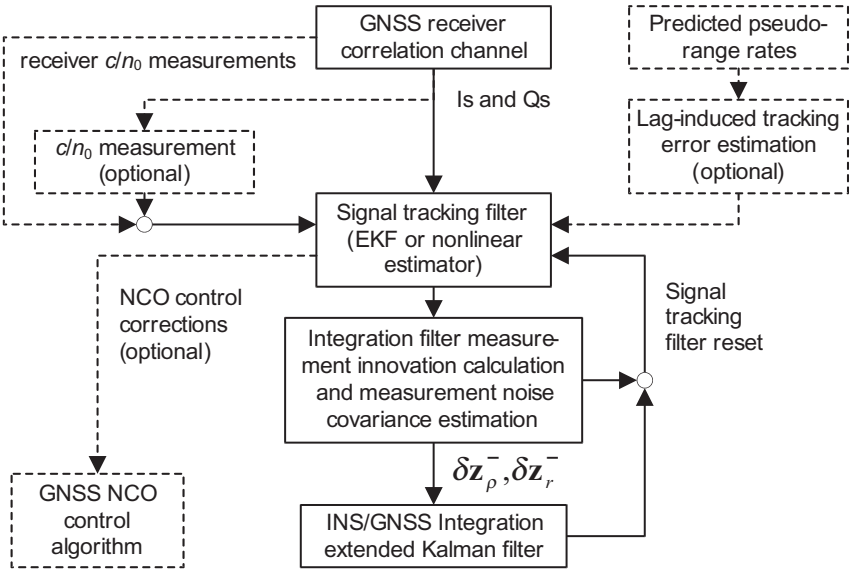

Figure 14.11 Coherent prefilter for deeply coupled integration.

When the prefilter frequency tracking error estimate is not used to modify the NCO commands, the deterministic system model for the code and carrier-phase tracking errors is

$$\delta\dot{x}^j = \frac{f_{co}}{f_{ca}}\delta f_{ca}^j, \qquad \delta\dot{\phi}_{ca}^j = 2\pi\delta f_{ca}^j. \tag{14.134}$$

Otherwise, the deterministic system model for the state estimates becomes

$$\mathrm{E}\left(\delta\dot{x}^j\right) = 0, \qquad \mathrm{E}\left(\delta\dot{\phi}_{ca}^j\right) = 0 \tag{14.135}$$

as the known frequency tracking error should be compensated through the NCO command corrections. However, (14.134) should be used for the propagation of the prefilter error covariance, $\mathbf{P}_P^j$.

When necessary, control inputs can be added to the system model to account for known tracking errors due to lags in applying the IMU-measured dynamics to the NCO commands in the GNSS receiver.

System noise of variance $f_{ca}^2 S_c^a \tau_{Ps}/c^2$ must be modeled on the frequency tracking error to account for receiver clock noise, where τ_{Ps} is the prefilter system propagation interval and S_c^a is as defined in Section 14.2.7. Additional system noise, modeled on $\delta\dot{f}_{ca}^j$ where estimated and δf_{ca}^j, otherwise may be needed to account for the effects of uncompensated NCO control lags; its variance may be proportional to the squares of the line-of-sight acceleration and/or jerk.

In a coherent prefilter, the differences between the measured Is and Qs from the GNSS receiver and their predicted values form the measurement innovations. Thus,

$$\delta\mathbf{z}_{P,k'}^{j-} = \begin{pmatrix} \tilde{I}_E^j - \hat{I}_E^{j-} \\ \tilde{I}_P^j - \hat{I}_P^{j-} \\ \tilde{I}_L^j - \hat{I}_L^{j-} \\ \tilde{Q}_E^j - \hat{Q}_E^{j-} \\ \tilde{Q}_P^j - \hat{Q}_P^{j-} \\ \tilde{Q}_L^j - \hat{Q}_L^{j-} \end{pmatrix}_{k'}, \tag{14.136}$$

where the subscript P denotes a prefilter, the superscript j denotes the signal to which it applies, and k' denotes the prefilter iteration.

The predicted Is and Qs may be calculated using (9.10) as a function of the measured carrier power to noise density, $\tilde{c}/\tilde{n}_0$, estimated code tracking error, $\hat{x}_{k'}^j$, carrier tracking error, $\delta\hat{\phi}_{ca,k'}^j$, and frequency tracking error, $\delta\hat{f}_{ca,k'}^j$. The measurement matrix, $\mathbf{H}_{P,k'}^j$, is obtained by differentiating (9.10) with respect to the Kalman filter states.

If an EKF is used as the estimation algorithm, accurate estimates of the carrier phases are needed to compute both the predicted Is and Qs and the measurement matrices; without them, the tracking filter will not work. One solution to this problem

is to use a particle filter as each particle has its own carrier-phase estimate [37]. A particle filter can thus tolerate much higher carrier-phase tracking errors before losing lock. However, the processor load is much higher.

When navigation-data wipe-off or data-free signals are used, the incorporation of the Is and Qs into the estimation algorithm as measurements maintains coherent summation over a varying interval, determined by the filter gain. This optimizes the signal-to-noise performance (see Section 9.1.4.4). Consequently, coherent summation of the Is and Qs prior to their input to the tracking filter has little impact on performance [26]. When there are unknown data bits that are not estimated (see Section 10.3.5), coherent integration is limited to the data-bit intervals and the integration algorithm must use the sign of one of the Is and Qs to correct for the data bits. Thus,

$$\delta\mathbf{z}^{j-}_{P,k'} = \begin{pmatrix} \tilde{I}^j_E\tilde{D}^j_{k'} - \hat{I}^{j-}_E \\ \tilde{I}^j_P\tilde{D}^j_{k'} - \hat{I}^{j-}_P \\ \tilde{I}^j_L\tilde{D}^j_{k'} - \hat{I}^{j-}_L \\ \tilde{Q}^j_E\tilde{D}^j_{k'} - \hat{Q}^{j-}_E \\ \tilde{Q}^j_P\tilde{D}^j_{k'} - \hat{Q}^{j-}_P \\ \tilde{Q}^j_L\tilde{D}^j_{k'} - \hat{Q}^{j-}_L \end{pmatrix}_k \qquad \tilde{D}^j_{k'} = \begin{matrix} \dfrac{\text{sign}(\tilde{I}^j_P)}{\text{sign}(\hat{I}^{j-}_P)} & \left|\tilde{I}^j_P\right| \geq \left|\tilde{Q}^j_P\right| \\ \dfrac{\text{sign}(\tilde{Q}^j_P)}{\text{sign}(\hat{Q}^{j-}_P)} & \left|\tilde{I}^j_P\right| < \left|\tilde{Q}^j_P\right| \end{matrix}. \tag{14.137}$$

When an AGC is used in the receiver front end, the measurement noise should be constant (with the signal amplitude varying as a function of c/n_0). A suitable value for the measurement noise covariance matrix [assuming the measurement order defined in (14.136)] is

$$\mathbf{R}^j_P = \sigma^2_{IQ}\begin{pmatrix} 1 & (1-d/2)^2 & (1-d)^2 & 0 & 0 & 0 \\ (1-d/2)^2 & 1 & (1-d/2)^2 & 0 & 0 & 0 \\ (1-d)^2 & (1-d/2)^2 & 1 & 0 & 0 & 0 \\ 0 & 0 & 0 & 1 & (1-d/2)^2 & (1-d)^2 \\ 0 & 0 & 0 & (1-d/2)^2 & 1 & (1-d/2)^2 \\ 0 & 0 & 0 & (1-d)^2 & (1-d/2)^2 & 1 \end{pmatrix}, \tag{14.138}$$

where σ_{IQ} is the noise standard deviation of the accumulated correlator outputs and d is the early–late correlator spacing in code chips. The off-diagonal terms are nonzero because the noise is partially correlated between the three I measurements and between the three Q measurements from each channel. The noise standard deviation varies with the receiver design so must be determined empirically. It may be necessary to introduce a $\tilde{c}/\tilde{n}_0$ dependence if the AGC reaches minimum gain at a c/n_0 level where signals may still be tracked; this must also be determined empirically.

Pseudo-range and pseudo-range-rate measurement innovations for output to the integration filter can be obtained from the tracking filter state estimates using

$$\delta z^{j-}_{\rho,k} = -\frac{c}{f_{co}}\hat{x}^{j}_{k'}, \qquad \delta z^{j-}_{rk} = -\frac{c}{f_{ca}}\delta\hat{f}^{j}_{ca,k'}. \tag{14.139}$$

As a federated zero-reset architecture (Section 16.1.5.3) [17] is implemented for the code-phase and carrier-frequency states in the tracking filters, these states are zeroed when data is output to the integration filter to ensure that no information is held simultaneously by two sequential filters. The corresponding state uncertainties must be reset to the code-phase and carrier-frequency tracking uncertainties derived from the integration filter. Off-diagonal elements of the error covariance matrix, $\mathbf{P}^{j}_{P}$, pertaining to the reset states are zeroed. When estimated, $\delta\dot{f}^{j}_{ca}$ should be similarly reset. However, the carrier-phase error state is not reset as this information is required for processing future I and Q measurements and is not passed onto the integration filter.

The elements of the integration filter measurement noise covariance, $\mathbf{R}_G$, for the relevant signal should be determined from the tracking filter error covariance, $\mathbf{P}^{j}_{P}$, noting that, with a coherent prefilter, the pseudo-range and pseudo-range rate measurement noise will be correlated. Thus,

$$\mathrm{E}\left[\begin{pmatrix} w^{j}_{m,\rho,k} \\ w^{j}_{m,r,k} \end{pmatrix}\begin{pmatrix} w^{j}_{m,\rho,k} \\ w^{j}_{m,r,k} \end{pmatrix}^{\mathrm{T}}\right] = \begin{pmatrix} \frac{c}{f_{co}} & 0 \\ 0 & \frac{c}{f_{ca}} \end{pmatrix}\mathrm{E}\left[\begin{pmatrix} \delta x^{j}_{k'} \\ \delta\delta f^{j}_{ca,k'} \end{pmatrix}\begin{pmatrix} \delta x^{j}_{k'} \\ \delta\delta f^{j}_{ca,k'} \end{pmatrix}^{\mathrm{T}}\right]\begin{pmatrix} \frac{c}{f_{co}} & 0 \\ 0 & \frac{c}{f_{ca}} \end{pmatrix}. \tag{14.140}$$

An alternative to the tracking filter described here is to use the batch-processing acquisition and tracking algorithm described in Section 10.3.4 for the prefilters in coherent deep INS/GNSS integration [38].

14.3.3.4 Multisignal Prefiltering

When the receiver processes GNSS signals on more than one frequency, it is more efficient to process all measurements from a given satellite using the same prefilter. In this case, the prefilter must maintain an estimate of the ionosphere propagation delay which is used by the NCO control algorithm.

In a noncoherent prefilter, separate discriminators should be computed for each signal with ionosphere-corrected combinations (see Section 9.3.2) used to form the measurement innovations output to the integration filter. The differences between the discriminators for different frequencies should be used as the measurement inputs to an ionosphere delay estimation algorithm; this could be a simple fixed-gain loop filter.

One way of configuring a multifrequency coherent prefilter is to implement a separate tracking filter for each signal. At the output and reset stage, ionosphere-corrected combinations of the tracking filter estimates can then be used to form

the measurement innovations output to the integration filter, while the differences between the tracking filter estimates on each frequency are used to update the ionosphere delay estimate.

14.3.3.5 GNSS Receiver NCO Control

In deeply coupled INS/GNSS integration, the GNSS receiver NCO commands are generated by the navigation processor. By analogy with (9.39), the code NCO command for the *j*th signal is

$$\hat{f}^j_{co,NCO,k+1} = f_{co}\left[1 - \frac{\left(\hat{\rho}^{j-}_{a,R,k+1} - \hat{\rho}^{j-}_{a,R,k}\right)}{c\tau_N}\right], \tag{14.141}$$

where τ_N is the NCO-command update interval and the pseudo-range estimate is given by

$$\begin{aligned}\hat{\rho}^j_{a,R} &= \left|\hat{\mathbf{r}}^i_{ij}\left(\tilde{t}^j_{st,a}\right) - \hat{\mathbf{r}}^i_{ia}\right| + \delta\hat{\rho}^a_c + \delta\hat{\rho}^j_{I,a} + \delta\hat{\rho}^j_{T,a} - \delta\hat{\rho}^j_c + \delta\hat{\rho}^j_r \\ &= \left|\hat{\mathbf{C}}^I_e\left(\tilde{t}^j_{st,a}\right)\hat{\mathbf{r}}^e_{ej}\left(\tilde{t}^j_{st,a}\right) - \hat{\mathbf{r}}^e_{ea}\right| + \delta\hat{\rho}^a_c + \delta\hat{\rho}^j_{I,a} + \delta\hat{\rho}^j_{T,a} - \delta\hat{\rho}^j_c + \delta\hat{\rho}^j_r\end{aligned}, \tag{14.142}$$

where the notation is as defined in Section 8.5.3, except for $\delta\hat{\rho}^j_r$, which is the Kalman-filter-estimated residual range bias (see Section 14.2.1). The receiver clock offset estimate, $\delta\hat{\rho}^a_c$, is obtained from the integration Kalman filter. The satellite position, $\hat{\mathbf{r}}^\gamma_{\gamma j}$, is obtained from the navigation data message as described in Section 8.5.2. The satellite clock correction, $\delta\hat{\rho}^j_c$, is given by (9.77), the troposphere error estimate, $\delta\hat{\rho}^j_{T,a}$, is obtained from a model, and the ionosphere error estimate, $\delta\hat{\rho}^j_{I,a}$, is obtained from a model and/or the relevant prefilter or the integration Kalman filter. Troposphere and ionosphere models are presented in Section 9.3.2 and in Section G.7 of Appendix G on the CD. The GNSS antenna position is, from (2.162),

$$\hat{\mathbf{r}}^\gamma_{\gamma a} = \hat{\mathbf{r}}^\gamma_{\gamma b} + \hat{\mathbf{C}}^\gamma_b \mathbf{l}^b_{ba} \qquad \gamma \in i, e, \tag{14.143}$$

where $\hat{\mathbf{r}}^e_{eb}$ may be calculated from $\hat{L}_b$, $\hat{\lambda}_b$, and $\hat{h}_b$ using (2.112) where required.

Assuming the signal and reference carrier phases are not synchronized, the carrier NCO command is given by

$$\hat{f}^j_{ca,NCO,k+1} = f_{IF} - \frac{f_{ca}}{c}\hat{\rho}^{j-}_{a,R,k+1}, \tag{14.144}$$

where the pseudo-range rate estimated from the inertial navigation solution is given by (14.11), noting that the receiver clock drift estimate is obtained from the integration Kalman filter.

There can be a significant lag between the time of validity of the inertial navigation solution used to generate the NCO commands and the application of those

commands in the GNSS receiver. Contributions to this lag include the length of the IMU sampling window; the time taken to output the IMU samples to the navigation processor, update the inertial navigation solution, and generate the NCO commands; the time taken to communicate the NCO commands to the GNSS receiver and then apply them; and the length of the GNSS signal correlation window [16]. This NCO control lag can cause significant tracking errors. However, it can be mitigated by using the estimated pseudo-range acceleration to predict the NCO commands forward in time from the inertial navigation solution time of validity to the signal correlation time. The range acceleration is calculated as shown in Section G.4.1 of Appendix G on the CD. The pseudo-range acceleration is assumed to be the same as the rate of change of the clock drift is not easily predictable. If the receiver does not permit variation of the NCO frequencies over the correlation interval, the NCO control algorithm should supply average values, determined using the pseudo-range acceleration.

When the navigation system is subject to significant jerk, an acceleration valid over the IMU sampling interval may be out of date by the time of the GNSS signal correlation interval when it is applied. However, by the time the I and Q measurements from that correlation interval are processed by the prefilters, further IMU measurements will have been processed. Consequently, corrections may be applied within the prefilters as discussed in Sections 14.3.3.2 and 14.3.3.3.

NCO control lags may be eliminated by using a software receiver, which enables the GNSS signal samples to be stored until the contemporaneous IMU measurements have been processed.

For most applications, an NCO command update rate of 50 Hz is sufficient when data latency compensation is applied, while a 100-Hz update rate is recommended without latency compensation. Exceptions are applications with extreme dynamics or vibration where the acceleration is liable to exceed 100 m s^{-2} or the jerk 100 m s^{-3}, noting that oscillatory jerk is not expected to cause loss of tracking where the position amplitude is much less than a GNSS carrier wavelength [16].

14.3.4 Estimation of Attitude and Instrument Errors

In INS/GNSS integration, the measurement innovations input to the Kalman filter are based on position and velocity or pseudo-range and pseudo-range rate. As (14.115), (14.126), and (14.127) show, the direct coupling of these measurements to the attitude-error and instrument-error states is usually negligible. Yet the Kalman filter still estimates these errors and how it does this is not intuitive. Here an explanation is presented.

As explained in Section 14.2.1, the attitude and instrument errors are observed through the growth in the velocity error they produce, with the attitude errors and accelerometer biases inducing a linear growth in the velocity error and gyro biases inducing a quadratic growth. The corresponding growths in position error are quadratic and cubic, respectively. This coupling of the states is represented by the system model (Sections 14.2.2–14.2.5). Each time the error covariance matrix, **P**, is propagated through the system model [using (3.15) or (3.46)], information on the

correlations between the residual attitude and instrument errors and the residual position and velocity errors is built up in the off-diagonal elements of **P**. This enables the measurement model to estimate corrections to the attitude and instrument error estimates from measurements of the position and velocity errors (or linear combinations thereof).

When a measurement update is performed, the error covariance matrix, **P**, is used in the calculation of the Kalman gain matrix, **K**, using (3.21). The products of the off-diagonal elements of **P** with the elements of the measurement matrix, $\mathbf{H}_G$, coupling the position and velocity errors to the measurements give elements of **K** coupling the measurements to the attitude and instrument errors. Thus, when a state-vector update, (3.24), is performed, the attitude and instrument error estimates are updated alongside the position and velocity error estimates and any GNSS states.

14.4 Advanced INS/GNSS Integration

This section collects together a number of advanced INS/GNSS integration topics. Integration of INS with differential, carrier-phase, and multiantenna GNSS; modeling large heading errors; advanced IMU error modeling; and smoothing are discussed.

14.4.1 Differential GNSS

Differential GNSS, described in Section 10.1, improves position accuracy by calibrating out much of the temporally and spatially-correlated biases in the pseudo-range measurements due to ephemeris prediction errors, residual satellite clock errors, ionospheric refraction, and sometimes tropospheric refraction.

The architectures for integrating DGNSS with INS are essentially the same as for stand-alone GNSS. Differential corrections are applied to the pseudo-range measurements. In loosely coupled integration, this occurs within the GNSS user equipment. For tightly coupled integration, the pseudo-range measurements may be corrected by the GNSS ranging processor or within the integration algorithm's measurement model. For deeply coupled integration, the differential corrections are applied within the NCO control algorithm.

The measurement noise covariance, $\mathbf{R}_G$, due to tracking noise, multipath, time-synchronization errors, and lever arm flexure is the same as for stand-alone GNSS as these error sources are unchanged by the application of differential corrections. However, the standard deviation of the range biases, whether modeled as states (see Sections 14.2.1 and 14.2.7) or as additional position and clock-offset uncertainty (see Section 9.4.2.5), will be smaller and should be reduced to a value commensurate with the accuracy of the overall differential corrections. This will also affect any weighting of $\mathbf{R}_G$ to account for variation in the range bias standard deviations between measurements. The noise on the differential corrections will typically be much smaller than that on the user receiver's pseudo-range measurements due to the use of smoothing at the reference station.

14.4.2 Carrier-Phase Positioning

As described in Section 10.2, real-time centimeter-accuracy positioning can be obtained by comparing GNSS ADR measurements with those made by user equipment at a precisely surveyed base station. Integration with INS, as well as bridging the position solution through GNSS outages, can also bridge the ambiguity resolution process through outages of up to about a minute [39, 40] and aid the detection and correction of cycle slips [41].

Loosely coupled integration of carrier-phase GNSS with INS is the same as integration of stand-alone or differential GNSS, except that the measurement noise covariance, $\mathbf{R}_G$, must be adjusted to account for the smaller GNSS position errors and their different time correlation properties. The position error variance will typically be of order $(0.01\text{–}0.05\text{m})^2$. However, to determine $\mathbf{R}_G$, this should be multiplied by the ratio of the error correlation time to the measurement update time interval, as for code-based GNSS position. The error correlation time will vary with the GNSS user equipment design.

Tightly coupled INS/GNSS integration may be performed independently of ambiguity resolution by inputting double-differenced ADR measurements, with the integer wavelength ambiguities corrected, to the integration algorithm [42, 43]. These may be converted to ambiguity-corrected ADR measurements differenced across satellites only using

$$\Delta\breve{\tilde{\Phi}}_{a,R}^{ts,l} = \nabla\Delta\tilde{\Phi}_{ra,R}^{ts,l} - \nabla\Delta\Phi\breve{N}_{ra}^{ts,l}\lambda_{ca}^{l} + \left|\mathbf{C}_e^I\left(\tilde{t}_{st,r}^{s,l}\right)\hat{\mathbf{r}}_{es}^{e}\left(\tilde{t}_{st,r}^{s,l}\right) - \mathbf{r}_{er}^{e}\right| - \left|\mathbf{C}_e^I\left(\tilde{t}_{st,r}^{s,l}\right)\hat{\mathbf{r}}_{et}^{e}\left(\tilde{t}_{st,l}^{t,l}\right) - \mathbf{r}_{er}^{e}\right|, \quad (14.145)$$

where the notation is as defined in Section 10.2 and the reference station position, $\mathbf{r}_{er}^{e}$, is assumed to be known. The measurement innovation vector is then

$$\delta\mathbf{z}_{\Phi,k}^{-} = \begin{pmatrix} \Delta\breve{\tilde{\Phi}}_{a,R}^{t1,l} - \hat{r}_{a1}^{-} + \hat{r}_{at}^{-} \\ \Delta\breve{\tilde{\Phi}}_{a,R}^{t2,l} - \hat{r}_{a2}^{-} + \hat{r}_{at}^{-} \\ \vdots \\ \Delta\breve{\tilde{\Phi}}_{a,R}^{tm,l} - \hat{r}_{am}^{-} + \hat{r}_{at}^{-} \end{pmatrix}_k, \quad (14.146)$$

where

$$\begin{aligned} \hat{r}_{as,k}^{-} &= \sqrt{\left[\hat{\mathbf{r}}_{is}^{i}\left(\tilde{t}_{st,a,k}^{s}\right) - \hat{\mathbf{r}}_{ia,k}^{i-}\right]^{\mathrm{T}}\left[\hat{\mathbf{r}}_{is}^{i}\left(\tilde{t}_{st,a,k}^{s}\right) - \hat{\mathbf{r}}_{ia,k}^{i-}\right]} \\ &= \sqrt{\left[\hat{\mathbf{r}}_{es}^{e}\left(\tilde{t}_{st,a,k}^{s}\right) - \hat{\mathbf{r}}_{ea,k}^{e-}\right]^{\mathrm{T}}\left[\hat{\mathbf{r}}_{es}^{e}\left(\tilde{t}_{st,a,k}^{s}\right) - \hat{\mathbf{r}}_{ea,k}^{e-}\right]} + \delta\rho_{ie}^{s} \\ &= \sqrt{\left[\mathbf{C}_e^I\left(\tilde{t}_{st,a,k}^{s}\right)\hat{\mathbf{r}}_{es}^{e}\left(\tilde{t}_{st,a,k}^{s}\right) - \hat{\mathbf{r}}_{ea,k}^{e-}\right]^{\mathrm{T}}\left[\mathbf{C}_e^I\left(\tilde{t}_{st,a,k}^{s}\right)\hat{\mathbf{r}}_{es}^{e}\left(\tilde{t}_{st,a,k}^{s}\right) - \hat{\mathbf{r}}_{ea,k}^{e-}\right]} \end{aligned}. \quad (14.147)$$

Note there is no benefit in using pseudo-range or pseudo-range rate measurements alongside ADR measurements, though the pseudo-ranges are used for the wavelength ambiguity determination.

The state vector is the same as for conventional tightly coupled integration except that the receiver clock states are omitted. Assuming the state vector defined by (14.15), (14.39), or (14.51), the measurement matrix is

$$\mathbf{H}_{\boldsymbol{\Phi},k}^{\Delta\gamma} \approx \begin{pmatrix} \mathbf{0}_{1,3} & \mathbf{0}_{1,3} & \left(\mathbf{u}_{a1}^{\gamma} - \mathbf{u}_{at}^{\gamma}\right)^{\mathrm{T}} & \mathbf{0}_{1,3} & \mathbf{0}_{1,3} \\ \mathbf{0}_{1,3} & \mathbf{0}_{1,3} & \left(\mathbf{u}_{a2}^{\gamma} - \mathbf{u}_{at}^{\gamma}\right)^{\mathrm{T}} & \mathbf{0}_{1,3} & \mathbf{0}_{1,3} \\ \vdots & \vdots & \vdots & \vdots & \vdots \\ \mathbf{0}_{1,3} & \mathbf{0}_{1,3} & \left(\mathbf{u}_{am}^{\gamma} - \mathbf{u}_{at}^{\gamma}\right)^{\mathrm{T}} & \mathbf{0}_{1,3} & \mathbf{0}_{1,3} \end{pmatrix}_{\mathbf{x}=\hat{\mathbf{x}}_{k}^{-}} \quad \gamma \in i,e \tag{14.148}$$

or

$$\mathbf{H}_{\boldsymbol{\Phi},k}^{\Delta n} \approx \begin{pmatrix} \mathbf{0}_{1,3} & \mathbf{0}_{1,3} & \left(\mathbf{h}_{\rho p}^{1} - \mathbf{h}_{\rho p}^{t}\right)^{\mathrm{T}} & \mathbf{0}_{1,3} & \mathbf{0}_{1,3} \\ \mathbf{0}_{1,3} & \mathbf{0}_{1,3} & \left(\mathbf{h}_{\rho p}^{2} - \mathbf{h}_{\rho p}^{t}\right)^{\mathrm{T}} & \mathbf{0}_{1,3} & \mathbf{0}_{1,3} \\ \vdots & \vdots & \vdots & \vdots & \vdots \\ \mathbf{0}_{1,3} & \mathbf{0}_{1,3} & \left(\mathbf{h}_{\rho p}^{m} - \mathbf{h}_{\rho p}^{t}\right)^{\mathrm{T}} & \mathbf{0}_{1,3} & \mathbf{0}_{1,3} \end{pmatrix}_{\mathbf{x}=\hat{\mathbf{x}}_{k}^{-}}, \tag{14.149}$$

where $\mathbf{h}_{\rho p}^{s}$ is given by (14.128).

The measurement noise covariance matrix is nondiagonal and given by

$$\mathbf{R}_{\boldsymbol{\Phi},k}^{\nabla\Delta} = \mathbf{D}_{G}\mathbf{R}_{\boldsymbol{\Phi},k}^{\nabla}\mathbf{D}_{G}^{\mathrm{T}}, \tag{14.150}$$

where $\mathbf{R}_{\boldsymbol{\Phi},k}^{\nabla}$ is a diagonal matrix representing the noise on the single-satellite ADR measurements differenced between user and reference. It will typically be at centimeter level and should account for reference station as well as user measurement noise. The range biases may often be neglected.

In both the loosely coupled and tightly coupled integration architectures, the corrected INS position solution may be used to aid GNSS ambiguity resolution. However, both the integration and ambiguity resolution algorithms must be carefully tuned to avoid positive-feedback problems. Alternatively, where the ambiguity resolution algorithm is Kalman filter-based, it may be combined with the integration algorithm into a single algorithm, estimating both the INS errors and the float carrier wavelength ambiguities. This is described in Section I.7.1 of Appendix I on CD and also applies to deeply coupled integration.

14.4.3 GNSS Attitude

GNSS attitude determination uses relative carrier-phase positioning between antennas mounted on the same vehicle as described in Section 10.2.5. GNSS attitude is very noisy, but does not drift, making it highly complementary to INS attitude and a solution to the heading calibration problem that occurs for some INS/GNSS applications. By combining INS with multiantenna GNSS, a precise and stable attitude solution may be obtained. A full GNSS attitude solution requires three or more antennas. However, two antennas is sufficient for INS/GNSS in cases where conventional INS/GNSS meets the roll and pitch accuracy requirements [44].

For loosely coupled integration of GNSS attitude, an additional measurement innovation is added:

$$\mathbf{I}_3 + \left[\delta\mathbf{z}^{\gamma-}_{\psi,k} \wedge\right] \approx \tilde{\mathbf{C}}^{\gamma}_{aG,k}\mathbf{C}^{a}_{b}\hat{\mathbf{C}}^{b-}_{\gamma,k} \qquad \gamma \in i,e,n, \tag{14.151}$$

where $\tilde{\mathbf{C}}^{\gamma}_{aG}$ is the GNSS attitude measurement, and the relative orientation of the INS and GNSS body frames, $\mathbf{C}^{a}_{b}$, is assumed to be known. The measurement matrix is

$$\mathbf{H}^{i/e/n}_{\psi k} = \begin{pmatrix} -\mathbf{I}_3 & \mathbf{0}_3 & \mathbf{0}_3 & \mathbf{0}_3 & \mathbf{0}_3 \end{pmatrix}, \tag{14.152}$$

assuming the state vector defined by (14.15), (14.39), or (14.51).

Tightly coupled integration of GNSS attitude may be performed by inputting measurements of ADR differenced between antennas [45]. Note that this differencing eliminates the position and velocity information, leaving only attitude. Measurements may also be differenced across satellites to eliminate any residual timing and phase biases between antennas, noting that a common receiver clock is typically used for multi-antenna GNSS.

When measurements comprise ADRs double-differenced across satellites and between antennas a and A, the tightly coupled measurement innovations are

$$\delta\mathbf{z}^{\gamma-}_{\psi,k} = \begin{pmatrix} \nabla\Delta\tilde{\boldsymbol{\Phi}}^{t1,l}_{aA,R} - \nabla\Delta\breve{N}^{t1,l}_{aA}\lambda^{l}_{ca} + \left(\mathbf{u}^{\gamma}_{a1} - \mathbf{u}^{\gamma}_{at}\right)^{\mathrm{T}}\hat{\mathbf{C}}^{\gamma}_{b}\mathbf{r}^{b}_{aA} \\ \nabla\Delta\tilde{\boldsymbol{\Phi}}^{t2,l}_{aA,R} - \nabla\Delta\breve{N}^{t2,l}_{aA}\lambda^{l}_{ca} + \left(\mathbf{u}^{\gamma}_{a2} - \mathbf{u}^{\gamma}_{at}\right)^{\mathrm{T}}\hat{\mathbf{C}}^{\gamma}_{b}\mathbf{r}^{b}_{aA} \\ \vdots \\ \nabla\Delta\tilde{\boldsymbol{\Phi}}^{tm,l}_{aA,R} - \nabla\Delta\breve{N}^{tm,l}_{aA}\lambda^{l}_{ca} + \left(\mathbf{u}^{\gamma}_{am} - \mathbf{u}^{\gamma}_{at}\right)^{\mathrm{T}}\hat{\mathbf{C}}^{\gamma}_{b}\mathbf{r}^{b}_{aA} \end{pmatrix}_{k} \qquad \gamma \in i,e,n, \tag{14.153}$$

where $\nabla\Delta\tilde{\boldsymbol{\Phi}}^{ts,l}_{aA,R}$ is the double-differenced ADR, given by

$$\nabla\Delta\tilde{\boldsymbol{\Phi}}^{ts,l}_{aA,R} = \tilde{\boldsymbol{\Phi}}^{s,l}_{A,R} - \tilde{\boldsymbol{\Phi}}^{t,l}_{A,R} - \tilde{\boldsymbol{\Phi}}^{s,l}_{a,R} + \tilde{\boldsymbol{\Phi}}^{t,l}_{a,R}, \tag{14.154}$$

$\nabla\Delta\breve{N}^{ts,l}_{aA}$ is the fixed double-differenced integer wavelength ambiguity estimate, and $\mathbf{r}^{a}_{aA}$ is the position of antenna A with respect to antenna a, resolved about INS

body-frame axes, b. When the error in the corrected inertial attitude solution, $\hat{\mathbf{C}}_b^{\gamma}$, is relatively small, the correct integer ambiguities will be those that minimize the measurement innovations. The measurement matrix is

$$\mathbf{H}_{\psi k}^{\gamma} = \begin{pmatrix} \left(\mathbf{u}_{a1}^{\gamma} - \mathbf{u}_{at}^{\gamma}\right)^{\mathrm{T}} \left[\left(\hat{\mathbf{C}}_b^{\gamma} \mathbf{r}_{aA}^{b}\right) \wedge\right] & \mathbf{0}_{1\times 3} & \mathbf{0}_{1\times 3} & \mathbf{0}_{1\times 3} & \mathbf{0}_{1\times 3} \\ \left(\mathbf{u}_{a2}^{\gamma} - \mathbf{u}_{at}^{\gamma}\right)^{\mathrm{T}} \left[\left(\hat{\mathbf{C}}_b^{\gamma} \mathbf{r}_{aA}^{b}\right) \wedge\right] & \mathbf{0}_{1\times 3} & \mathbf{0}_{1\times 3} & \mathbf{0}_{1\times 3} & \mathbf{0}_{1\times 3} \\ \vdots & \vdots & \vdots & \vdots & \vdots \\ \left(\mathbf{u}_{am}^{\gamma} - \mathbf{u}_{at}^{\gamma}\right)^{\mathrm{T}} \left[\left(\hat{\mathbf{C}}_b^{\gamma} \mathbf{r}_{aA}^{b}\right) \wedge\right] & \mathbf{0}_{1\times 3} & \mathbf{0}_{1\times 3} & \mathbf{0}_{1\times 3} & \mathbf{0}_{1\times 3} \end{pmatrix}_{\hat{\mathbf{x}}=\hat{\mathbf{x}}_{\bar{k}}} \quad \gamma \in i,e,n, \quad (14.155)$$

again assuming the previous state vector defined by (14.15), (14.39), or (14.51). The measurement noise covariance is as given by (14.150). Note that ADR difference measurements between a second pair of antennas must be added to provide three-axis GNSS attitude measurements.

Note that both the loosely coupled and tightly coupled forms of GNSS attitude integration may be combined with either loosely coupled or tightly coupled integration of the GNSS range measurements.

Another form of tightly coupled attitude integration, which is not compatible with loosely coupled position and velocity integration, processes separate code- and carrier-phase-derived range-domain measurements from each antenna in a single EKF. The EKF's measurement matrix performs the differencing of carrier-phase-derived measurements between antennas that is required to obtain the attitude information. Note that the appropriate lever arms must be modeled and the attitude-error components of the measurement matrix, $\mathbf{H}_G$, must not be neglected [42].

The accuracy of INS/GNSS attitude determination depends on the quality of the inertial sensors and the antenna separation. Longer lever arms produce more precise GNSS attitude measurements, but can be subject to flexure. One solution to the flexure problem is to measure it using the main IMU, additional inertial sensors at the antennas, and strain gauges [46].

The inertial attitude solution can be used to aid the GNSS wavelength ambiguity resolution process, either by constraining the search space or by estimating the float ambiguities in the integration algorithm as described in Section I.7.2 of Appendix I on the CD. With a short baseline, the inertial attitude alone may be sufficient resolve the ambiguities.

14.4.4 Large Heading Errors

In the examples of INS/GNSS Kalman filters presented in Sections 14.2 and 14.3, the small angle approximation is applied to the attitude errors. This is usually valid for the roll and pitch attitude, which may be observed through leveling (Section 5.6.2). However, the heading (or azimuth) is more difficult to initialize. Only the higher grades of INS are capable of gyrocompassing, while magnetic heading is subject to

environmental anomalies and heading derived from the GNSS trajectory is subject to sideslip-induced errors.

When consumer-grade inertial sensors are used, all three components of the attitude error can be relatively large, particularly during GNSS outages or when signal reception is poor.

When the small angle approximation is applied to the attitude components resolved about the horizontal axes, but not the heading, the attitude-error coordinate transformation matrix may be expressed as

$$\begin{aligned}\delta \mathbf{C}_b^n &\approx \begin{pmatrix} \cos\delta\psi_{nb,D}^n & -\sin\delta\psi_{nb,D}^n & \delta\psi_{nb,N}^n \sin\delta\psi_{nb,D}^n + \delta\psi_{nb,E}^n \cos\delta\psi_{nb,D}^n \\ \sin\delta\psi_{nb,D}^n & \cos\delta\psi_{nb,D}^n & -\delta\psi_{nb,N}^n \cos\delta\psi_{nb,D}^n + \delta\psi_{nb,E}^n \sin\delta\psi_{nb,D}^n \\ -\delta\psi_{nb,E}^n & \delta\psi_{nb,N}^n & 1 \end{pmatrix}, \\ &= \begin{pmatrix} \cos\delta\psi_{nb,D}^n & -\sin\delta\psi_{nb,D}^n & 0 \\ \sin\delta\psi_{nb,D}^n & \cos\delta\psi_{nb,D}^n & 0 \\ 0 & 0 & 1 \end{pmatrix} \left(\mathbf{I}_3 + \left[\begin{pmatrix} \delta\psi_{nb,N}^n \\ \delta\psi_{nb,E}^n \\ 0 \end{pmatrix} \times \right] \right)\end{aligned} \quad (14.156)$$

noting that the down component of the attitude error, $\delta\psi_{nb,D}^n$, is the heading error, $\delta\psi_{nb}$.

Using (14.156), the system model is no longer a linear function of the error states, a key requirement of Kalman filtering. One solution is to replace the heading error state with sine and cosine terms, $\sin\delta\psi_{nb}$ and $\cos\delta\psi_{nb}$ [47] or $\delta\sin\psi_{nb}$ and $\delta\cos\psi_{nb}$ [48, 49]. These enable INS/GNSS integration and other forms of fine alignment (Section 5.6.3) to take place with no prior knowledge of heading.

When the heading error is very large, the products of the heading error state(s) with other states are no longer negligible, so a system model of at least second order is required. With a consumer-grade IMU, this can also apply to the roll and pitch. An extended Kalman filter (Section 3.4.1) is not suitable as it linearizes the propagation of the error covariance matrix, **P**, through which the attitude errors are observed (Section 14.3.4). Alignment with large heading errors has been demonstrated using an unscented Kalman filter (Section 3.4.2) [50] and a number of other nonlinear filters [51], noting that nonlinear filtering is only needed for the system propagation phase [52]. However, other research has shown that a conventional approach with closed-loop INS correction works equally well for initial attitude uncertainties up to 30° [53]. Where the initial heading is completely unknown, a particle filter (Section 3.5) may be used.

When either a particle filter or the system propagation phase of a UKF is implemented, total-state integration should be used as discussed in Section 14.1.1. In this case, separate inertial navigation equations are implemented for each particle or sigma point. Separate corrections are also applied to the IMU outputs. Each system propagation phase will typically comprise tens of inertial navigation processing cycles using successive IMU outputs. Figure 14.12 illustrates this for a UKF. GNSS state estimates may be propagated in one step.

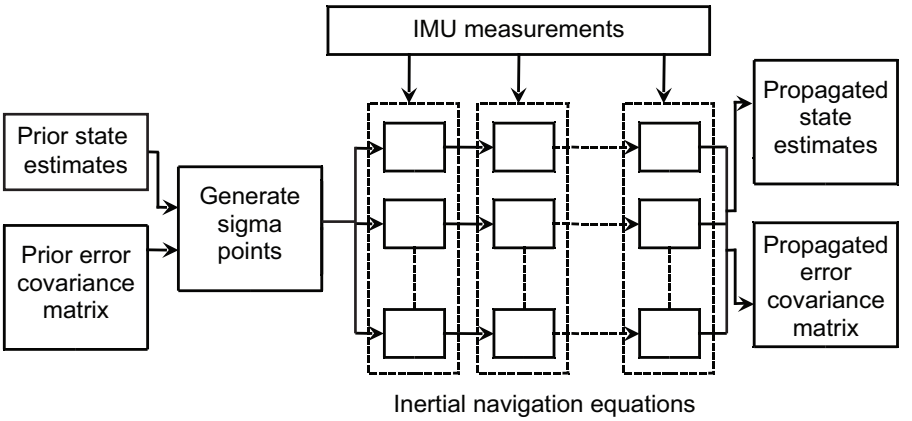

Figure 14.12 Total-state system propagation of INS states using a UKF.

14.4.5 Advanced IMU Error Modeling

Low-grades of IMU, particularly those using MEMS sensors, can exhibit high levels of noise. To optimize the Kalman filter gain, as discussed in Section 3.3.1, it is important to match the assumed sensor noise to its true value. Unfortunately, the manufacturer's specification may not be an accurate guide due both to variation in noise performance between individual sensors and to variation in effective noise levels with the vibration environment (see Sections 4.4.3 and 4.4.5).

One solution is to use an adaptive Kalman filter to vary the assumed system noise covariance according to the measurement innovations as described in Section 3.4.4. Both the innovation-based and multiple-model adaptive estimation techniques have been shown to speed up the rate of convergence of the state estimates with their true counterparts [54–57]. Interestingly, these algorithms tend to select high levels of system noise initially, leading to high Kalman filter gains and faster convergence, and then switch to lower system noise after convergence, producing lower gains, more stable state estimates, and smaller state uncertainties. Note that IAE-derived covariances may require rescaling to account for time-correlated measurement noise. Using an ANN to estimate the system noise covariance as a function of velocity increments and attitude increments [58] and using reinforcement learning to automate the manual tuning process [59] have also been shown to improve performance.

When the dominant vibration modes are known, or determined from the IMU data, they can be incorporated into the Kalman filter. Modeling the sensor noise as correlated by second-order Markov processes using a Schmidt-Kalman filter (Section D.2 of Appendix D on the CD) has been shown to improve alignment performance for missiles in an air-carriage environment [60].

MEMS IMUs can also exhibit complex higher-order systematic and slowly time-varying errors that are difficult to model using a Kalman filter. However, these errors can be modeled using an ANN alongside a conventional Kalman filter estimating

the standard 15 INS error states (see Sections 14.2.2–14.2.4). The neural network is trained while GNSS data is available and then predicts the residual INS position errors during outages, noting that the dynamics in the training and prediction phases must be similar. Significant improvements in position accuracy during GNSS outages have been demonstrated using a number of hybrid ANN/Kalman filter integration algorithms, compared to a Kalman filter alone [61–65]. However, it should be noted that the tests assumed good GNSS reception during training and complete GNSS outages during prediction. Therefore, further work is needed to address degraded GNSS reception conditions.

Accelerometer and gyro biases (Section 4.4.1) vary over time. This is conventionally accounted for by modeling white system noise on the bias states, or by modeling each bias state as either first-order Markov processes or the sum of a constant and a Markov state. However, these models are only a rough approximation of the sensor behavior. Performance improvements have been demonstrated by representing the biases as second- and third-order autoregressive models, tuned to each sensor type [66, 67], while a frequency-domain approach [68] avoids the need to make a priori assumptions about the time variations and can improve the speed of convergence.

All of these methods of modeling IMU errors require more processing capacity, and were relatively immature at the time of writing. However, they demonstrate the scope to improve upon the conventional system models described in Section 14.2.

14.4.6 Smoothing

For many applications, such as surveying, geo-referencing, vehicle testing, and military ranges, the navigation solution is required for analysis after the event. In these cases, the INS errors can be calibrated using GPS measurements taken after the time of interest as well as before. A standard Kalman filter will not do this; the solution is to use a Kalman smoother, as described in Section 3.4.6. Whether smoothing significantly improves performance depends on the application. It is useful when it is not practical to undergo a period of INS calibration before the data set of interest or where a heading solution is required and the heading error is difficult to observe. However, it has the biggest impact where GNSS signal availability is relatively poor, such as in urban areas, particularly where carrier-phase accuracy is required [69] or a low-grade IMU is used [70]. Smoothing effectively halves the period of INS drift during GNSS outages, reducing the maximum position error by a factor of up to 4.

Problems and exercises for this chapter are on the accompanying CD.

References

[1] Titterton, D. H., and J. L. Weston, *Strapdown Inertial Navigation Technology*, 2nd ed., Stevenage, U.K.: IEE, 2004.

[2] Grewal, M. S., L. R. Weill, and A. P. Andrews, *Global Positioning Systems, Inertial Navigation, and Integration*, 2nd ed., New York: Wiley, 2007.

[3] Farrell, J. A., *Aided Navigation*, New York: McGraw-Hill, 2008.